Volume 93, Number 2, March–April 1988
Journal of Research of the National Bureau of Standards

In This Issue:

Departments

News Briefs

Articles

Volume 93, Number 2, March–April 1988
Journal of Research of the National Bureau of Standards

News Briefs

Developments

PRESIDENT SIGNS COMPUTER SECURITY ACT

On January 8, President Reagan signed the Computer Security Act of 1987 (P.L. 100–235) giving NBS the primary responsibility for developing standards and guidelines needed to secure sensitive, unclassified information in Federal computer systems. In addition, the act amends the basic charter of NBS and mandates a computer standards program within NBS. (Since 1966, under the Brooks Act and policy directives from the Office of Management and Budget, the NBS Institute for Computer Sciences and Technology has conducted a computer standards program for the Federal Government which included computer security activities.)

The Computer Security Act leaves unchanged the National Security Agency's (NSA) authority over computer systems containing classified, national security-related information. NBS will continue to work closely with NSA and to draw upon the agency's technical advice and assistance where appropriate.

NEW PATENT COVERS 3-D LASER MEASUREMENT SYSTEM

NBS researchers have received a patent for an automated laser tracking system that greatly simplifies the task of accurately measuring the dimensions of large shapes, such as aircraft wings or fuel tanks.

The five-axis laser tracking system invented by Kam Lau and Robert Hocken of the NBS Center for Manufacturing Engineering includes a laser interferometer, a servo-controlled tracking mirror, a similar target mirror, and a computer to control the system. Once the laser is "locked" on the target mirror, the control system keeps the beam centered on the target as it is moved about the space to be measured. The interferometer constantly returns displacement measurements to the controller, and angle-sensitive transducers on the tracking and target mirrors send the data necessary for the computer to keep a running account of the three-dimensional position, pitch, and roll of the target mirror. A simpler 3-axis system, also covered by this patent, measures the position of the target without pitch and roll.

The system is portable, fully automated, uses only one station, and can measure positions over a sizeable volume (a radius of 20 meters or greater over 360° in the horizontal and $\pm 40°$ in the vertical) to an accuracy of about one part in 100,000. This is about 3 times better than a close competitor: a multi-station, computer-assisted theodolite system (also invented at NBS).

Other applications include assessing the static and dynamic performance of robot arms and the accuracy of machine tools and coordinate measuring machines. The system is being marketed by Automated Precision, Inc., 7901-C Cessna Avenue, Gaithersburg, MD 20879.

MILLION-FOLD IMPROVEMENT IN SUPERCONDUCTOR RESISTANCE

In further developments on the high-temperature superconductor front, NBS and Westinghouse have lowered contact resistivity to a million times less than indium-solder contacts. This a hundred- to a thousand-fold improvement over the earlier reported results of Ekin (NBS), Panson and Blankenship (both of Westinghouse) who devel-

oped the basic technique. The newest results are obtained by annealing the sputter-deposited silver contact pads on the superconductor in oxygen at temperatures up to 500 °C for an hour. (The previously reported technique involved temperatures up to 150 °C, but no oxygen annealing.) Where the intermediate (500 °C) temperatures can be tolerated, the annealing technique yields resistivities of about 10^{-8} ohm-cm^2 at 76 K for bulk sintered samples of $YBa_2Cu_3O_7$. This resistivity was measured for current densities of up to 100 A/cm^2. The voltage-current characteristic was non-linear, having the character of a superconducting proximity effect; at lower current densities, below 30 A/cm^2, the resistivity was unmeasurably low.

For technical details, contact Jack Ekin, Division 724.05, National Bureau of Standards, 325 Broadway, Boulder, CO 80303, 303/497-5448.

NBS SEEKS HELP TO AUTOMATE PLASTIC PROCESSES

Polymer scientists at NBS are seeking cooperation from researchers in industry, universities, and other organizations to help develop the measurement tools manufacturers need to automate the processing of high-performance plastics, polymer blends, and advanced composite materials.

The NBS researchers have identified three areas that need to be developed: sensors to monitor polymer production processes, processing models for producers, and a database on the properties of polymer materials. To meet the measurement goal, researchers are invited to collaborate in the development of technology to monitor the quality of the mix of product ingredients, the viscosity of polymers in a molten state, the flow and velocity of polymeric materials, the orientation of molecules during processing, and the interlocking of molecules in two-phase materials such as block copolymers. Several NBS facilities for polymer research are available to industry for joint projects. Under the NBS Research Associate Program guest scientists and engineers are able to conduct research at the Bureau on projects of mutual interest with salaries paid by their employers.

For information on the plastic processes cooperative program, contact Drs. Anthony J. Bur or Francis W. Wang, B320 Polymer Building, National Bureau of Standards, Gaithersburg, MD 20899, 301/975-6748.

BULLETIN BOARD STARTED ON FIRE RESEARCH PROGRAMS

Many of the computer programs developed by the NBS Center for Fire Research (CFR) now can be obtained 24 hours a day, 7 days a week through a computerized bulletin board called CFRBBS. Included are computer programs which simulate the movement of smoke and toxic gases and the decisions and actions of occupants during a fire as well as a program which can help analyze smoke control systems. Information on upcoming CFR activities, such as conferences; a list of recent CFR reports; and information on accessing FIREDOC (a computerized fire research database) also is available on the bulletin board. It is designed to operate with IBM personal computers or compatible computers. The modem telephone number is 301/921-6302. The bulletin board operates at 300, 1200, or 2400 BAUD with most PC communications packages. The package should be set for 8 data bits, 1 stop bit, and no parity. Xmodem, Ymodem, Crxmodem, or Kermit protocol is required to download most of the files. No password is needed and there is no fee other than telephone costs paid by the user.

For additional information, contact system operator Doug Walton, B345 Polymer Building, National Bureau of Standards, Gaithersburg, MD 20899, 301/975-6872.

COMPUTER SECURITY STANDARD REAFFIRMED FOR FIVE MORE YEARS

NBS has reaffirmed use of the Data Encryption Standard (DES) for another 5 years, saying it continues to be a sound method for protecting computerized data. Based on a technique developed by IBM, the standard was adopted by NBS and approved by the Secretary of Commerce as a Federal Information Processing Standard in 1977. (These standards are developed by NBS for use by the Federal Government.) The DES is reviewed by the Bureau and the Secretary of Commerce every 5 years to determine its adequacy to protect computerized data.

"The DES continues to be a sound and economical method for protecting unclassified, but valuable or sensitive data, and we support it," said Dr. Dennis Branstad of the Bureau's Institute for Computer Sciences and Technology.

The DES provides a publicly available set of equations, or "algorithm," to encode a message and a 56-bit electronic "key," held by the sender and receiver, to decode it. In 1977, NBS set up a laboratory to validate commercial devices to help ensure that products properly implement the standard and are compatible with other equipment using the DES. More than 100,000 devices that conform to the standard are currently being used to protect computer information.

Among other uses, the DES has been adopted by the American National Standards Institute and the American Bankers Association for protecting transfers of funds and securities over communications lines, a process known as electronic funds transfer. NBS also is helping the Department of the Treasury to use the DES to help protect the billions of dollars in federal funds that are transferred electronically each year.

Contact Dr. Dennis Branstad, A225 Technology Building, National Bureau of Standards, Gaithersburg, MD 20899, 301/975-2913.

ENVIRONMENTAL "FROZEN ASSETS" DESCRIBED IN VIDEOTAPE

A project that is using frozen environmental samples to monitor pollution trends across the country is described in an 8.5-minute videotape available from NBS. The tape examines the National Biomonitoring Specimen Bank, which is a storage facility and clean laboratory for samples such as human livers and marine specimens as well as food products. These kinds of samples are banked because they are excellent indicators of pollution contamination at a particular time and location. Human livers, for example, are collected because they act as "sponges" in which toxic chemicals accumulate. Project researchers store samples at liquid nitrogen temperatures and can withdraw these materials at any time for reliable analysis. By periodically analyzing banked specimens, scientists can examine pollution trends.

For details on obtaining the videotape, contact Dr. Stephen Wise, A113 Chemistry Building, National Bureau of Standards, Gaithersburg, MD 20899, 301/975-312.

Standard Reference Materials

NEW SRMS FOR CHOLESTEROL IN SERUM

In cooperation with the College of American Pathologists (CAP) and the Centers for Disease Control (CDC), NBS has recently completed measurements for certification of cholesterol in new serum-based materials to be issued as Standard Reference Materials (SRMs). The measurements are made using a "definitive method," i.e., a method shown to provide highly precise results with no known sources of bias. The technique employed in this method is isotope dilution mass spectrometry. This highly specialized technique is beyond the capabilities of most clinical laboratories and would be too costly and time consuming to be used directly on patients' samples. However, the laboratories can use the SRMs certified by this technique to evaluate the accuracy of their routine methods. The new SRMs are in two forms: SRM 1951 consists of three vials of frozen serum supplied by CDC at 210, 242, and 282 mg/dL; SRM 1952, supplied by CAP, consists of three vials of lyophilized serum which when reconstituted have levels of 207, 262, and 357 mg/dL. These new materials cover the range in which most medical decisions concerning cholesterol risk factors are being made and should provide clinical laboratories with a much needed accuracy base.

Each of these SRMs costs $150, plus the cost of our shipment in insulated boxes. These SRMs can be ordered from the Office of Standard Reference Materials, B311 Chemistry Building, National Bureau of Standards, Gaithersburg, MD 20899, 301/975-6776.

DRUGS-OF-ABUSE-IN-URINE SRM

In an effort to provide reference materials for the drug testing community, NBS has prepared and certified the first of a series of urine-based SRMs. SRM 1507 is a freeze-dried urine fortified with 11-nor-Δ^9-tetrahydrocannabinol-9-carboxylic acid (THC-9-COOH), the major urinary metabolite of marijuana. Each unit of SRM 1507 consists of three bottles of freeze-dried urine: two bottles containing, after reconstitution, THC-9-COOH at the certified concentration of 20 ± 1 ng/mL and one bottle of a urine blank. The certified value for the analyte was obtained from the concordant results of two independent NBS analytical methods: 1) solid phase extraction followed by gas chromatography/mass spectrometry (GC/MS); and 2) liquid-liquid extraction followed by high-performance liquid chromatography (HPLC) with electro-chemical detection.

A limited round robin exercise using SRM 1507 as an unknown was conducted among five Department of Defense laboratories engaged in drug testing. The reported results ranged from 17.7 to 21.0 ng/mL, with an average concentration of 20.8 ng/mL and the standard deviation of a single measurement among the laboratories being 1.0 ng/mL.

SRM 1507, which costs $159, is intended primarily for verifying the accuracy of methods used for the determination of THC-9-COOH in human urine. The concentration of the reconstituted SRM is near the decision level for THC-9-COOH in urine that is used by the DOD and many government and private institutions. This SRM should be useful in addressing some of the legal and scientific issues surrounding substance abuse and its detec-

tion and treatment. A cocaine-in-urine SRM is being developed currently and urine-based SRMs for other drugs of abuse are planned.

This SRM can be ordered from the Office of Standard Reference Materials, B311 Chemistry Building, National Bureau of Standards, Gaithersburg, MD 20899, 301/975-6776.

SRM CATALOG AVAILABLE

A new catalog lists nearly 1000 SRMs available from NBS. The SRMs, certified by NBS for specific chemical and physical properties, help scientific, industrial, and commercial users to achieve quality assurance of materials and goods. These materials include cements, ores, metals, glasses, plastics, food, environmental, and clinical items. The new catalog contains an improved alphabetical index and a complete numerical listing of the latest renewal SRMs and their certificate dates. It includes a description of the reference material, its certified characterization, and unit size.

Ordering and shipping information is also included; prices for the SRMs are published separately in annual supplements. Copies of the new catalog are available free-of-charge from the Office of Standard Reference Materials, B311 Chemistry Building, National Bureau of Standards, Gaithersburg, MD 20899, 301/975-6776.

Calendar

April 10–15, 1988

RESONANCE IONIZATION SPECTROSCOPY AND ITS APPLICATIONS (RIS '88)

Location: National Bureau of Standards
Gaithersburg, MD

The RIS '88 Symposium is a major focal point for presenting the results of multidisciplinary research involving resonance ionization phenomena and related laser applications. The program will consist of posters, contributed and invited papers, and plenary lectures on the following topics: (1) Photophysics and Spectroscopy, (2) Resonance Ionization Mass Spectrometry (RIMS), (3) Molecular Resonance Ionization Spectroscopy, (4) Noble Gas Atom Counting, (5) Analysis of Materials and Surfaces, (6) Medical and Environmental Application, (7) Optical Sources, (8) Atom Reservoirs and Sampling, (9) Physics Applications—including Elementary Particles and Nuclear Processes, (10) Chemical Applications—including Diffusion, Reaction Rates, and Clustering.

This symposium is organized by an International Advisory Group through an appointed Program Committee and is sponsored by the Department of Energy, the University of Tennessee, the National Bureau of Standards, the International Union of Pure and Applied Physics, EG&G, and Battelle Northwest Laboratories.

Contact: Thomas B. Lucatorto, A243 Physics Building, National Bureau of Standards, Gaithersburg, MD 20899, 301/975-3734.

April 13–15, 1988

4th INTERNATIONAL CONFERENCE ON METROLOGY AND PROPERTIES OF ENGINEERING SURFACES

Location: National Bureau of Standards
Gaithersburg, MD

Metrology and properties of engineering surfaces have continued to assume great importance to both the practicing engineer and the researcher. In recent years, industry has gained increased awareness of the importance of surface preparation techniques. This international conference is the 4th in a series of meetings on the subject of metrology and properties of engineering surfaces which have been held every 3 years since 1976. The main topics to be discussed at this meeting will be: the application of new surface techniques in industry, the development of new tactile instruments, the development of new techniques for the optical measurement of engineering surfaces, the compilation and analysis of data for specific manufacturing processes, and the relationships between surface generation and practical performance. This conference is sponsored by the National Bureau of Standards, Coventry Polytechnic, and Whitestone Business Communications.

Contact: Professor K. J. Stout, Coventry Polytechnic, Department of Manufacturing Systems, Priory Street, Conventry CV1 5FB, England, 0203 24166, ext. 278; or Dr. T. V. Vorburger, A117 Metrology Building, National Bureau of Standards, Gaithersburg, MD 20899, 301/975-3493.

April 21–22, 1988
WORKSHOP ON MICROSTRUCTURE AND MACROMOLECULAR RESEARCH WITH COLD NEUTRONS

Location: National Bureau of Standards
Gaithersburg, MD

In order to inform and involve the community of scientific researchers at an early stage in the development of the Cold Neutron Research Facility (CNRF), NBS is hosting a series of workshops which will each focus on a major area of cold neutron research. This workshop on "Microstructure and Macromolecular Research with Cold Neutrons" will focus on scientific opportunities in the study of submicron structures in materials, including macromolecular structures in polymers and biomaterials, which arise from experimental techniques which take special advantage of cold neutron.

Technical talks by invited speakers will review current work in a variety of disciplines and discuss future extensions utilizing cold neutrons. Specific instruments and techniques related to characterizing submicron structures in materials will also be discussed. An important part of the workshop will be the active participation of the attendees in assessing the capabilities of and the need for various types of instrumentation for the CNRF. The workshop will thus afford potential users a unique opportunity to explore the capabilities of the CNRF and to guide its development.

The meeting is sponsored by the National Bureau of Standards.

Contact: Charles J. Glinka, B106 Reactor Building, National Bureau of Standards, Gaithersburg, MD 20899, 301/975-6242.

May 10–11, 1988
CONFERENCE ON UNCERTAINTY IN ENGINEERING DESIGN

Location: National Bureau of Standards
Gaithersburg, MD

Designing for Quality and Reliability is the focus of this conference. The aim is to provide an opportunity for engineers and statisticians to explore approaches to handling uncertainty in design and manufacturing. The conference will facilitate the interaction of these disciplines in the context of both product and process design. The program will include invited talks and open discussion led by selected participants. Attendees will also have an opportunity to tour the NBS Advanced Manufacturing Research Facility (AMRF). Sponsored by the George Washington University, the National Science Foundation, the Army Research Office, the Office of Naval Research, the Air Force Office of Scientific Research, and the National Bureau of Standards, with the cooperation of the American Statistical Association.

Contact: Shirley Bremer, A337 Administration Building, National Bureau of Standards, Gaithersburg, MD 20899, 301/975-2845.

June 9, 1988
TWENTY-SEVENTH ANNUAL TECHNICAL SYMPOSIUM OF THE WASHINGTON, DC, CHAPTER OF THE ASSOCIATION FOR COMPUTING MACHINERY
Productivity: Progress, Prospects, and Payoff

Location: National Bureau of Standards
Gaithersburg, MD

Productivity is a key issue in the information industry. Information technology must provide the means to maintain and enhance productivity. This symposium will explore the theoretical and practical issues in developing and applying technology in an information-based society. "How productive are we?"—"How productive can we become?"—"What are the inhibitors and facilitators?" Topics to be discussed include: software; hardware system considerations; economic considerations; labor and the workplace; capture and use of expertise; artificial intelligence and knowledge-based systems; and building, testing, and maintaining systems. Sponsored by the Washington, DC, Chapter of ACM and the National Bureau of Standards.

Contact: Wilma Osborne, B266 Technology Building, National Bureau of Standards, Gaithersburg, MD 20899, 301/975-3339.

June 20–23, 1988
10th SYMPOSIUM ON THERMOPHYSICAL PROPERTIES

Location: National Bureau of Standards
Gaithersburg, MD

This Symposium is the 10th in a well-established series of conferences on thermophysical properties. It will address theoretical, experimental, and

applied aspects of thermophysical properties for gases, liquids, and solids. Appropriate topics to be included in the symposium include Thermodynamic Properties, Transport Properties, Optical and Thermal Radiative Properties, Interface Properties, and Data Correlation. Special topics to be included in the symposium are Properties of New Materials, Properties of Gaseous and Liquid Mixtures, New Developments in Experimental Techniques, and Interpretation of Experimental Data in Terms of New Theoretical Developments. Also included in the symposium is the "First Workshop on Subsecond Thermophysics."

Contact: Dr. A. Cezairliyan, Room 124 Hazards Building, National Bureau of Standards, Gaithersburg, MD 20899, 301/975-5931; or Dr. J. V. Sengers, Institute for Physical Science and Technology, University of Maryland, College Park, MD 20742, 301/454-4117.

Volume 93, Number 2, March–April 1988
Journal of Research of the National Bureau of Standards

Measurement of the Universal Gas Constant R Using a Spherical Acoustic Resonator

Volume 93 Number 2 March–April 1988

M. R. Moldover, J. P. M. Trusler[1], and T. J. Edwards[2]
National Bureau of Standards
Gaithersburg, MD 20899

J. B. Mehl
University of Delaware
Newark, DE 19716

and

R. S. Davis
National Bureau of Standards
Gaithersburg, MD 20899

We report a new determination of the Universal Gas Constant R: (8.314 471 ±0.000 014) J·mol^{-1}K^{-1}. The uncertainty in the new value is 1.7 ppm (standard error), a factor of 5 smaller than the uncertainty in the best previous value. The gas constant was determined from measurements of the speed of sound in argon as a function of pressure at the temperature of the triple point of water. The speed of sound was measured with a spherical resonator whose volume was determined by weighing the mercury required to fill it at the temperature of the triple point. The molar mass of the argon was determined by comparing the speed of sound in it to the speed of sound in a standard sample of argon of accurately known chemical and isotoptic composition.

Key words: argon; fundamental constants; ideal gas; mercury; molar gas constant; R; resonator; speed of sound; spherical resonator; temperature; thermometry; Universal Gas Constant.

Accepted: October 30, 1987

Contents

[1] Present address: Department of Chemistry, University College London, 20 Gordon Street, London WC1H OAJ, United Kingdom.

[2] Present address: School of Mathematical and Physical Sciences, Murdoch University, Murdoch WA 6150, Australia.

1. Introduction

With readily available technology (such as triple point cells and platinum resistance thermometers), it is possible to define and reproduce states of particular temperatures with much greater precision than it is possible to measure the fundamental statistical mechanical quantities characterizing such states (such as the average energy in each degree of freedom of a many body system or the derivative of the internal energy with respect to the entropy at constant volume). Accordingly, the International System of Units (SI) has defined temperature as an independent physical quantity and the kelvin (K) as the unit of that quantity. The definition specifies that the temperature T_t of the triple point of water is exactly 273.16 K. Having made this specification, one can define the Boltzmann constant k, as the ratio $2E/T_t$ and one can define the universal gas constant R, as the ratio $2EN_A/T_t$. (Here E is the average kinetic energy in a single

mechanical degree of freedom at T_t and N_A is the Avogadro constant.) In this work we have re-determined R with the result:

$$R = (8.314\ 471 \pm 0.000\ 014)\ \text{J/(mol·K)}$$

$$(1.7\ \text{ppm}), \tag{1.1}$$

where the error quoted is a standard deviation. From this new value of R one can obtain improved values of the Boltzmann constant:

$$k = R/N_A = (1.380\ 651\ 3 \pm 0.000\ 002\ 5)$$

$$\times 10^{-23}\text{J/K} \quad (1.8\ \text{ppm}), \tag{1.2}$$

and the Stefan-Boltzmann constant σ:

$$\sigma = 2\pi^5 k^4/(15h^3c^2) = 2\pi^5 R^4/[15N_A(N_A h)^3 c^2]$$

$$= (5.670\ 399 \pm 0.000\ 038) \times 10^{-8}\text{W/(m}^2\text{·K}^4\text{)}$$

$$(6.8\ \text{ppm}). \tag{1.3}$$

Here, we have used the values of N_A, the Planck constant h, and the more accurately known molar Planck constant $N_A h$ resulting from the 1986 adjustment of the fundamental physical constants [1].

The present value of R is compared with other recent determinations of R in figure 1. Our value is consistent with previous values; however, it is 5 times more accurate than the best previous value. [The same is true for the values of k and σ given in eqs (1.4) and (1.5).] This higher accuracy will be most useful for primary thermometry (e.g., gas, noise, acoustic, and radiation thermometry) with thermometers whose design does not permit them to be used at T_t where the temperature scale is defined. Further details concerning the roles of R in metrology and the methods used in prior determinations of R have been reviewed by Colclough [2] in 1984 and will not be repeated here.

We conclude this introduction with a summary of the errors in our redetermination of R, the prospects for further improvements, and a brief list of the technical advances developed in this work. For these purposes it is useful to present a highly simplified equation relating R to the quantities actually measured in the laboratory.

Our redetermination of R is based on a new measurement of the speed of sound in a well-characterized sample of argon at T_t. Elementary

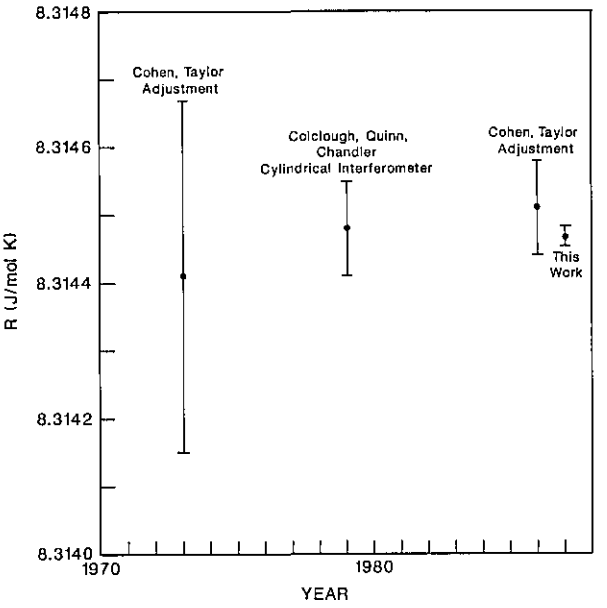

Figure 1. Recent values of R. The values from Cohen and Taylor [1] are adjustments. The value from Colclough et al. [13] was obtained with a cylindrical acoustic resonator.

considerations of hydrodynamics and the kinetic theory of dilute gases lead to the relations:

$$\frac{1}{2}mv_{rms}^2 = \frac{3}{2}kT, \quad c^2 = \frac{\gamma}{3}v_{rms}^2. \tag{1.4}$$

(Here v_{rms}^2 is the mean square speed of the molecules, m is the mass of one molecule, c is the speed of sound, and γ is the ratio of the specific heat capacities C_p/C_V and has the value $\gamma_0 = 5/3$ for dilute monatomic gases.) Thus, a measurement of the speed of sound in a dilute monatomic gas at T_t is a measurement of the v_{rms} at T_t and it would be a measurement of k if m were known accurately. In practice the relative values of isotopic masses are extremely well known on a scale of atomic mass units but the knowledge of m for any *pure* gas is limited by the uncertainty in N_A, the constant which relates the atomic mass unit to the kilogram and also relates the mass m of a molecule to the molar mass M [3].

In this work the speed of sound was deduced from measurements of the internal volume of a spherical shell and the frequencies f_{0n} of the radially-symmetric acoustic resonances when the shell was filled with argon. There is a well-developed theory for such resonances [4–10] which has been confirmed by detailed experiments [9–11]. The fre-

quencies of the radially-symmetric modes are insensitive to geometric imperfections that leave the internal volume of the shell unchanged [4–6]. Thus, accurate internal dimensional measurements were not required. The internal volume V was determined by weighing the quantity of mercury required to fill the shell completely at T_t. R is related to the frequencies, volume, and the molar mass by the equations:

$$R=\frac{c_0^2 M}{T_t \gamma_0}=\frac{1}{T_t}\left(f_{0n}/\nu_{0n}\right)^2 V^{2/3}\frac{M}{\gamma_0}. \tag{1.5}$$

(ν_{0n} is the eigenvalue z_{0n} multiplied by the factor $(6\pi^2)^{-1/3}$ and is known exactly and c_0^2 is the zero-pressure limit of the speed of sound.)

Table 1 lists the important contributions to the standard error of R from the measurements of the quantities in eq (1.5). We now consider them in turn.

Table 1. One-sigma uncertainties (in parts per million) from various sources in the redetermination of R

I	$(\text{Volume})^{2/3}$	
	density of mercury at 20 °C	0.28
	storage and handling of mercury	0.20
	thermal expansion of mercury (0–20 °C)	0.67
	random error of volume measurements	0.20
	corrections from weighing configuration to acoustics configuration	0.10
	mass of counterweights	0.14
II	Temperature	
	random error of calibrations	0.8
	temperature gradient	0.4
III	M/γ_0	
	Ar-40 standard	0.7
	comparison of working gas to Ar-40	0.4
IV	Zero-pressure limit of $(f_{0n}/\nu_{0n})^2$	
	s.d. of c_0^2 from 70 observations at 14 pressures	0.68
	thermal boundary layer correction (0.3% of thermal conductivity)	0.30
	possible error in location of transducers	0.55
	Square root of the sum of the squares	1.7

The uncertainty in the volume determination is dominated by our imperfect knowledge of the thermal expansion of mercury between T_t and 20 °C. The random error of the volume determinations is only 0.29 ppm and it contributes 0.20 ppm to the standard error in R. It is unusual for an assembled artifact of this size (3 liters) to have such a reproducible internal volume.

In the present work, capsule platinum resistance thermometers were calibrated at T_t and then inserted in the enclosed acoustic apparatus. The dominant uncertainty in the thermometry resulted from drifts in the thermometers and/or the bridge used with them during the weeks between calibrations. This uncertainty could be greatly reduced by designing an acoustic apparatus which permitted rapid insertion and removal of calibrated thermometers.

In the present work, M/γ_0 was deduced from measurements of the concentrations of the isotopic argon species and noble gas impurities in a standard sample of nearly monoisotopic ^{40}Ar. Routine gas chromatographic techniques were used to measure the concentrations of the noble gas impurities in the standard sample. The detection limit for xenon led to the 0.7 ppm uncertainty in M/γ_0. This source of uncertainty could certainly be reduced in future work. The spherical acoustic resonator was used to compare the speed of sound in the standard sample with that in working samples of argon. The comparison had an imprecision of only 0.2 ppm; thus, the ratio of the average molar masses of the argon samples could be determined with an imprecision of 0.4 ppm.

The errors in the measurements of the resonance frequencies are quite small; however, the zero-pressure limit of $(f_{0n}/\nu_{0n})^2$ was determined by fitting a 4-parameter function of pressure to the measured frequencies in the pressure range 25–500 kPa. The correlations among the 4 parameters contributed an uncertainty of 0.68 ppm to c_0^2 [which is the zero-pressure limit of $(f_{0n}/\nu_{0n})^2$ multiplied by $V^{2/3}$]. This uncertainty could be reduced by increasing the signal-to-noise ratio of the acoustic measurements, particularly at the lower pressures.

The resonance frequencies are perturbed by the presence of a thermal boundary layer (roughly 50 μm thick) in the gas in contact with the shell. This perturbation is proportional to the square root of the thermal diffusivity. Thus, it varies as $(f_{0n}p)^{-1/2}$ at low pressures and it ranges from 40–360 ppm. The perturbation has been calculated from independent information about the thermal conductivity of argon. We estimate the uncertainty in the thermal conductivity to be 0.3% and this propagates into a 0.30 ppm uncertainty in the zero-pressure limit of $(f_{0n}/\nu_{0n})^2$ and in R. The same boundary layer makes the dominant contribution to the widths of the resonances. At low pressures the measured and calculated widths of the resonances are in agreement, which confirms the perturbation calculation.

The final contribution to the uncertainty in the zero-pressure limit of $(f_{0n}/\nu_{0n})^2$ resulted from a possible problem in defining the location of one transducer during some of the frequency measurements and could have been eliminated if the opportunity to repeat these measurements were available.

In summary, straightforward modifications of the present measurements might reduce the uncertainty in R somewhat, but probably by less than a factor of 2. Further improvement would require two developments: 1. new transducers with improved signal-to-noise characteristics (without degrading the other characteristics required by the measurement), and 2. either a better value for the density of mercury at T_1 or a better method of measuring the resonator's volume. Microwave measurements are a promising alternative to weighing mercury for volume measurements. A theorem derived by two of us (JBM and MRM) suggests a strategy for doing this with high accuracy using comparatively few microwave resonances in a spherical cavity constructed with ordinary machine shop tolerances [12].

Prior to the present measurements, the most accurate determination of R was that of Colclough, Quinn, and Chandler [13]. Their work was also based on measurements of the speed of sound in dilute argon. We shall briefly contrast the two acoustic measurements.

Colclough et al. used a variable-pathlength, cylindrical interferometer operating at 5.6 kHz. They used optical techniques to measure the displacement required of one end of the interferometer to achieve successive longitudinal resonances. In contrast, we have used a spherical resonator of fixed dimensions which was operated near five different radially-symmetric modes at frequencies in the range 2.5–9.5 kHz. Our gravimetric volume determination takes the place of their displacement measurement.

The corrections to the resonance frequencies arising from boundary layers were a factor of 10 smaller for the radial modes in the 18-cm diameter sphere than for the longitudinal modes in the 3-cm diameter cylinder. Because the radial corrections were smaller they could be calculated with sufficient accuracy from independent measurements of the transport properties. The calculations were confirmed by acoustic measurements of the half-widths of the resonances.

The resonances in the sphere were a factor of 10 narrower than in the cylinder. This enabled us to use smaller (6-mm diameter) transducers which perturbed the radially symmetric resonances in a minor and easily calculable fashion while attaining a satisfactory signal-to-noise ratio. In contrast, a larger electroacoustic transducer formed one end of the cylindrical interferometer. The large transducer exhibited nonlinear behavior which caused problems in interpretation of the acoustic data.

In the present work, we have accounted for the effects of the finite elastic compliance of the resonator's wall and for the incomplete thermal accommodation of the gas at the wall, two phenomena which were not considered by Colclough et al. (The compliance produces a perturbation which is linear in the pressure; thus it does not affect R.)

The primary divisions of the remainder of this manuscript are: 2. Theoretical Basis of the Measurement, 3. Fabrication and Characterization of the Resonator, 4. Measuring Resonance Frequencies, 5. Thermometry, 6. Determination of the Resonator's Volume, 7. Determination of M/γ_0, 8. The Pressure and Other Thermodynamic and Transport Properties, 9. Determination of c_0^2 in the Working Gas, 10. Other Tests for Systematic Errors, and 11. Summary.

2. Theoretical Basis of Measurement

2.1 Introduction

In this section we describe the acoustical model of the spherical resonator. The model includes a calculation of the response of the gas and the shell to excitation by a steady sinusoidal source, and also includes calculation of the fundamental resonance parameters which appear in the response function. It is convenient to assume that all of the "small" quantities of linear acoustics are proportional to $e^{i\omega t}$, and to obtain solutions in the form of linear combinations of appropriate eigenfunctions. In the following development, we assume the eventual inclusion of a source term whose strength and frequency remain constant long enough for the system to reach a steady state.

We begin with a zero-order description of the acoustics of the gas-filled resonator. This description is not complete enough for calculations of the required accuracy, but it is the simplest way to introduce the basic concept and language used in the complete model. Let the acoustic field in the gas be described by a velocity potential $\Psi(r)$, which is related to the particle velocity u through

$$u(r)=\nabla\Psi(r). \tag{2.1}$$

If the dynamics of the gas are governed by the Euler equation, and an adiabatic equation of state is used for the gas, then the acoustic pressure p' is related to the velocity potential through

$$p'(r) = -i\omega\rho\Psi(r), \tag{2.2}$$

where ρ is the mass density of the gas. The velocity potential satisfies the steady-state wave equation

$$(\nabla^2 + k^2)\Psi(r) = 0, \tag{2.3}$$

where c is the speed of sound, and $k = \omega/c$. The regular solutions of eq (2.3) in spherical coordinates have the form

$$\Psi(r) \propto j_l(kr) Y_{lm}(\theta,\phi), \tag{2.4}$$

where $j_l(z)$ is a spherical Bessel function and Y_{lm} is a spherical harmonic. In a spherical shell which is perfectly rigid and insulating, free vibrations of the gas are permitted at frequencies such that the radial particle velocity vanishes at the inner shell wall ($r = a$). These frequencies, which will be referred to as the unperturbed eigenfrequencies, are given by

$$f_{ln}^0 = cz_{ln}/(2\pi a). \tag{2.5}$$

where $z_{ln} = k_{ln}a$ is the nth root of the equation $\frac{dj_l(z)}{dz} = 0$. Note that the unperturbed eigenfrequencies are independent of the mode index m; for each pair of indices ln there are $2l+1$ modes with the same frequency f_{ln}^0. The modes with $l = 0$ are nondegenerate; they will be referred to as the radial modes. They have numerous special properties which make them most suitable for use in high-accuracy acoustical measurements. According to the conventional numbering of roots of Bessel functions, the first $l = 0$ root is designated $z_{01} = 0$. The (0,2) through (0,6) radial modes were used in the present work. For argon at 273.16 K in the resonator used in this work, the range of frequencies is between $f_{02}^0 = 2476$ Hz and $f_{06}^0 = 9490$ Hz. In specifying the numerical values of quantities for argon, it will be convenient to use the dimensionless quantities $\tilde{f} \equiv f/f_{02}^0$ and $\tilde{p} \equiv p/(100\ \text{kPa})$. The present measurements span the range $1 < \tilde{f} < 4.5$ and $0.25 < \tilde{p} < 5.0$.

The unperturbed eigenfrequencies are proportional to the ratio of the speed of sound to the radius of the resonator. Measurement of an unperturbed eigenfrequency and the radius of the sphere gives a value for the speed of sound. This is the basic principle of our measurement. We made high-precision measurements of the experimental eigenfrequencies of the system. These must be related to the speed of sound and the mean resonator radius by a more complete model of the acoustical system. A description of this model is given in the remainder of this section. The model predicts complex eigenfrequencies $F_N = f_N + ig_N$, where N is shorthand for the notation using multiple indices. The complex eigenfrequency differs from the corresponding unperturbed value f_{ln}^0 in both the real and imaginary parts. The imaginary part represents the losses; it can be observed experimentally either as the halfwidth of a resonance curve or the decay constant of free oscillations.

The most complete derivation of the relevant theory is presented in Moldover, Mehl, and Greenspan [9]. Their model is incomplete in one respect, however. They use a boundary condition for the temperature at the shell boundary which is not sufficiently accurate at the lowest experimental pressures. This effect was analyzed by Ewing, McGlashan, and Trusler [10]. It is incorporated in the description of the theoretical model presented here.

2.2 Basic Equations

The basis of the theoretical model is a set of equations first derived by Kirchhoff in 1868 [14,15]. For completeness, we indicate the nature of the fundamental assumption and the use of constitutive relations in the following. The dynamics of the gas are described by the Navier-Stokes equation, which consists of Newton's second law and a constitutive relation giving the stresses in terms of the spatial derivatives of the velocity of the gas. The relevant kinetic coefficient is the shear viscosity η. Heat flow in the gas is assumed to be governed by Fourier's law; the relevant kinetic coefficient is the coefficient of thermal conductivity λ. Two additional equations are statements of the equation of continuity for mass flow and for heat flow. An equation of state for the gas is used to relate changes in pressure, density, and temperature. The second law of thermodynamics is also used to relate changes in the entropy of the gas to temperature and pressure variations. These principles are used to construct a linear acoustic theory. That is, the squares and products of certain "small" quantities are neglected in the equations. Let the pressure, temperature, and density be represented by $p + p'(r)$, $T + \tau(r)$, and $\rho + \rho'(r)$, where p, T,

and ρ are the ambient quantities, and $p'(r)$, $\tau(r)$ and $\rho'(r)$ are small terms with the assumed time dependence. The equations of motion couple these fields with each other and with the longitudinal particle velocity $u(r)$. Kirchhoff found that $\tau(r)$ was governed by a fourth order partial differential equation which may be written in the form

$$(i\delta_t^2/2)[1+(i\gamma/2)(\omega\delta_v'/c)^2]\nabla^4\tau + [1+(i/2)(\omega/c)^2(\gamma\delta_t^2+\delta_v'^2)]\nabla^2\tau + (\omega/c)^2\tau=0. \quad (2.6)$$

The characteristic lengths in this equation are the thermal penetration length

$$\delta_t=\sqrt{2D_t/\omega}, \quad (2.7)$$

the viscous penetration length

$$\delta_v=\sqrt{2D_v/\omega}, \quad (2.8)$$

and a supplementary quantity δ_v' which is related to the viscous penetration length and the bulk viscosity η_b by

$$\delta_v'^2=\frac{4}{3}\delta_v^2+\eta_b/\rho. \quad (2.9)$$

In these equations the thermal diffusivity D_t is equal to the ratio of the thermal conductivity to the constant-pressure specific heat capacity per unit volume $\lambda/(\rho C_p)$, and the viscous diffusivity $D_v=\eta/\rho$ is equal to the ratio of the viscosity to the density. For argon at 273.16 K approximate values for these lengths are $\delta_t=47.6\ \mu\text{m}(\tilde{f}\tilde{p})^{-1/2}$, $\delta_v=38.8\ \mu\text{m}(\tilde{f}\tilde{p})^{-1/2}$, and $\delta_v'=44.8\ \mu\text{m}(\tilde{f}\tilde{p})^{-1/2}$. (For argon and other monatomic gases, the bulk viscosity term is negligible; it is included here for completeness.)

The pressure is related to the temperature through

$$p'(r)=\frac{\gamma\alpha}{\gamma-1}\left[1-\frac{\delta_t^2}{2i}\nabla^2\right]\tau(r), \quad (2.10)$$

where $\gamma=C_p/C_V$ is the ratio of the specific heat capacities and $\alpha=(\partial p/\partial T)_V$. The longitudinal particle velocity $u(r)$ is related to the pressure and temperature by

$$i\omega\rho u=-\nabla[p'+(i\gamma/2)(\omega\delta_v'/c)^2(p'-\alpha\tau)]. \quad (2.11)$$

A divergence-free component of the velocity is also needed in the complete theory. This component is necessary to describe the shear waves which couple to nonradial modes through the boundary conditions. It is not needed in the present discussion, which will be restricted to radial modes.

Equation (2.6) separates into

$$(\nabla^2+k_p^2)(\nabla^2+k_t^2)\tau(r)=0, \quad (2.12)$$

where k_p^2 and k_t^2 are the roots of a bi-quadratic equation whose coefficients can be determined from eq (2.6). The quantities k_p and k_t will be referred to as the propagation parameters for the acoustic and thermal modes. Exact expressions for k_p^2 and k_t^2 can be obtained from the bi-quadratic equation. The following series expansions of the exact solutions are, however, more useful:

$$k_p^2=(\omega/c)^2\{1-(i/2)(\omega/c)^2[(\gamma-1)\delta_t^2+\delta_v'^2] + O(\omega\delta/c)^4\} \quad (2.13)$$

$$k_t^2=(-2i/\delta_t^2)\{1+(i/2)(\omega/c)^2(\gamma-1)(\delta_t^2-\delta_v'^2) + O(\omega\delta/c)^4\}. \quad (2.14)$$

The notation here indicates that the solutions are correct to fourth order in the ratio of any of the characteristic lengths δ to the wavelength of an acoustic wave.

Solutions of eq (2.12) for the temperature which are finite at the origin and radially symmetric have the form

$$\tau(r)=\tau_p j_0(k_p r)+\tau_t j_0(k_t r). \quad (2.15)$$

The propagation parameter for the thermal mode is approximately equal to $(1-i)/\delta_t$. Thus the argument $k_t r$ is generally sufficiently large that the asymptotic form for $j_0(k_t r)$ can be used; the magnitude of the asymptotic form is approximately $\exp(r/\delta_t)/(r/\delta_t)$, which decays rapidly with decreasing r. The thermal wave solution is thus significant only within a few thermal penetration lengths δ_t of the shell wall. The pressure corresponding to eq (2.15) is

$$p'(r)=\frac{\gamma\alpha}{\gamma-1}\left[\tau_p\left(1+\frac{\delta_t^2k_p^2}{2i}\right)j_0(k_p r) + \tau_t\left(1+\frac{\delta_t^2k_t^2}{2i}\right)j_0(k_t r)\right], \quad (2.16)$$

and the longitudinal particle velocity is given by

$$\rho c u(r)=\frac{ic}{\omega}\frac{\gamma\alpha}{\gamma-1}\nabla[F(k_p^2)\tau_p j_0(k_p r) + F(k_t^2)\tau_t j_0(k_t r)], \quad (2.17)$$

where

$$F(k^2)\equiv 1+(i/2)(\omega\delta_v'/c)^2-(i/2)(k\delta_t)^2 + (\gamma/4)(\omega\delta_v'\delta_t k/c)^2. \quad (2.18)$$

Equation (2.13) can be inverted to give a classical Navier-Stokes dispersion relation for ω as a function of k_p. Corrections to the Navier-Stokes dispersion relation have been derived from approximate solutions to the Boltzmann equation in the form of an ascending series in the variable $x\equiv\Lambda k$, where Λ is the mean free path [16]. These corrections are consistent with ultrasonic measurements in gases at low pressures [17], and if they were applied to the pressure regime of the present experiment they would be negligible. More recently, it has been argued that the scaled dispersion relation (ω divided by a collision frequency considered as a function of x) has corrections proportional to $x^{1/2}$ with an amplitude on the order of (density/close-packed density)^2 for a hard-sphere gas [18]. If the hard-sphere estimate is roughly applicable to argon, the more recent corrections are also negligible in the regime of the present work where x ranges from 10^{-6} to 5×10^{-5} and the density ranges from 3×10^{-4} to 6×10^{-3} of the density of liquid argon.

2.3 Boundary Conditions

There are four boundary conditions to be satisfied by radial modes at the gas-shell interface ($r=a$). First, the radial components of the gas and shell velocities must match. Second, the radial component of the shell velocity is proportional to the radial force per unit area exerted on it by the gas times an effective acoustic admittance β_{sh}. Two additional boundary conditions deal with thermal effects at the gas-shell interface. These effects occur uniformly over the boundary. In this section it will be shown that these effects lead to a single equation which determines the complex eigenfrequencies. Shell motion and thermal boundary effects shift the eigenfrequencies from the unperturbed values f_{0n}^0. Other sources of eigenfrequencies shifts, such as transducers, small openings, and imperfect geometry will be discussed in subsequent sections.

The force per unit area acting on the shell differs from the acoustic pressure by a fractional amount of order $(\omega\delta/c)^2$, which we neglect [9]. The first two boundary conditions can then be written

$$(\rho c u_r/p)_{r=a}=\beta_{sh}(\omega). \quad (2.19)$$

An expression for the admittance of an idealized shell was derived in reference [9]. Several assumptions made in reference [9] differ from the conditions of the experiment. The derivation is based on the theory of elasticity for isotropic materials. It applies to a uniform spherical shell, not a composite structure fabricated from parts. The experimental shell does not have a uniform thickness. The derivation neglects mechanical coupling between the shell and its environment. (Radiation of sound from the outer boundary of the shell was included in the calculation, however, and shown to be negligible.) Despite the differences between the idealized shell and the present experimental shell, the predicted effects of shell motion are sufficiently small that an approximate calculation is adequate for the determination of R. [The calculation was tested by measurements of the shell's compliance (secs. 6.8.1–6.8.3) and the frequency of its breathing mode (sec. 3.8).]

The acoustic admittance of the shell was found to be

$$\beta_{sh}=[-i\rho\omega ca/(\rho_{sh}c_{sh}^2)]S_0(k_{sh}a), \quad (2.20)$$

where ρ_{sh} is the shell density, c_{sh} is the speed of longitudinal waves in the bulk shell material, $k_{sh}=\omega/c_{sh}$, and the function S_0 is

$$S_0=-q\times\frac{(1+AB-qB^2)\tan(B-A)-(B-A)-qAB^2}{[(qA^2-1)(qB^2-1)+AB]\tan(B-A)-(1+qAB)(B-A)} \quad (2.21)$$

where the outer shell radius is b, $A=k_{sh}a$, $B=k_{sh}b$, and the parameter q is related to Poisson's ratio σ through $q=(1/2)(1-\sigma)/(1-2\sigma)$. The radial shell resonances occur at frequencies for which the denominator of eq (2.21) vanishes. The lowest such resonance will be referred to as the breathing resonance of the shell; its frequency will be designated f_{br}. For the shell used in this work the breathing resonance occurs at approximately 13.58 kHz. All other shell resonances occur at much higher frequencies. Accordingly, an excellent approximation to eq (2.21) is obtained by taking the zero-frequency limit of eq (2.21) and dividing by the resonance term $1-(f/f_{br})^2$. This approximation gives

$$S_0=-q\frac{3qab^2-3bh(a-qb)-h^3}{3qh(a^2+ab+b^2)-3abh-h^3}\frac{1}{1-(f/f_{br})^2}. \tag{2.22}$$

The third boundary condition at the gas-shell interface deals with the temperature of the gas and the shell. In previous work, Moldover, Mehl, and Greenspan assumed that the temperatures of the gas and wall were equal at the interface [9]. However, Ewing, McGlashan, and Trusler [10] have shown that at low densities a temperature discontinuity should be included in the boundary condition. According to kinetic theory, [19–21] the temperature of the gas (extrapolated to the wall) should exceed that of the shell by

$$\Delta\tau=J_t l_a/\lambda_g, \tag{2.23}$$

where J_t is the normal heat flux across the interface, l_a is the accommodation length in the gas, and λ_g is the thermal conductivity of the gas. The accommodation length is given by

$$l_a=\frac{\lambda_g}{P}\sqrt{\frac{\pi MT_g}{2R}}\frac{(2-h)/h}{C_V/R+1/2}, \tag{2.24}$$

where M is the molar mass of the gas, T_g is the temperature of the gas, R is the gas constant, C_V is the molar specific heat at constant volume of the gas, and h is the thermal accommodation coefficient. Ewing, McGlashan, and Trusler found that the thermal accommodation coefficient between argon and the machined aluminum wall of their resonator was 0.84 ± 0.05. Values near unity are apparently typical for heavier gases and machined surfaces which have not been vacuum-flashed in ultra-high vacuums [20–23]. With $h=1$, the accommodation length of argon at 273.16 K and 100 kPa is 118 nm.

For the first thermal boundary condition at the gas-shell interface, we thus assume that our equation for the gas temperature extrapolated to $r=a$ must equal the shell temperature at $r=a$ plus the temperature jump, or

$$\tau_p j_0(k_p a)+\tau_t j_0(k_t a)=\tau_{sh}+\Delta\tau. \tag{2.25}$$

The remaining thermal boundary condition at the gas-shell interface is continuity of heat flow. The thermal current in the shell can be expressed in terms of a thermal wave in the shell. Let λ_{sh}, δ_{sh}, and $k_{t,\,sh}=(1-i)/\delta_{sh}$ be the thermal conductivity, thermal penetration length, and propagation parameter for thermal waves in the shell, respectively. Radial thermal waves in the shell should be described by a Hankel function; however, owing to the small value of δ_{sh} an exponential form $\tau_{sh}\exp[k_{t,\,sh}(r-a)]$ is an excellent approximation. Continuity of heat flow at the interface can be expressed as

$$-\lambda_g[k_p\tau_p j_0'(k_p a)+k_t\tau_t j_0'(k_t a)]=\lambda_{sh}k_{t,\,sh}\tau_{sh}. \tag{2.26}$$

Equations (2.25) and (2.26) give the ratio of the amplitudes τ_p and τ_t:

$$\tau_p j_0(k_p a)\left[1+\left(k_p l_a+\frac{\lambda_g k_p}{\lambda_{sh}k_{t,\,sh}}\right)\frac{j_0'(k_p a)}{j_0(k_p a)}\right]$$

$$-\tau_t j_0(k_t a)\left[1+\left(k_t l_a+\frac{\lambda_g\delta_{sh}}{\lambda_{sh}\delta_t}\right)\frac{j_0'(k_t a)}{j_0(k_t a)}\right]. \tag{2.27}$$

The final step in obtaining an equation for the eigenfrequencies is to substitute eqs (2.16) and (2.17) into eq (2.25), and to use eq (2.27) to eliminate the ratio of the temperature amplitudes. As in reference [9], it is possible to do this without introducing any approximations, which leads to an equation which can be solved numerically to determine the eigenfrequencies. For the range of parameters used in this work, however, it is possible to identify certain small terms and to obtain a sufficiently accurate approximate equation for the eigenfrequencies. The result is

$$-i(\omega a/c)\beta_{sh}=$$

$$\frac{k_p a j_0'(k_p a)}{j_0(k_p a)}+\frac{\omega^2 a^2}{c^2}\left[-(1-i)\frac{\gamma-1}{2}\frac{\delta_t}{a}+(\gamma-1)\frac{l_a}{a}\right.$$

$$\left.-(1+i)\frac{\gamma-1}{2}\frac{\delta_{sh}}{a}\frac{\lambda_g}{\lambda_{sh}}\right], \tag{2.28}$$

where products of various "small" quantities have been omitted. Numerical values of the "small" quantities are given below for argon at 273.16 K in a stainless steel resonator. The quantities are all dimensionless; frequency and pressure dependence is indicated in terms of the dimensionless frequency $\tilde{f}$ and the dimensionless pressure $\tilde{p}$.

$$k_p l_a=6.0\times10^{-6}\tilde{f}$$

$$(\lambda_g/\lambda_{sh})(k_p\delta_{sh})=1.4\times10^{-6}(\tilde{f}/\tilde{p})^{1/2}$$

$$k_t l_a=2.5\times10^{-3}(1-i)(\tilde{p}\tilde{f})^{1/2}$$

$$(\lambda_g/\lambda_{sh})(\delta_{sh}/\delta_t)=5.6\times10^{-4}(\tilde{p})^{1/2}$$

$$\delta_t/a = 5.4\times 10^{-4}(\tilde{f}\tilde{p})^{-1/2}$$

$$(\omega\delta_t/c)^2 = 5.8\times 10^{-6}(\tilde{f}/\tilde{p}) \qquad (2.29)$$

The expression in eq (2.28) involving the spherical Bessel functions is also "small." In obtaining eq (2.28) the products $(\delta_t/a)(k_t a)$ and $(\delta_t/a)[(\lambda_g/\lambda_{sh})(k_p\delta_{sh})]$ were retained; all other products were omitted.

The next step is to obtain an approximate solution to eq (2.28). Equation (2.13) gives a relation between k_p and ω correct to order $(\omega\delta/c)^4$:

$$k_p a = (2\pi a/c)(f_{0n} + \Delta f - ig_{bulk}) = z_{0n} + \Delta k a, \quad (2.30)$$

where $f_{0n} = cz_{0n}/(2\pi a)$, and

$$g_{bulk} = \frac{\pi^2 f^3}{c^2}\left[(\gamma-1)\delta_t^2 + \frac{4}{3}\delta_v^2 + \frac{\eta_b}{\rho\omega}\right] \qquad (2.31)$$

can be identified as the contribution to the imaginary part of the resonance frequency which is proportional to the bulk attenuation of sound. In eq (2.31) and similar equations which give the value of small terms, f represents either the mean source frequency in steady-state measurements or the real part of the mode frequency in free decay. As noted above, the bulk viscosity term η_b is negligible for monatomic gases. By expanding the spherical Bessel functions in eq (2.28) and using the notation of eq (2.30), approximate solutions for the complex eigenfrequencies $F_{0n} = f_{0n}^0 + \Delta f_{0n} + ig_{0n}$ can be found:

$$\frac{\Delta f_{0n} + ig_{0n}}{f_{0n}} = \frac{g_{bulk}}{f} + \frac{\Delta f_{sh}}{f} + \frac{\Delta f_t + g_t}{f}$$

$$= i(\pi f/c)^2[(\gamma-1)\delta_t^2 + (4/3)\delta_v^2] + \frac{i\beta_{sh}}{z_{0n}}$$

$$-(1-i)\frac{\gamma-1}{2}\frac{\delta_t}{a} + (\gamma-1)\frac{l_a}{a}$$

$$+(1+i)\frac{\gamma-1}{2}\frac{\delta_{sh}}{a}\frac{\lambda_g}{\lambda_{sh}}. \qquad (2.32)$$

The first term on the second line is the bulk loss term. The second is the shell correction. The sum of the remaining terms is the thermal boundary correction. The third term is the usual thermal boundary layer term. The fourth term accounts for the discontinuity of temperature at the boundary. The last term accounts for the penetration of the thermal wave into the shell.

The effect of lack of smoothness of the shell surface on the thermal boundary layer has been considered in some preliminary modeling calculations [24]. The surface was assumed to have a sinusoidal profile of amplitude $d \ll \delta_t$. (Such a finish might be left by machine tools.) The results seem to be sensitive mainly to the amplitude d and not to the horizontal spacing of the surface undulations, at least over the reasonable range of surface profiles which were investigated. The calculations suggest that the magnitude of Δf_t is increased by a fractional amount of order d/δ_t and that g_t is not affected.

2.4 Imperfect Spherical Geometry

Consider a resonator whose shape differs from a perfect sphere by an amount of order ϵ. Let the surface be described by

$$r(\theta,\phi) = a[1-\epsilon f(\theta,\phi)], \qquad (2.33)$$

where $f(\theta,\phi)$ is a smoothly-varying function of order unity. Greenspan [5,25] showed that constant-volume shape deformations do not affect the frequencies of radial modes to order ϵ. His argument was based on the Ehrenfest adiabatic principle and on an exact calculation for spheroidal deformations. Mehl [6,8] later applied boundary-shape perturbation theory to radial and non-radial modes. He confirmed that the effect of geometry on radial modes can be described to lowest-order in ϵ by

$$\Delta f_{geom}/f_{0n} = C_n\epsilon^2, \qquad (2.34)$$

and calculated values of the constants C_n for some sample shape functions $f(\theta,\phi)$. The results suggest that, for the values of ϵ obtainable with high-quality machining, the frequencies of the first seven radial modes will not be shifted by geometric effects by more than one part in 10^6. The internal consistency of experimental values of the speed of sound determined with different modes is an experimental check on this effect.

In summary, boundary shape perturbation theory predicts that the frequencies of the radial modes of a set of resonators with a common volume V are all the same to order ϵ. The results of an experiment done in a resonator with volume V will be equivalent to results obtained in an experiment with a perfect sphere of radius a, provided that

$$a = [3V/(4\pi)]^{1/3}. \qquad (2.35)$$

The volume, and hence the mean radius, of our resonator was determined by filling it with a measured quantity of mercury.

2.5 Transducers

The mechanical boundary impedance differs from the value for a uniform shell on the surface of the source and detector transducers. The two transducers have nominal resonance frequencies of 40 kHz. All acoustic measurements were taken at sufficiently low frequencies that the motion of the transducer membranes was limited by stiffness. Let the transducers have area A_{tr} and compliance per unit area χ. The acoustic admittance of the transducers is thus

$$\beta_{tr}=i\omega\rho c\chi \tag{2.36}$$

at low frequencies. The additional frequency perturbation due to the transducers can be calculated using boundary perturbation theory [9,26]. The result is

$$\frac{\Delta f_{tr}}{f_{0n}}=\frac{i\beta_{tr}}{z_{0n}}\frac{2A_{tr}}{4\pi a^2}=-\frac{\rho c^2\chi A_{tr}}{2\pi a^3}. \tag{2.37}$$

We used transducers with a nominal value of χ (specified by the manufacturer) of 1.5×10^{-10} m/Pa. The corresponding fractional shift is $-0.16\times10^{-6}\tilde{p}$.

2.6 Openings in Resonator Wall

Owing to imperfect fit, there are small annular slits surrounding each microphone adapter. The slits have widths d_{slit} on the order of 10 μm, and lengths equal to the circumference of the adapters $2\pi a_{tr}\approx2.98$ cm. According to boundary perturbation theory, if the slits have an acoustic admittance β_{slit}, the frequency perturbations are

$$\frac{\Delta f_{slit}+ig_{slit}}{f_{0n}}=\frac{i\beta_{slit}}{z_{0n}}\frac{4\pi a_{tr}d_{slit}}{4\pi a^2}\approx1.3\times10^{-6}\frac{i\beta_{slit}}{\tilde{f}}, \tag{2.38}$$

where the numerical value applies to a 10 μm slit width. Trusler [27] has calculated the input admittance of a slit bounded by semi-infinite parallel flat surfaces. For a slit of depth D, rigidly terminated at the end, the result is

$$\beta_{slit}=\frac{(1+i)\sqrt{3\gamma}}{6\delta_v/d_{slit}}\tanh[(1+i)(\delta_v/d_{slit})kD\sqrt{3\gamma}]. \tag{2.39}$$

With a depth of 8.7 mm, typical numerical values for the real and imaginary parts of this expression range from 0.05 to 1.

2.7 Steady State Response

The steady state response of the resonator has been calculated using a Green's function technique. A source region S' on the inner surface of the shell is assumed to have a radial velocity u_s relative to the rest of the shell. The steady-state acoustic pressure at any point r' in the resonator is

$$p'(r')=\sum_N\frac{i\omega\rho c^2\Psi_N(r')}{V\Lambda_N(\omega^2-F_N^2)}\int_{S'}\Psi_N(r)u_s(r)\mathrm{d}S, \tag{2.40}$$

where

$$\Phi_N(r)\approx j_l(k_{ln}r)Y_{lm}(\theta,\phi) \tag{2.41}$$

is a general eigenfunction, F_N is the corresponding eigenfrequency, Λ_N is the average value of Φ_N^2 over the resonator volume, and N stands for the triplet (l, n, m). The detector is typically a pressure transducer whose complex output voltage $u+iv$ is proportional to $p'(r')$, and is hence proportional to the summation in eq (2.40). In normal experimental practice, only one or a small number of modes whose eigenfrequencies lie within a small range are excited. The contribution of the excited modes can be described in detail by including one or a small number of terms in the summation in eq (2.40). The remaining terms of the summation can be approximated using a Taylor series in frequency. The detector output can then be written

$$u+iv=\sum_N\frac{ifA_N}{(f^2-F_N^2)}+B+C(f-f_0), \tag{2.42}$$

where A_N, B, and C are complex constants, and the sum is now over only one mode or over a small number of modes of interest.

2.8 A Working Equation for Determination of R

A "working equation" is useful for analysis of the various limits on determination of the gas constant R from measurements of the speed of sound. The speed of sound can be expressed as a virial series in the pressure

$$c^2=A_0+A_1P+A_2P^2+A_3P^3, \tag{2.43}$$

where we have truncated the series above the last

marginally significant term. The first term is

$$A_0=\gamma_0 RT/M, \tag{2.44}$$

where γ_0 is the ratio of the specific heat capacities in the ideal-gas limit. For monatomic gases it has the exact value 5/3 at temperatures where electronic excitations are not important. The other coefficients are temperature dependent; they can be related to the coefficients of a volumetric virial series and the temperature derivatives of those coefficients. In this work A_1 and A_2 will be determined in the experiment; a value of A_3 determined experimentally elsewhere will be used [28]. With approximate values to show the magnitudes of the various terms, eq (2.43) is

$$c^2=A_0[1+2.37\times10^{-4}\tilde{p}+5.6\times10^{-6}\tilde{p}^2 +1.5\times10^{-8}\tilde{p}^3]. \tag{2.45}$$

Experimental determinations of the resonance frequencies can be related to the speed of sound through

$$f_{0n}=\frac{cz_{0n}}{2\pi a}+\Delta f_{\rm sh}+\Delta f_{\rm t}, \tag{2.46}$$

where only the major corrections due to shell motion and the thermal boundary layer have been included. This can be rearranged to give experimental values of c^2:

$$\begin{aligned}c^2_{\rm exp}&=\left(\frac{2\pi}{z_{0n}}\right)^2\left(\frac{3V}{4\pi}\right)^{2/3}f^2_{0n,\,\rm exp}\left[1-\frac{2\Delta f_{\rm sh}}{f_{0n}}-\frac{2\Delta f_{\rm t}}{f_{0n}}\right]\\ &=\left(\frac{2\pi}{z_{0n}}\right)^2\left(\frac{3V}{4\pi}\right)^{2/3}f^2_{0n,\,\rm exp}\Big[1+3.4\times10^{-6}\tilde{p}\\ &\quad+3.4\times10^{-4}(\tilde{f}\tilde{p})^{-1/2}-1.8\times10^{-6}\tilde{p}^{-1}\\ &\quad+2.0\times10^{-7}(\tilde{f})^{-1/2}\Big].\end{aligned} \tag{2.47}$$

For the numerical expressions in eq (2.47), the low frequency form for the effect of the shell was used; a more accurate expression including the resonance denominator was used in the data analysis.

The effects of the various terms on a determination of R can be obtained by combining eqs (2.45) and (2.47):

$$\begin{aligned}R=\left(\frac{M}{\gamma_0 T}\right)\left(\frac{2\pi}{z_{0n}}\right)^2\left(\frac{3V}{4\pi}\right)^{2/3}f^2_{0n,\,\rm exp}\\ \times\Big[1-2.38\times10^{-4}\tilde{p}-5.6\times10^{-6}\tilde{p}^2-1.5\times10^{-8}\tilde{p}^3\\ +3.4\times10^{-6}\tilde{p}+3.4\times10^{-4}(\tilde{f}\tilde{p})^{-1/2}\\ -1.8\times10^{-6}\tilde{p}^{-1}+2.0\times10^{-7}(\tilde{f})^{-1/2}\Big].\end{aligned} \tag{2.48}$$

2.9 Discussion of Working Equation for R

Equation (2.48) demonstrates that, to first order, the present redetermination of R depends upon the accurate measurement of four quantities: the molar mass of the monatomic gas used, the thermodynamic temperature, the volume of the resonator, and a set of resonance frequencies. Upon inspection of the higher order terms in eq (2.48), it becomes evident that the redetermination of R is best accomplished in a limited range of pressures on the order of $\tilde{p}=1$.

If the pressure were much lower than $\tilde{p}=1$, the redetermination of R would depend strongly on terms which vary as $(\tilde{f}\tilde{p})^{-1/2}$ and as $(\tilde{p})^{-1}$. These terms are proportional to the thermal conductivity of the gas and the accommodation length, respectively. With state-of-the-art techniques, the thermal conductivity can be measured with an accuracy on the order of tenths of a percent. The accommodation length is a property of both the gas and the particular surface of our resonator: thus it must be determined by fitting the pressure dependence of the resonance frequencies. The accuracy of this procedure is limited because the signal-to-noise ratio of the measurements of $f^2_{0n,\,\rm exp}$ varies as $(\tilde{p})^{-2}$ at pressures below $\tilde{p}\approx1$. Furthermore, as the pressure is reduced, the problem of contamination of the gas under study becomes increasingly difficult.

If the pressure were much higher than $\tilde{p}=1$, the redetermination of R would depend strongly on the terms in eq (2.48) which vary as $\tilde{p}$, $(\tilde{p})^2$, and $(\tilde{p})^3$. These terms depend upon the virial coefficients of argon and the elastic properties of the resonator. They cannot be predicted with the necessary accuracy; thus, these terms must also be determined by fitting the pressure dependence of the resonance frequencies. As the pressure is increased, the correlations between these terms in the multiparameter fit limit the accuracy with which each term can be determined.

As discussed below, we have chosen to use other measurements to obtain the coefficients of $(\tilde{p}\tilde{f})^{-1/2}$ and the very small coefficients of $(\tilde{p})^3$ and $(\tilde{f})^{-1/2}$. We have fitted our own data to obtain R and the coefficients of $(\tilde{p})^{-1}$, $\tilde{p}$, and $(\tilde{p})^2$. We have also

chosen to carry out our measurements very near T_t. Therefore, we have avoided problems associated with the imperfect knowledge of the relation between the thermodynamic temperature scale and the practical temperature scale.

3. Fabrication and Characterization of Resonator

In this section, we describe the manufacture and characterization of the spherical acoustic resonator. The description commences with the design, fabrication, and final finishing of two hemispherical shells. It includes a table of their dimensions. We continue by discussing the assembly of the hemispheres into a hollow spherical shell and we give a description of the fixtures and the ports used to install electroacoustic transducers into the shell. This section concludes with a description of the acoustic measurements which characterize the completed resonator. These measurements determine the frequency of the breathing mode of the completed resonator.

3.1 Design and Fabrication

The spherical resonator was assembled from two stainless-steel hemispheres. Figure 2 shows the hemispheres and gives the dimensions specified in our design. In earlier work with spherical resonators, the shells were fabricated from aluminium or brass. These materials are incompatible with mercury. The resonator of the present study was fabricated from type 316L stainless-steel bar stock. This alloy has excellent corrosion resistance and good machining properties.

To facilitate precise alignment of the two hemispheres, the equatorial sections of the outer surfaces were made accurately cylindrical and concentric with the spherical surfaces. Cylindrical bosses were machined at the pole of each hemisphere. These were used to hold the pieces during machining of the internal surfaces and were subsequently modified to accept mounting blocks for the two platinum resistance thermometers. The boss on the upper ("northern") hemisphere was also machined to accommodate the gas-inlet line and valve mechanism. Previous experience had shown that polishing the interior surfaces of the hemispheres rounded their equatorial edges. This created an equatorial groove with curved sides when the hemispheres were fastened together. To prevent this, each hemisphere was initially machined with a

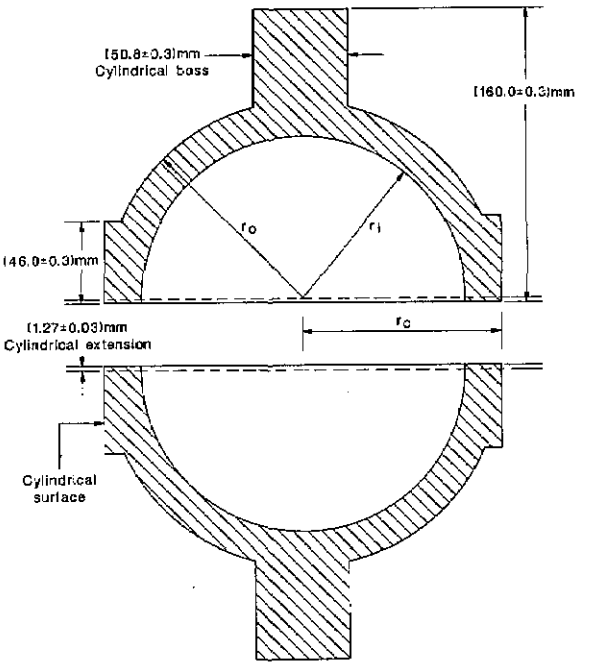

Figure 2. Cross-section of hemispheres.

cylindrical extension from the equatorial plane. The extension was removed after final polishing.

Two ports were machined in the northern hemisphere to accept adaptors housing the electroacoustic transducers used to excite and detect the sound field. In order to enhance the discrimination between the (3,1) non-radial mode and the (0,2) radial mode, these ports were placed 90° apart on the spherical surfaces. Their orientation at 45° with respect to the polar axis was chosen for convenience. We now describe the machining sequence required to turn the cylindrical blanks into the hemispheres as shown in figure 2, and the additional operations performed to obtain the finished resonator.

All turning operations were conducted on a numerically-controlled turret lathe. In this lathe, the turret is able to travel continuously and independently perpendicular and parallel to the turning axis. Position read-out resolution was 2.5 μm. The spindle speed was also varied under numerical control so that the surface speed of the work past the cutting tool was as constant as possible. The following operations were performed:

(1) Each cylindrical blank was held in a three-jaw chuck and, after rough machining, the boss and the spherical portion of the outer surface were turned in one pass to the final size.

(2) The piece was then reversed and held by the boss for the remainder of the machining.

(3) The rough machining of the internal surface took place via a series of steps at 0.75 mm increments. The rough diameter was smaller than the finish diameter by approximately 1.5 mm. At this stage, the outer cylindrical surface was turned to within 0.75 mm of final size.

(4) The hemispheres were then given stress-relieving heat treatment consisting of 40 hours at 400 °C in air, followed by a slow cool down over 24 hours. This operation was intended to promote dimensional stability by relieving stress originally present in the billet.

(5) The stepped inner surface then received the first cut in which the cutting tool followed, in one pass, the desired profile. This profile passed along the outer cylindrical surface, across the rim, and along the inner surface of the cylindrical extension; it then proceeded along a 90° circular arc to form a hemispherical chamber. After this pass, the inner surface was within 0.25 mm of final dimensions.

(6) The hemispheres were heat treated, similar to (4).

(7) Prior to final machining of the spherical surface, the tool piece was reground. Since the cutting tool traced out a quarter circle cutting arc, the point of contact between it and the work piece also moved by 90°. Consequently, the tool tip was required to have an accurate semi-circular cross-section. The Stellite tool was ground to a tip radius of 0.18 mm; the radius and shape were then checked using a shadow-graph projector.

(8) Each hemisphere was then chucked, trued, and given the final cut. In each case, the cutting tool followed precisely the same path, thereby ensuring nearly identical hemispheres.

3.2 Polishing

Visual inspection of the internal surfaces after initial machining showed that the finish was unsatisfactory. Turning marks were evident. Thus, the hemispheres were mounted in a lathe and hand polished to a near mirror finish using successively lighter grades of emery paper and cutting oil in the initial stages of polishing. The final finish was achieved using α- and γ-alumina paste (0.3 and 0.05 μm particle sizes). After these steps, almost all of the tooling marks that had initially been present were no longer visible.

3.3 Final Machining

After completion of the polishing and dimensional measurements, final machining was performed. This work consisted of the following five operations: (1) facing and drilling of the bosses in preparation for the attachment of stainless-steel blocks containing the platinum resistance thermometers, (2) fabrication of the gas-inlet-valve port in the boss of the "northern" hemisphere, (3) fabrication of transducer ports (also in the northern hemisphere), (4) drilling of 18 bolt holes vertically through the equatorial joint so that the hemispheres could be bolted together to form the finished resonator, and finally, (5) removal of the cylindrical extensions by turning and then lapping of the mating surfaces to a local flatness of 0.5 μm.

The isolation valve is shown in detail in figure 3. It consists of the bellows assembly and valve driver mechanism from a commercial 316 stainless-steel valve (Nupro bellows valve, type SS-6BG [29]) and is clamped to the boss by a retaining nut. A vacuum tight seal is effected by the compression of a stainless-steel O-ring. The valve stem and tip supplied with the valve were removed and replaced by a specially fabricated shaft. The shaft was made from 316 stainless-steel and was polished so that there was a snug sliding fit in the passage bored in the top of the boss, ensuring that the tip of the shaft would always enter the 3.2 mm diameter aperture in the sphere wall without catching or fouling. When closed, the sloping shoulder of the stem made metal-to-metal contact with a mating surface in the passage, thus ensuring reproducible positioning of the stem tip relative to the inner spherical surfce. At the same time, a "Viton" O-ring [29] was compressed on the sloping surface and isolated the sample gas. A number of axial slits were milled along the shaft to provide pathways for gas flow when evacuating the resonator (and the dead space within the bellows). The dimensions of these slits were such that when the valve was fully open the vacuum pumping speed of the resonator was largely determined by the conductance of the aperture in the spherical wall.

In addition to having accurate placement, the transducer holes through the spherical wall must be of known depth and diameter so that the transducer housings, and the stainless steel plugs that sealed the ports during the volume determination could be machined for tight fit. Accordingly, this operation was performed using a precision jig boring machine and a micrometer-adjustable variable radius boring bar. To maintain a sharp edge, free of burrs, at the intersection of the hole and the spherical surface, cutting was performed with the rotating tool moving radially outwards from the

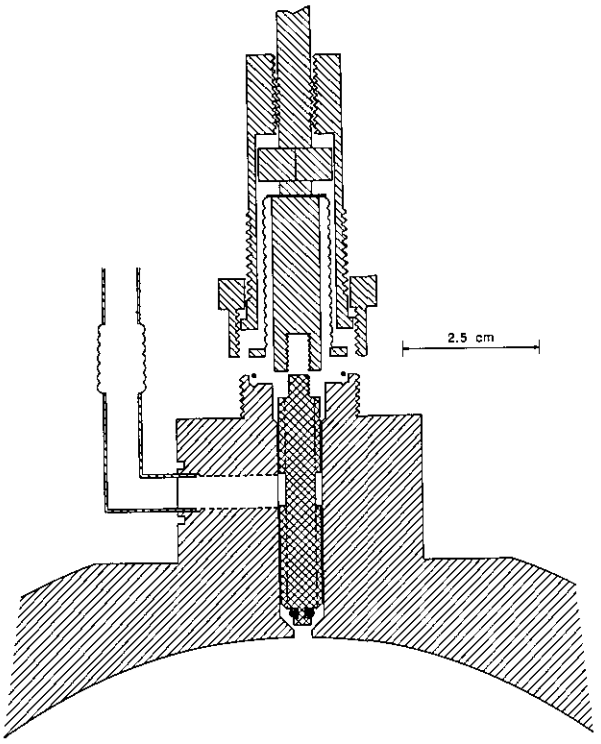

Figure 3. Cross-section of isolation valve.

resonator. The jig borer was also used to mill the features of the recess that located the transducer housing. These features therefore were highly concentric with the axis of the transducer port.

3.4 Dimensional Measurements

A Bendix [29] coordinate measuring machine (CMM) was frequently employed during machining to monitor the progress of metal removal and to determine the relationship between the cutting edge of the tool and the coordinate scales of the lathe. It was also used for the final dimensional measurements. The CMM was housed in a thermostatted room maintained at 22.07 °C. The machine had a resolution and repeatibility of 2.5 μm, and an accuracy of approximately twice that figure.

Each hemisphere was held vertically by the boss in a precision dividing-head chuck mounted on the CMM flat bed, so that coordinate measurements could be taken at different angular orientations of the hemispheres. Before commencing dimensional measurements, the hemispheres were brought into thermal equilibrium with the room. A measuring sequence consisted of: (1) determination of the coordinates of the (imaginary) plane bounding the open face of the cylindrical extension to the hemisphere from four approximately equally spaced points on the flat face of the extension, (2) co-ordinate measurements made at 12 equally spaced points around the outside of the cylindrical section, from which the least-squares-best-fit circle (center (x_c,y_c), radius r_c) was obtained, and (3) co-ordinate measurements made at 16 equally spaced points along the arc of a great circle. Three more such arcs were traced out at 45°, 90°, and 135° to the original arc; thus there were 64 coordinate points from which the best fit spherical surface was determined. The radius r_s, radial deviations δr_s, root mean square radial deviation $<\delta r_s^2>^{1/2}$, and coordinates (x_s,y_s,z_s) of the center of the best fit spherical surface were then determined. This gave directly the height h of the cylindrical section abutting the hemisphere. In addition, the differences δx and δy between the centers of the spherical and cylindrical surfaces gave a measure of concentricity.

The results of dimensional measurements performed both after the initial machining and after polishing (but prior to final machining and lapping) are summarized in table 2. Repeated measurements demonstrated that the *repeatability* of mean radius determinations was about an order of magnitude smaller than the resolution of the CMM. The external radii are particularly well matched (to within 5 μm) and the difference was unchanged over the period of about 3 months between the two sets of measurements reported in table 2. The internal radii match to 20 μm, or about 220 ppm in r_s. Such a difference leads to a very small, second-order, perturbation to the resonance frequencies of the radial modes used in this work. The perturbation can be calculated from table II of reference [6] and is −0.7 ppm for the (0,2) mode; it is less than 0.1 ppm for the (0,3) through (0,6) modes.

The volume of the spherical chamber that would have been formed from the two hemispheres assuming perfect removal of the cylindrical extensions is $(2945.8_1 \pm 0.5_4)$ cm^3 at 22.07 °C. This volume differs by (148±194) ppm from that obtained from weighing mercury as described in section 6. Unfortunately, we had no opportunity to monitor the removal of the cylindrical extensions using the coordinate measuring machine. Such an extension may have been the largest geometric imperfection in the assembled resonator; however, it could not have been very large without destroying the agreement of the volumes determined from dimensional measurements and from weighing.

Table 2. Key dimensions of the hemispheres

Blank	Outside radius, r_c, mm	Inside radius, r_s, mm	rms radial deviation $<\delta r_s^2>^{1/2}$, μm	Concentricity δx, μm	δy, μm	Cylindrical extension h, mm
			After final polish			
#1	107.958	88.918	10	8	5	0.570
#2	107.963	88.938	4	1	1	0.509
			Before final polish			
#1	107.949	88.922	5	8	−4	0.537
#2	107.955	88.938	5	2	−5	0.497

An analysis of the deviations of the 64 data points from the best-fit spherical surface reveals that the deviations from sphericity are not random. There are two reasons why the deviations are likely to vary with latitude. Firstly, if the tool tip is not ground with a precisely constant radius of curvature, then departures from sphericity will be produced. Secondly, the surface speed past the polishing cloth depends upon the latitude; thus it is difficult to hand polish a spherical surface in a uniform way.

On the assumption that the radial deviations are a function of angle alone, the 16 points on each measuring arc may be reduced to 8 mean measurements at evenly spaced latitudes between 2° and 84°. As there were 4 measuring arcs there were 8 measurements of the radial deviation at each latitude. The mean and a typical standard deviation of the 8 points at each latitude are displayed in figure 4 for both finished hemispheres.

The dimensions of the transducer ports were also measured with a calibrated coordinate measuring machine. The diameter was measured at several locations along the axis of the port. In all cases we obtained the same diameter, confirming that the transducer ports were not tapered and were circular to within the 2.5 μm resolution and repeatibility of the CMM.

The length of the transducer hole was measured by standing the hemisphere on a gage block placed within the inner recess prepared for the transducer housing. After locating the center coordinates of the port, the vertical coordinate of the gage block was measured there, and the coordinates of a number of contact points on the spherical surface were also obtained at a fixed height above the gage block. Knowing the radius r_s of the sphere and the radius of the port it is then a matter of simple geometry to obtain the length of the wall of the transducer port.

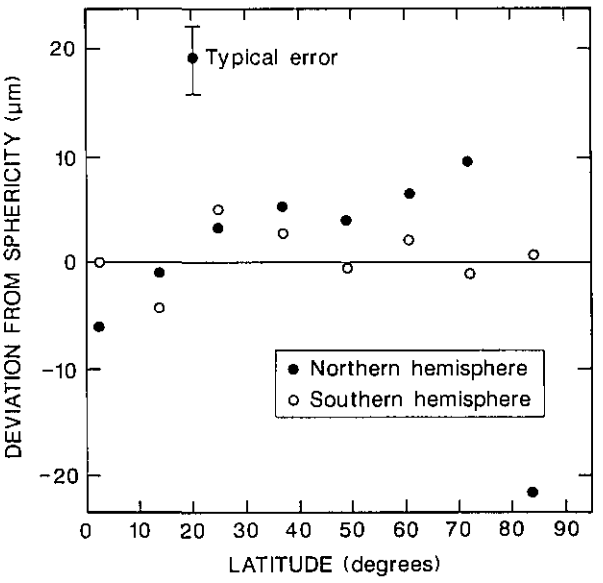

Figure 4. Deviations from sphericity of hemispheres after polishing.

The dimensional measurements conducted on the transducer ports gave the following results:

	Diameter, mm	Length, mm
Transducer port 1	9.545±0.005	9.624±0.005
Transducer port 2	9.520±0.005	9.733±0.005

3.5 Assembly of the Resonator

In order to use the resonator for accurate measurements of the speed of sound, its volume must be stable and nearly spherical. It is particularly important to avoid a gap at the equatorial joint between the hemispheres. (Such a gap would perturb the acoustic resonance frequencies in a hard-to-

predict fashion and could permit irreproducible intrusion of the mercury used for the volume measurement.) A prototype resonator had been assembled by electron-beam welding; however, it did not have a stable volume. The alternative that was ultimately used, was to "solder" the two hemispheres together with an extremely thin layer of "Apiezon-W" vacuum wax [29]. The resulting resonator had a volume which did not change by more than 0.8 ppm during the six months between two volume measurements. (0.8 ppm was the range of the volume difference measurement.) The resonator did not have a void at the joint. We shall now describe the procedure for "soldering" the hemispheres together.

The mating surfaces had been lapped flat in the optical shop to a nominal tolerance of 0.5 μm. The hemispheres had been ultrasonically cleaned and vapor degreased by the shop and finally cleaned by us with distilled trichloroethane. A solution of the wax (3 mg/cm^3) was prepared using freshly distilled 1,1,1-trichloroethane. It was applied to one of the hemispheres using a homemade atomizer with helium as the propellant. The spraying was carried out while the hemisphere was in a fume hood and was maintained at 110 °C with a heating mantle. Under these conditions, the solvent and volatile impurities in the wax evaporated quickly, and the wax completely wetted the steel surface. Thus, the wax formed a uniform layer with no tendency to coagulate. The layer did not appear to contain embedded dust when it was examined after cooling. If there were no overspray, the 20 cm^3 of solution would have deposited a wax layer 5 μm thick. Examination of the masks used to protect the inner surface of the hemisphere and the mantle during spraying suggests that 2/3 or more of the wax remained on the joint.

The cooled, waxed hemisphere was set on a table and the other hemisphere was lowered on it with a hoist. During this procedure, the joint was cushioned and lubricated with a layer of freshly distilled isopropyl alcohol. A coarse alignment of the hemispheres was maintained with four PTFE rods which passed through the bolt holes in both hemispheres. The final alignment was achieved manually with the aid of three aluminum blocks used at 120° intervals on the cylindrical portions of the hemispheres around the equator. The 18 stainless-steel bolts (1/4"-24) were drawn up finger tight, torqued to 1.7 N·m (15 in·lb), and then torqued to 14 N·m (10 ft·lb). The assembled resonator was heated in an oven to 60 °C and the bolts were re-torqued to 14 N·m; it was heated to 100 °C and re-torqued to 14 N·m; and, finally it was maintained at 120 °C for 15 h. After these steps, tiny beads of wax were visible at the seam on both the interior and the exterior surfaces of the resonator. (The interior was inspected with a borescope.) This indicates that the wax did flow as required and that there was no crack where the joint meets the interior surface of the resonator. We believe that the small burr that remained after lapping prevented the formation of a continuous bead at the joint. It is not surprising that we never found evidence of leakage at the joint with a helium leak detector. The tiny beads at the joint within the resonator were not removed.

3.6 Transducers and Transducer Housings

Two electroacoustic transducers were used to measure the resonance frequencies. Both transducers were mounted flush with the interior wall of the resonator. As sketched in figure 5, they were both located at 45° from the north pole on the same great circle through the pole. One transducer drove the sound field within the resonator and the other one detected the amplitude and phase of the pressure at a point 90° away from the driver. (This 90° orientation was chosen to minimize the detector's response to the (3,1) non-radial mode when measuring the resonance frequency of the nearby (0,2) radially symmetric mode.) Both transducers were commercially manufactured microphone cartridges (Bruel & Kjaer Type 4135, [29]). These microphones were constructed from materials which are compatible with clean gases (silicone treated quartz, high nickel alloys, and gold plating). The manufacturer provided voluminous data describing their mechanical and electrical characteristics. The moving element of each microphone was a flat, stretched, nickel diaphragm which was nearly flush with the front of the cartridge and served as one electrode of a capacitor. The other electrode was a monel backplate located 20 μm behind the diaphragm. The generator was excited with 60 V (RMS), at half the desired acoustic frequency. The motion of the detector's diaphragm was measured with a commercially manufactured bias supply and preamplifier (Bruel & Kjaer Model 2660, [29]), whose output was connected to a lock-in amplifier. Under typical conditions [300 kPa, (0,4) mode] the acoustic pressure was 0.0023 Pa.

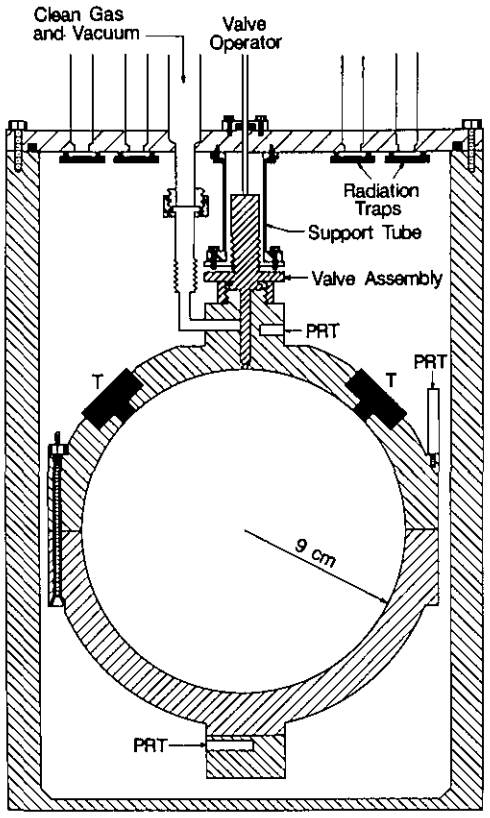

Figure 5. Cross-section of resonator and pressure vessel. The transducer assemblies are indicated by "T," and the locations of the capsule thermometers are indicated by "PRT."

Transducer housing assemblies were used to support the microphone cartridges in precisely defined positions within the transducer ports of the resonator. The transducer housing assemblies also acted as hermetic seals and electrical feedthroughs. The components of a transducer housing assembly are shown in figure 6.

The manufacturer of the microphone cartridges supplied them with protective grids covering the diaphragms. These grids were unscrewed and replaced with threaded bands which were the key components for positioning the cartridges within the transducer housings. Each threaded band was pressed against the inside front surface of its housing by a tube threaded along part of its length. (A slot in the tube was used to screw the tube into the housing, thus, pressing the band against its housing's surface.) The outside and inside diameters of the front of the housings were machined to tight tolerances (± 6 μm) to minimize the volumes of the annular gaps exposed to the acoustic field within the resonator.

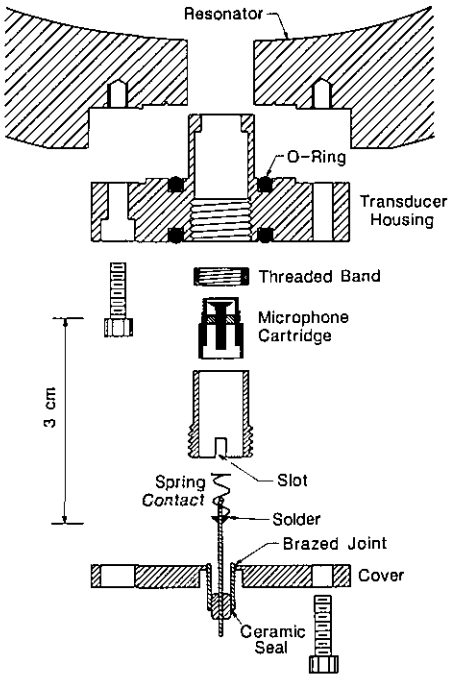

Figure 6. Exploded section of transducer housing assembly and electrical feedthroughs.

"Viton" [29] O-rings were used to seal the transducer housings to the resonator. Thus, the positions of the microphones' diaphragms with respect to the interior surface of the resonator were determined by reproducible metal-to-metal contacts. The backs of the transducer housings were sealed to covers with "Viton" [29] O-rings. Commercially manufactured electrical feedthroughs were brazed to the covers. For the detector transducer, a shield (not shown) surrounded the outside of the feedthrough. Triaxial cable led from this shield and the feedthrough through the pressure vessel, up the interior of a tube through the water bath, through a triaxial feedthrough, and, with additional triaxial cable, to the preamplifier. The guard of this cable was driven by the preamplifier to compensate for loading of the detector by the large capacitance of the cable. For the driven transducer, coaxial cable led from the cover to signal source.

The volume in each transducer housing behind the microphone cartridge is approximately 0.5 cm^3. This volume is connected to the interior of the resonator by a small pressure-equalization port within the cartridge and by the small gaps between the machined components of the transducer housing assembly. Such a volume is slow to pump out. Thus, extensive flushing procedures were used

when changing the gas sample in the resonator, as described in section 7. Furthermore, to avoid stressing the diaphragms, the pressure within the resonator was never changed faster than 1 kPa/s and potential differences were never applied to the transducers while the pressure was being changed.

After their initial installation in the resonator, intermittent electrical arcing was detected in both transducers. The occurrence of arcing increased, eventually reaching several incidents within a minute. After a few hours of use, the detector transducer failed. Examination showed that its diaphragm was torn. The diaphragms of both transducers had numerous pinholes, presumably as a result of the arcing. Both damaged transducers were replaced. In subsequent use, a few isolated incidents of arcing have occurred. The transducers' sensitivity remained unchanged after several hundred hours of operation. We have no certain explanation of the cause of the arcing, nor are we aware of any changes in procedure which have diminished its frequency.

3.7 Geometry of the Assembled Resonator

Moldover, Mehl, and Greenspan [9] have argued that some information concerning the geometry of the assembled resonator can be obtained by measuring the resonance frequencies of the nearly degenerate, non-radial modes. We made an effort to exploit this possibility; however, we were not able to obtain a satisfactory interpretation of the results.

We attempted to measure the three components of the (1,3) and (1,8) modes with argon in the resonator at 0.1 MPa. For both modes, only two components were found. For both modes, the two components had nearly equal amplitudes and scaled half-widths g_N/f_N within 3 ppm of the theoretical values. The components of the (1,3) and (1,8) modes were separated by 215 ppm and 214 ppm of their average frequencies, respectively. For both modes, the phase difference between the two components was within 0.5° of 180°. For the (1,3) mode, the phase of the lower frequency component was 8° from that interpolated between the adjacent radially symmetric (0,3) and (0,4) modes. For the (1,8) mode, the phase of the lower frequency component was 17° from that interpolated between the adjacent, radially symmetric (0,8) and (0,9) modes. Following reference [9], we attempted to interpret these observations in terms of smooth, axisymmetric imperfections in the resonator's geometry. (The calculations use unpublished notes and eqs (67-69) of reference [9]. Note that eq (69) of this reference should be corrected to read $\lambda_0 = -1$.)

The phase relations suggest that the lower frequency component of each mode results from gas motion with a symmetry axis which is nearly coincident with the line running from the north pole to the south pole of the resonator. The higher frequency component resulted from gas motion with a symmetry axis which is in the plane of the equator and which is also in the plane through the transducers and the poles. If this interpretation were correct, one would expect the unobserved third components of the (1,3) and (1,8) modes to be much weaker than the two observed components because the gas motion is primarily along the axis in the equatorial plane which is perpendicular to the plane of the transducers. The frequency of the third component would be nearly coincident with the higher of the two observed frequencies and the phase of the third component would be nearly coincident with the phase of the higher frequency component. The fit to the (1,3) and the (1,8) data is not improved by the addition of such a third component.

If the geometric interpretation of the splitting were correct, and if the resonator were modeled as either a prolate spheroid or as two hemispheres separated by a short cylindrical section, the effective polar diameter of the resonator would have to be about 530 ppm greater than the effective equatorial diameter.

A 530 ppm difference in diameters is not consistent with the dimensional measurements made on the hemispheres prior to their assembly (see sec. 3.4). In particular, with the assumption that there is no cylindrical extension, the volume of the resonator determined from dimensional measurements is (150±190) ppm smaller than the volume determined from the very accurate weighing and expansion measurements described in section 6. A cylindrical extension of 530 ppm would increase the volume determined from the dimensional measurements by 790 ppm leading to an inconsistency. (As discussed above, the thickness of the equatorial joint is less than 20 ppm of the diameter.) Furthermore, a cylindrical extension (or comparable ellipsoidal deformation) would cause a shift in the frequencies of the $(0,n)$ modes in the second order of perturbation theory, that would range from 0.16 to 2.48 ppm for the (0,2) through the (0,6) modes. Such shifts would be manifest as a dispersion of 4.6 ppm in the values of c^2 determined from these modes. No dispersion was observed. (See sec. 9 and especially fig. 17.)

3.8 Breathing Motion of the Shell

The effects of shell motion on the gas resonances have been discussed in reference [9] and in greater detail by Mehl [7]. In these publications, the shell motion was modeled as an isotropic "breathing" motion excited by radially symmetric oscillations of the gas within it. This model can be combined with the known dimensions of the resonator and the properties of the alloy it was fabricated from (see table 3) to predict that the frequencies of the gas resonances are perturbed by:

$$\frac{\Delta f_{\text{shell}}}{f} = \frac{-\gamma_0 p \chi_{s,i}/3}{1-(f/f_{\text{breathing}})^2}. \tag{3.1}$$

Here, γ_0 is 5/3, a is the inner radius of the shell, $\chi_{s,i} \equiv (3/a)\cdot(da/dp)_i$ is the shell's compliance to internally applied pressure which we have measured in connection with the volume determination (sec. 6.8.3), and the $f_{\text{breathing}}$ is calculated to be 13.58 kHz from the data in table 3.

Table 3. Properties of shell

Density	7.96 g/cm^3
Internal radius	88.9 mm
External radius	108 mm
Young's Modulus	197 GPa
Poisson ratio	0.297

When helium was in the resonator at T_t, the (0,3) acoustic resonance varied from 13.450 kHz to 13.516 kHz as the pressure was increased from 75 kPa to 1003 kPa; thus this gas resonance was strongly perturbed by the shell's motion. Upon comparing the (0,3) resonance with the others, it was obvious that the dominant shell response occurred at a frequency well below 13.450 kHz. We were led to study the shell motion further with simple auxiliary experiments.

In one experiment, a piezoelectric transducer was clamped to the boss on the bottom of the shell and was used to shake the shell. A phonograph needle was placed in contact with the shell in several different positions to detect the shell's motion. No resonance was observed at 13.58 kHz; however, at least three resonances occurred in the range 13.1–13.3 kHz. When the positions of the transducers were changed, the frequencies of the peak amplitudes varied slightly while the relative amplitudes varied dramatically. When the excitation was at the south pole and the detector was at the north pole, the most prominent component of this multiplet was at 13.220 kHz at 22.5 °C and at 13.190 kHz when the shell was warmed to 29.5 °C. At both temperatures, the half-width of this component was 18 Hz. While these measurements were conducted, the shell contained argon at a pressure near 0.1 MPa and the exterior of the shell was exposed to the ambient air.

A second experiment was conducted to determine which, if any, of these shell resonances couple to the radially symmetric oscillations of the gas within the shell. The frequencies and half-widths of the (0,2) and (0,8) modes were measured with argon in the resonator while the speed of sound of the argon was continuously changed by scanning the temperature of the shell from 0–35 °C. To interpret the results, it was assumed that the effect of the shell motion on the (0,2) mode is exactly given by eq (3.1). The measured perturbation of the real and imaginary parts of the (0,8) frequency is shown in figure 7. The smooth curve drawn through the data is the sum of two terms in the form of eq (3.1) with "$f_{\text{breathing}}$" given by $13245+30i$ Hz and $13080+50i$ Hz and with amplitudes 0.3 and 0.08 times as large as that in eq (3.1). It is clear that at least two of the shell resonances which were directly observed do indeed couple to radially symmetric gas motion. In order to account for the measured static compliance of the shell, one must assume that there are other resonances which also couple to radial gas motions. They might be nearly degenerate and interfere with the observed resonances, or they might be too broad to be detected by these simple experiments.

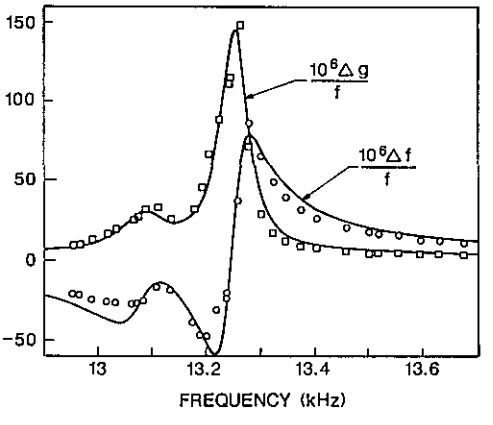

Figure 7. Perturbations to the frequency and half-width of (0,8) mode as a function of frequency, with argon in the resonator at 100 kPa. The frequency was swept by changing the temperature of the resonator, which changes the speed of sound.

The shell's motion is more complex than an isotropic breathing. In lieu of a more accurate model, we have not based the measurement of R on data close to the predicted breathing mode. (The argon data for the (0,2) through (0,6) modes span the range 2.5–10.0 kHz.) We have used eq (3.1) with $f_{\text{breathing}}=13.58$ kHz to approximate the effects of shell motion. If this approximation were seriously in error, the values of c^2 determined with various modes would differ significantly from one another. They do not. If $f_{\text{breathing}}$ in eq (3.1) were changed by 400 Hz, R would change by less than 1 part in 10^8. If the compliance $\chi_{s,i}$ were changed by its estimated error, 6%, R would be changed by less than 1 part in 10^8. Because the frequency shifts produced by the shell's motion are a linear function of pressure, the errors in $\chi_{s,i}$ have a direct effect on A_1, the first pressure coefficient of the square of the speed of sound. A 6% increase in the magnitude of $\chi_{s,i}$ leads to a 0.09% increase in A_1.

4. Measuring Resonance Frequencies

We shall now describe the procedures we used for measuring the frequencies and the half-widths of the acoustic resonances. Upon assessing the accuracy of the results we shall argue that the data for the (0,7) mode should be ignored when either helium or argon is used in our resonator because it overlaps the (13,2) mode. As discussed above, the (0,3) mode should be ignored when the resonator is filled with helium because this mode is nearly coincident with the breathing resonance of the empty shell.

4.1 Procedures for Frequency Measurements

The strategy used to measure the resonance frequencies f_N and the half-widths g_N is the same one documented in earlier work [9,11]. Preliminary measurements were used to estimate f_N and g_N. Then the drive transducer was stepped through 11 synthesized, discrete frequencies starting at f_N-g_N and increasing in increments of $g_N/5$ until f_N+g_N was reached. At each frequency, the in-phase voltage u and the quadrature voltage v produced by the detector transducer were measured with a tracking lock-in amplifier, scanner, and digital voltmeter, all operating under control of a microcomputer. Then the sign of the frequency increment was reversed and the voltages were measured again as the frequency was reduced in steps back to its original value. A function of the theoretically predicted form

$$u+iv=\frac{ifA}{(f^2-F_N^2)}+B+C(f-f_N) \tag{4.1}$$

was fit to the 11 frequencies and 44 voltages. Here, A, B, and C are complex constants, and $F_N=f_N+ig_N$ is the complex resonance frequency of the mode under study. The parameters B and C account for possible crosstalk and for the effects of the "tails" of the modes other than the one under study. For all the argon data at pressures above 100 kPa, the inclusion of the parameter C in eq (4.1) is justified at a 95% confidence level by the F test for the statistical significance of the reduction in χ^2. Its omission changes the mean value of f_N by 0.1 ppm at 500 kPa and by 0.5 ppm at 100 kPa. The efficient algorithm used for fitting eq (4.1) to the data has been described elsewhere [30].

The dwell time at each frequency prior to the voltage measurements was the longer of $1.2/g_N$ and 3.2 s. The former time was required for the sound field in the resonator to settle sufficiently close to its steady state and the latter time was eight times the post-detection time constant of the lock-in amplifier. The settling time for the frequency tracking circuitry of the lock-in amplifier was less than 0.4 s.

4.2 Random Errors of Resonance Frequency Measurements

When the resonator is filled with argon at a pressure p, and the post-detection time constant is 0.4 s, an approximate expression for the standard deviation of a measurement of f_N is:

$$\sigma(f_N)=10^{-7}f_N\cdot\{1+(100\text{ kPa}/p)^2(6\text{ kHz}/f_N)^2\}. \tag{4.2}$$

At pressures above 100 kPa the signal-to-noise ratio (s/n) is sufficiently high that the imprecision of a measurement is dominated by small, uncontrolled phase shifts in the measurement system (probably in the lock-in amplifier). The loss of precision at low pressures can be understood from the following considerations: The imprecision of a measurement of f_N and g_N is, within a factor of order unity, $g_N/(s/n)$ where s/n is the signal-to-noise ratio of a measurement of the acoustic pressure at the detector transducer. Under the conditions of these measurements, the source transducer is not heavily loaded. It generates an acoustic pressure $k\cdot p\cdot Q$, where k is a proportionality factor, p is the ambient pressure and $Q=f_N/(2g_N)$ is the quality factor of

the resonance under study. Because g_N is dominated by the thickness of the thermal boundary layer, it varies as $p^{-1/2}$. We have:

$$\frac{\delta f_N}{f_N} \approx \frac{g_N}{f_N(s/n)} = \frac{g_N}{f_N}\left(\frac{n}{kpQ}\right) = \frac{n}{2kpQ^2} \approx \frac{2n}{f_N^2 kp^2}. \tag{4.3}$$

The effect of the signal declining as $p^{1.5}$ and the effect of the resonance half-widths increasing as $p^{-0.5}$ conspire to reduce the frequency resolution as p^{-2}. At low pressures, the integration time was increased somewhat; however, at 25 kPa the standard deviation of a typical frequency measurement was 1 ppm. When the resonator is filled at some pressure p with helium instead of argon, the transducer's characteristics are essentially unchanged [31]. The Q of any resonance is the same as the resonator would have had if it were filled with argon at the pressure $p/2.7$. One expects eq (4.3) to give the standard deviation of a measurement of f_N, provided that the characteristic pressure in that equation is replaced with 270 kPa. This expectation is confirmed by the data.

4.3 Systematic Errors in Resonance Frequency Measurements

We consider several possible sources of systematic errors in the procedures for the measurement of the resonance frequencies. We show that systematic errors arising from the frequency standard, nonlinear effects, and the instrumentation for frequency measurement are negligible. The evidence presented in section 4.3.4 shows that the data for the (0,7) mode must be rejected because this radially symmetric mode happens to overlap a neighboring non-radial mode.

4.3.1 Frequency Standard Before and after the measurements reported here, the frequency synthesizer was compared with a standard oscillator which in turn is frequently compared with the signals broadcast by WWV. The comparison revealed that the oscillator within the synthesizer had a frequency 0.20 Hz higher than 10 MHz. The tabulated frequencies have been corrected accordingly.

4.3.2 Nonlinear Effects To minimize possible electrical crosstalk, the drive transducer was not operated with the usual dc bias voltage. Instead, it was supplied with an ac voltage (typically 60 V RMS) at half the desired acoustic frequency. This voltage was obtained by passing the output of the synthesizer through a transformer. Under typical operating conditions (300 kPa, argon, (0,4) mode) the acoustic pressure at resonance was 0.03_5 Pa. The acoustic pressure at resonance varied quadratically with the drive voltage as one would expect with an unbiased drive transducer.

We have searched for possible systematic errors in the measurement of the resonance frequencies resulting from nonlinear behavior of the resonator, and/or the instrumentation and procedures of data acquisition and analysis. The resonance frequencies were unchanged ($\Delta f/f = -0.06 \pm 0.28$ ppm) when the drive voltage was reduced by at least a factor of 3.2 thereby reducing the acoustic pressure by at least a factor of 10. These searches were made at pressures in the range 0.1–1.0 MPa and at the highest and lowest frequencies used and with helium and argon in the resonator.

4.3.3 Ring-Down Experiment In previous work [9], an important check was made of the data acquisition system and the numerical methods used to fit eq (4.1). A 1-liter resonator was filled with propane at 287.5 K and 0.52 MPa. Under those conditions, the (0,2) mode occurred at 2568 Hz and had a half-width of 0.0526 Hz. The mode was excited and then the source transducer was turned off. The detected voltage was measured as a function of time during the "ring-down." The value of $g_{0,2}$ determined by fitting an exponential function to the voltage differed from the value determined by the cw methods described above by only 0.0004 Hz or $1.6 \times 10^{-7} f_{0,2}$. This small difference is consistent with the limitations of the instrumentation mentioned above.

4.3.4 Overlapping Modes The original design for this determination of R included plans to measure the resonance frequencies of the six lowest radially symmetric modes (i.e. $(0,n)$ with $n = 2,3,\ldots, 7$). A complete set of data for these modes has been obtained; however, we shall now argue that the overlap between the (0,7) mode and the adjacent (13,2) mode is so great that inclusion of the data for the (0,7) mode in the final analysis would lead to a systematic error in R and an overestimate of the inconsistencies in the acoustic measurements. The problem is a consequence of the fact that the (13,2) mode is comprised of 27 partially resolved components; thus, its contribution to the detected signal is not a linear function of frequency on the scale of $g_{0,7}$ and eq (4.1) is not a satisfactory representation of the data. Because the widths of the resonances increase as $p^{-0.5}$, the problem of overlapping modes is aggravated at low pressures.

Figure 8 displays the amplitude of the acoustic pressure as the source transducer is swept through frequencies in the vicinity of the (0,2) and (0,7)

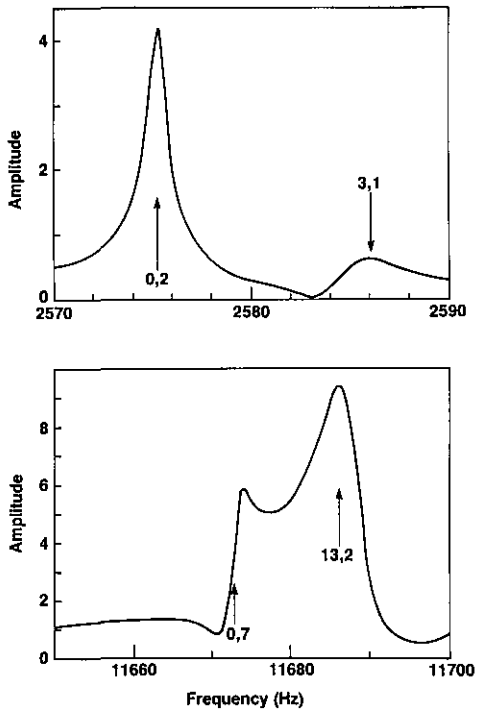

Figure 8. Relative amplitude of the acoustic pressure as a function of frequency in the vicinity of the (0,2) and (0,7) modes.

modes. These data were taken with the resonator near 295 K and filled with argon at 100 kPa. (If the resonator were filled with helium at 270 kPa, the figure would be unchanged, except for a scale factor for the abscissa.) It is clear that the (0,7) mode overlaps the (13,2) mode; the (0,2) mode is better resolved from the (3,1) mode. The (0,3)-(0,6) modes are not displayed here; however, they are even better resolved from neighboring modes.

When eq (4.1) is fitted to the data for the (0,7) mode, there are three indications of problems. First, the value obtained for $F_{0,7}$ changes greatly when the number of fitting parameters is changed from 3 to 4 complex numbers (i.e., whether or not the constraint $C=0$ is imposed). In the case illustrated in the upper part of figure 8 (argon, 100 kPa), $F_{0,7}$ changes by $(-4.1\text{-}4.5i)$ ppm upon changing from 3 to 4 complex parameters. In contrast, the changes for $F_{0,2}$ through $F_{0,6}$ are much smaller: $(1.0+0.9i)$ ppm, $(0.7+0.7i)$ ppm, $(0.2+1.0i)$ ppm, $(-0.1+1.1i)$ ppm, $(-0.4+0.8i)$ ppm, respectively. A second indication of difficulty is that the values of $g_{0,7}/f_{0,7}$ resulting from 3 or 4 parameter fits exceed the theoretical value by 8.6 or 3.7 ppm. (For the other modes, the excess values of $g_{0,s}/f_{0,s}$ are -0.1 to 1.7 ppm from 3 parameter fits; the excess values of $g_{0,s}/f_{0,s}$ are 1.3 to 2.5 ppm from 4 parameter fits.) A third indication of the problem of overlapping modes is that the speed of sound determined from the (0,7) mode is not consistent with that determined from the (0,2)-(0,6) modes. For example, the speed of sound in argon at 100 kPa determined from a 4 parameter fit to the (0,7) mode is 5.7 ppm higher than the mean speed of sound determined from 3 or 4 parameter fits to the (0,2)-(0,6) modes. This 5.7 ppm difference corresponds to 6 standard deviations of the mean for 3 parameter fits to the other modes, and it corresponds to 11 standard deviations for 4 parameter fits.

From the evidence we have just reviewed, it is clear that the data from the (0,7) mode are systematically in error. Accordingly, we neglect them.

5. Thermometry

The temperature of the gas within the resonator was inferred from reading two 25 Ω, capsule-type, platinum resistance thermometers which were embedded in metal blocks attached to the bosses at the top and the bottom ends of the resonator. The imperfections in the measurement of the temperature of the gas contribute approximately 0.9 ppm to the standard deviation of the present determination of R. This includes an allowance of 0.22 mK (0.80 ppm) for imperfections in the measurement of the temperature and an allowance of 0.1 mK (0.37 ppm) for the effects of the temperature gradient that was present across the resonator during the acoustic measurements at $T_t=273.16$ K. We shall now describe the factors which lead to these error estimates. We consider the resistance bridge, the history of the resistance thermometers, the thermal environment of the resonator, and miscellaneous observations which test our understanding of the temperature of the gas.

5.1 Thermometer Calibration, History, and Stability

The resistance bridge and the capsule thermometers together function as a transfer standard between a triple point cell and the resonator. Thus our primary concern is the long term stability of these elements. This has been established by periodically checking the thermometers in triple point cells. In table 4 we list the quantity $R(T_t, i\to 0)$ which is the resistance measured with the ac bridge and extrapolated to zero current at T_t. The average change in $R(T_t, i\to 0)$ between our calibrations is equivalent to 0.22 mK. We believe that this is a

sensible estimate of the errors in our temperature measurements. A standard deviation of all the measurements for each thermometer would be somewhat smaller; however, it might be a misleading measure of error for two reasons. First, the measurements show small correlated changes which plausibly could be attributed to drift in the internal standards of the resistance bridge we used. Second, there is evidence of a secular increase in $R(T_t, i\rightarrow 0)$ for thermometer 835B which we cannot explain. (During recalibration on April 16, 1986, this thermometer was found to be unstable. A subsequent examination showed that the glass seal of the thermometer had a crack which may have formed as it was removed from the resonator and installed in the probe used for insertion into the triple point cell. No instability was evident prior to removing this thermometer from the resonator.)

Table 4. Thermometer calibration data at T_t

Date	Thermometer	$R(T_t, i\rightarrow 0)$ Ω	$\Delta R/\Delta i^2$ μΩ/mA²
June 5, 1986	1888002	25.541645	41
Apr. 17, 1986	1888002	25.541634	40
Apr. 2, 1986	1888002	25.541660	40
Mar. 25, 1986	1888002	25.541625	43
Oct. 10, 1985	1888002	25.541647	48
Apr. 16, 1986	835B	25.915752	72
Apr. 2, 1986	835B	25.915780	80
Mar. 25, 1986	835B	25.915751	79
Oct. 10, 1985	835B	25.915740	86
June 5, 1986	1818362	25.562715	116
Apr. 17, 1986	1818362	25.562703	115
Apr. 4, 1986	1818362	25.562750	116
June 5, 1986	303	25.475649	13
Apr. 17, 1986	303	25.475653	12
Apr. 1, 1986	303	25.475669	14

Table 5 lists values for the parameters α and δ which occur in the equations in the definition of the International Practical Temperature Scale of 1968. The values of δ for three of the thermometers were taken from calibrations made by the NBS Temperature Section in the years 1972–1978, long before the start of this project. The value of the parameter δ for thermometer 835B was assumed to be the same as δ for thermometer 1888002. The values for α were based on these values of δ in combination with the tabulated calibrations at T_t and additional calibrations of each capsule thermometer in a gallium triple point cell. Because all of the measurements of the volume and the resonance frequencies were carried out within 0.05 K of T_t, the uncertainties in α and δ made negligible contributions to the uncertainty in R.

5.1.1 Resistance Bridge The thermometers' resistances were measured using a 4-wire, ac resistance bridge designed by Cutkosky [32] and operated at 30 Hz. The bridge was built and tested by Robert S. Kaeser of the Temperature and Pressure Division of NBS and has been designated NBS/CAPQ Microhm Meter 5. The long term drift of the bridge arises from the drift of the internal standards and was measured at 1.7 ppm in 2 years, relative to a 10 Ω thermostatted Rosa standard. The bridge was normally operated with a measurement current of 1 mA. With our 25 Ω thermometers installed in the resonator, a typical standard deviation of a bridge reading was 3 μΩ which corresponds to 30 μK.

5.1.2 Calibration Probes For calibration, each capsule thermometer was placed in an extension probe similar to that described in Monograph 126 [33]. In the probe, the capsule is surrounded by a carefully fitted copper sleeve. The sleeve is attached with an O-ring seal to the end of a thin walled stainless steel tube designed for insertion into a triple point cell. There were appropriate ex-

Table 5. Summary of thermometer characteristics

Thermometer serial number	1818362	1888002	835B	303
Mean self heating (μΩ/mA²)	116	42	79	13
$\alpha\cdot 10^3$	3.92719_6[b]	3.92677_1[b]	3.92575_8[b]	3.92652_4[b]
δ	1.49612[a]	1.49627[a]	1.49627[c]	1.49638[a]

[a] From calibration by NBS Temperature Section.
[b] From calibration by us at T_t and the Gallium Point.
[c] Assumed.

tension leads and radiation shields inside the tube and a valve atop the tube permitted us to evacuate it and then backfill it with helium. The self-heating coefficients of the thermometers were measured in this configuration during recalibration of the thermometers at T_t. These values are also listed in table 5. The self-heating coefficient of the thermometers changed by less than 10 $\mu\Omega/mA^2$ (0.1 mK) when the thermometers were installed in the resonator.

5.2 Temperature Measurements

The temperature attributed to the gas within the resonator was always calculated from the average of the temperatures indicated by the thermometers in the top and the bottom of the resonator. It was assumed that the combination of the thermometers and the bridge drifted linearly in time between calibrations. Thermometer #1888002 monitored the temperature of the top of the resonator. Thermometer 835B monitored the temperature of the bottom of the resonator until April 15, 1986. Subsequently, thermometer #1818362 was used to monitor the temperature of the bottom of the resonator. A third thermometer (#303 for the critical measurements) was mounted in a threaded copper sleeve which, in turn, was screwed into a tapped hole in the equatorial band on the resonator. A thin layer of vacuum grease was used to improve the thermal contact between the thermometers and their respective sleeves. The self-heating of the thermometers, when installed in the resonator, was within 10 $\mu\Omega/mA^2$ of that measured when the thermometers were in calibration probes.

It was found that the equatorial thermometer was perceptibly coupled to the temperature of the gas within the can (which in turn is coupled to the water bath) as well as to the temperature of the resonator. When the can was filled with argon at 0.1 MPa, the temperature indicated by the equatorial thermometer was approximately $0.94 \cdot T(\text{resonator}) + 0.06 \cdot T(\text{bath})$.

5.3 Temperature Gradients

During the acoustic measurements used to obtain R, a small vertical temperature gradient existed along the resonator. (Typically, the north pole was 0.5 to 0.7 mK warmer than the south pole.) One can show that the resonance frequencies for the radially symmetric modes are determined by the volume average of the temperature distribution and that these frequencies are unaffected by the presence of a temperature gradient [34]. We believe our imperfect knowledge of the volume average of the temperature distribution is no more than 0.1 mK (relative to the calibrations of the thermometers); thus, the effect of the gradient increases the uncertainty in the measurement of R by 0.37 ppm. We now discuss this gradient.

As shown in figure 5, the resonator was hung from the lid of a cylindrical pressure vessel. The pressure vessel was surrounded by a carefully designed water bath. When the water bath was maintained near T_t for an extended period, a steady state developed such that the top of the resonator was 0.5 to 0.7 mK warmer than the bottom. A nearly identical gradient was measured just before and just after the thermometer calibration of April 1–3, 1986. After this calibration, the equatorial thermometer was installed and it indicated a temperature that differed from the mean of the thermometers by no more than 0.2 mK. Concurrently with the calibration, the bath was modified to greatly increase the circulation rate. The thermal grounding of the leads to the transducers, heaters, and thermometers was improved and the radiation traps on the tubes used to conduct the leads from the room through the water bath into the pressure vessel were improved. The gradient was not changed by these modifications. The gradient was unchanged when the depth of immersion of the top of the pressure vessel was increased from 5 to 11 cm and when the top of the bath was insulated. (The sides and bottom of the bath are 7 cm thick including 5 cm of closed cell foam insulation.) When the bath was maintained near the triple point of gallium (29.771 °C) the sign of the gradient reversed and its magnitude was significantly reduced. This suggests that the gradient is the result of a heat leak from the laboratory into the top of the resonator. Additional evidence that there was a genuine heat leak results from the observations that the bath had to be maintained approximately 6 mK below the temperature of the resonator to avoid temperature drifts (when the pressure vessel was filled with argon) and that when the bath and resonator were at the same temperature, the resonator's temperature increased at the rate of 0.6 mK/h. When the pressure vessel was filled with argon, the thermal conductance between the resonator and the bath was 0.3 W/K. (2/3 of this conductance is the result of black-body radiation.) From these observations we estimate that the stray heat input was approximately 1.5 mW. We suspect that radiant heat transport down the filling tube leading from the gas manifold at room temperature to the valve on top of the resonator is responsible

for this heat leak. We attempted to confirm this by heating a portion of the manifold; however, we did not see a change in the 0.2 mK gradient in an experiment which lasted 1 hour. If radiation were indeed responsible for the heat leak, the radiation would have been intercepted by the closed valve on the top of the resonator. The gas within the resonator would be affected only by the temperature gradient induced within the shell, which we have measured.

It is possible to model the temperature distribution that the resonator would acquire in a steady state using the parameters in the preceding paragraph, the dimensions of the resonator, and the known thermal conductivity of stainless steel. A straightforward calculation predicts that at T_t the equator will be 0.15 mK warmer than the south pole and that the north pole will be 0.35 mK warmer than the equator. The same model predicts the gradient will be multiplied by $-1/3$ at the gallium point. These model gradients are consistent with the observations at T_t and at the gallium point, leading us to believe that the volume average of the temperature of the gas within the resonator was known within 0.1 mK, relative to the thermometer calibrations.

We now mention three, negligibly small, sources of heat to the resonator. Under typical conditions used during the acoustic measurements (300 kPa, argon, (0,4) mode), the acoustic pressure at the detector transducer was roughly 0.0023 Pa and the acoustic power dissipated in the thermal boundary layer on the interior of the resonator was 2×10^{-13} W. The resistance bridge dissipated 25 μW in the capsule thermometers mounted in the resonator. This power was divided equally among the three thermometers because they were measured in a cycle which switched the bridge from one to another at 1 minute intervals. The heat conducted from the laboratory to the resonator through the electrical leads to the thermometers and transducers is estimated to be less than 1 μW because of careful thermal grounding of the leads to the lid of the pressure vessel.

5.4 Additional Observations Concerning Thermometry

A few hundred seconds after the valve in the filling port of the resonator was closed, the thermometer attached to the top of the resonator showed a temperature increase of 1–3 mK. This increase relaxed with a time constant of 1800 s, which is what one would expect for heat diffusion in the shell. The final temperatures indicated by the thermometers were identical with the ones before closing the valve, indicating that the top thermometer was responding to a small amount of energy supplied in its vicinity.

The thermal relaxation time of the resonator towards the bath temperature was approximately 33000 s when the resonator is within 0.1–0.01 K of the bath temperature. This is inconveniently slow. When acoustic measurements were made at several pressures with a given sample of gas, the data at the highest pressure were taken first. Then some gas was pumped out of the resonator and its surrounding pressure vessel (in such a way as to avoid large pressure differences across the resonator's wall). As expected, the adiabatic cooling of the resonator was substantial. The resonator was then re-heated to a temperature near T_t using a 5 cm high foil heater which had been glued around the circumference of the equator for this purpose. The temperature inhomogeneities produced by this symmetrically applied heat pulse relaxed with a time constant of 720 s.

It was necessary to keep the valve in the fill port closed during the most precise acoustic measurements. Otherwise, temperature fluctuations in the room would be communicated to the gas in the manifold which in turn would cause the pressure in the resonator to fluctuate. These pressure fluctuations would be too small to change the speed of sound noticeably; however, the adiabatic temperature changes associated with the pressure changes are easily detected.

6. Determination of the Resonator's Volume

6.1 Summary and Results of Volume Determination

In order to determine R, the volume of the resonator must be accurately known at temperatures near $T_t=273.16$ K and at pressures in the range 0–1 MPa. The volume was measured by weighing the quantity of mercury required to fill the resonator when it was maintained at T_t and had equal external and internal pressures of $p_0=101.325$ kPa. Additional measurements were made of the thermal expansion of this volume and its compliance to internal and external pressures. In the following sections we shall describe the measurements, calculations, and diagnostic tests which have led to our conclusions: In the weighing configuration at T_t and at internal and external pressures of p_0, the

internal volume of the resonator was:

$$V_R(T_t,p_0)=(2943.1524\pm0.0036)\ \text{cm}^3 \quad (1.21\ \text{ppm}).$$

At temperatures T between 273 and 303 K and at pressures p (equal inside and outside the resonator) between 0 and 1 MPa, the volume is given by

$$V_R(T,p)=V_R(T_t,p_0)[1-6.18\times10^{-12}\ \text{Pa}^{-1}(p-p_0)$$
$$+47.6\times10^{-6}\ \text{K}^{-1}(T-T_t)]$$

with an additional variance which depends on T and p:

$$[0.6\times10^{-6}\ \text{Pa}^{-1}(p-p_0)\text{ppm}]^2$$
$$+[0.1\ \text{K}^{-1}(T-T_t)\text{ppm}]^2.$$

Upon conversion of the configuration of the resonator from that used for weighing to that used for the measurement of the acoustic resonance frequencies, the volume was increased by

$$(0.0142\pm0.0005)\ \text{cm}^3 \quad \text{or} \quad (4.82\pm0.17)\ \text{ppm}.$$

At T_t and p_0, the uncertainty in the volume of the resonator in the acoustics configuration has important contributions from six sources: The dominant contribution is the uncertainty (1 ppm) in the integrated thermal expansion of mercury in the range 0–20 °C. The five additional contributions to the uncertainty are: the uncertainty which Cook placed on the density of NBS mercury at 20 °C (0.42 ppm), an allowance for possible density changes during storage (0.3 ppm), the random uncertainty in the average of our three volume determinations (0.29 ppm); the uncertainty in the mass of the counterweights (0.14 ppm), and the uncertainty in changing the configuration of the resonator from that used for the volume measurements to that used for frequency measurements (0.17 ppm).

6.2 Principles of Volume Determination

We determined the volume of our resonator from the mass of mercury required to fill it at T_t. The accepted density of mercury is based on the classic work of Cook and Stone [35], who determined the mass of mercury displaced by a cube of known volume; and of Cook [36], who then measured the mass of mercury which filled a cube of known volume. The basic idea of our volume measurement is simply Cook's second method run in reverse. To implement this idea with the required accuracy, we had to reconfigure the resonator to resemble a volume dilatometer. The valve in the north pole of the resonator was replaced with a glass capillary tube and expansion volume assembly. The electroacoustic transducers were replaced with carefully designed plugs.

Our techniques differ from Cook's in other significant details. For instance, rather than weigh the resonator when filled with mercury (a total mass of about 60 kg), we weighed the deficit of mercury from a weighing bottle which was used to transfer mercury to the resonator. By transferring mercury to the resonator in two separate filling operations, the total mass of the filled weighing bottle was kept to less than 25 kg, thus allowing us to use a balance (described below) which has a standard deviation of less than 2 mg.

It is a fundamental assumption in this determination of R that liquid mercury completely filled the resonator during the determinations of its volume. We shall describe extensive tests which would have detected a bubble or a void in the mercury in the resonator if its volume were greater than 0.3 ppm of the resonator's volume. We have also assumed that the volume of the resonator is a stable function of temperature and pressure. We expected that both the compliance and the thermal expansion of the resonator would be determined by its geometry and the properties of 316 stainless steel, without the influence of joints and seals. This expectation has been confirmed by the reproducibility of our volume measurements and by diagnostic tests described below.

The discussion of the volume determination proceeds in the following order. We recall the literature on the density of mercury. The methods we used for weighing mercury and for filling the resonator with mercury are described. The results of the weighings are presented and followed by measurements of the thermal expansion, the compliance, and diagnostic tests for bubbles and voids.

6.3 Density of the Mercury

Cook's two measurements of the density of mercury differed by less than 0.5 ppm. Each measurement was subject to quite different known or suspected systematic errors; thus, the metrological community has placed great confidence in Cook's results. Samples of mercury, directly traceable to Cook, have been used in precision manometry [37] and in the measurement of the so-called "absolute volt" [38]. The mercury we have used is also

traceable to Cook. Indeed, it came from the same NBS stock described in reference [37].

Cook reported a total standard deviation for his measurement of NBS mercury as 0.42 ppm. Sloggett et al. [38] have recently conducted an extensive review of the density of mercury in connection with their redetermination of the absolute volt. They have used Cook's results and have included an additional uncertainty component 0.3 ppm to account for possible changes in the mercury's density during storage and manipulation. We shall do the same.

Cook's measurements were done at a nominal temperature of 20 °C (measured on the IPTS-48 temperature scale) whereas our resonator was maintained at a nominal temperature of 0.01 °C. We must, therefore, correct Cook's value to the temperature of our experiment. We used the expansion formula recommended by Cook [39]. Uncertainty in this correction has been estimated at 1 ppm [35]. Because our temperatures are measured on the IPTS-68, we use an amended thermal expansion formula [40] to correct our density to other temperatures we have measured. Thus, our mercury density is represented (with an uncertainty of 1.13 ppm near 0 °C) as:

$$\rho_{Hg}=13.595078_5\ \mathrm{g\cdot cm^{-3}}/(1+\alpha_{Hg}t_r)$$

$$\alpha_{Hg}=181.5253\times10^{-6}+5.898\times10^{-9}t_r + 3.1507\times10^{-11}t_r^2+2.405\times10^{-14}t_r^3,$$

where t_r is $t/°C$. Cook's densities are reported for mercury at a pressure of 101.325 kPa, while our volume measurements were made at various pressures within 500 Pa of 101.325 kPa and corrected to that pressure using the value 4×10^{-11} Pa^{-1} [41,42] for the isothermal compressibility of mercury.

The mercury we used was stored in soda-lime glass bottles as described in reference [36] and, we believe, had not been touched since the stock was set aside almost 30 years ago. The only preparation given to the mercury was to filter it through a pinhole in order to remove any surface scum.

A sample of the mercury we used was sent to CSIRO in Australia in order to be compared with a sample of their mercury (which was also standardized by Cook) using the high-precision method of Patterson and Prowse [43]. The comparison showed [44] that the CSIRO sample of mercury was (0.0056 ± 0.0005) kg/m^3 denser than ours. This compares favorably with the difference, (0.007 ± 0.006) kg/m^3, measured by Cook. If the densities of these mercury samples did change during the 30 years of storage following Cook's measurements, the changes were identical (within 0.5 ppm) for the CSIRO sample and our NBS sample.

6.4 Weighing

Our guiding principle in design of the weighing aspects of the experiment was that all objects should, as much as possible, have the properties and characteristics of standards used in mass metrology. Volumes of the objects weighed were known well enough so that corrections for air buoyancy could be applied with negligible uncertainty. Temperature and relative humidity were measured within the balance enclosure and atmospheric pressure was measured just outside the balance. The CIPM-81 [45] formula was used to compute the air density.

The balance which we used is described in reference [46]. Its most important features are: 22.7 kg (50 pounds) capacity, single-pan construction (so that substitution, or "Borda" weighing must be used), an enclosure which permits two weights to be interchanged by remote control, and a standard deviation for a single measurement of less than 2 mg.

In practice, we need to know the difference in mass between the weighing bottle filled with mercury and the weighing bottle relieved of about 20 kg. The mass of the filled weighing bottle was balanced against a 50-lb brass standard with a long calibration history. Although its mass does not enter into the final calculation, it is important that the brass weight be stable and that its volume be known to sufficient accuracy [see eq (6.1)].

After partial emptying of its contents into the acoustic resonator, the weighing bottle, along with additional weights, was again balanced against the brass standard. These additional weights were, of course, necessary to make up the deficit in mass of the mercury. Owing to dimensional constraints within the balance, these "counterweights" to the missing mercury had to be specially constructed. The counterweights are crucial to the experiment because it is they which largely determine the mass of the mercury that has been transferred to the resonator. Therefore the counterweights must possess all the properties of a high-quality mass standard and be calibrated in terms of the SI kilogram.

The weighing bottle will now be described, after which we will discuss the counterweights.

6.4.1 Weighing Bottle *The weighing bottle* sketched in figure 9 was constructed of thin-walled austenitic stainless steel. A 2-L stainless-steel

top loading, servo-controlled balance of 15-kg capacity and 0.5 g resolution. The balance was uncalibrated but found to be linear. Each counterweight (distinguished here by the subscript "i") was placed on the balance (in air) and the reading $I_{a,i}$ recorded. Next, a plastic bucket filled with distilled water to which had been added 4 parts in 10^5 (by volume) of non-ionic surfactant was centered on the balance pan. With the bucket in place, the balance was re-zeroed. Then, each counterweight was suspended by monofilament nylon line and lowered into the bucket. The weight, completely submerged, was not allowed to touch the sides or bottom of the bucket. The balance reading $I_{w,i}$ was noted, along with the temperature of the water. To the extent that the effects of surface tension on the nylon suspension and that the volume of submerged nylon are negligible, the density of the suspended weight is:

$$\rho_{cw,i}=\frac{I_{a,i}}{I_{w,i}}(\rho_w-\rho_a)+\rho_a$$

where ρ_w is the density of water in the bucket and ρ_a is the density of the ambient air. The results of the measurements, at 296 K are:

$$\rho_{cw,1}=(7.960\pm0.005)\ \text{g/cm}^3 \quad (14.49\text{-kg weight})$$
$$\rho_{cw,2}=(7.955\pm0.012)\ \text{g/cm}^3 \quad (5.55\text{-kg weight}).$$

These results are in agreement with a handbook [47] which reports that both alloys have a density of 8.0 g/cm^3. The uncertainty estimates were verified by measurements of other objects of known density using the same apparatus.

The masses of the counterweights were determined by direct measurement against NBS mass standards: The smaller counterweight was compared with a 5-kg mass standard plus an assembly of small standards. The larger counterweight plus another assembly of mass standards was compared with a 20-kg mass standard. This time, the 5-kg standard served as the largest weight in the assembly of standards. Finally, both counterweights were compared against the 20-kg mass standard plus an assembly of additional small standards. The three measurements were carried out on two different balances. Final results were arrived at by a linear least squares solution using a weighting scheme which takes into account the differing total variances of each datum [48]. The variances of each measurement were dominated by a combination of the standard deviation of the balance used and the calibration uncertainties of the 20-kg and 5-kg standards.

The mass of the summation of both counterweights is found by the above technique, to be

$$(20041.1783\pm0.0019)\ \text{g} \quad (\pm0.09\ \text{ppm}).$$

The uncertainty does not include any estimate for the possible deviation of the NBS mass standards which we used from the SI unit as defined by the international prototype kilogram. Work in progress leads us to believe that this deviation could result in a lowering of all reported masses by no more than 0.15 ppm.

6.4.3 Weighing Operations In this subsection, we describe the sequence of weighing operations necessary to determine the mass of mercury which went into the resonator. The final weighing equation will be given, along with typical values for each term. Finally, we will demonstrate the long-term stability of our weighing procedures.

We began with a full weighing bottle. The filling port of the weighing bottle was capped by a teflon stopper. The weighing bottle was transported from the acoustics laboratory to the mass metrology laboratory indoors on a cart. Upon arrival in the metrology laboratory, the teflon cap was removed and inspected for mercury droplets. By referring to the weighing bottle as "full," we mean that the level of mercury had been adjusted so that the total apparent mass of weighing bottle plus mercury nearly equaled that of the 50-lb brass weight. Additional, well-calibrated standards were then placed on the weighing bottle to bring its apparent mass to within 50 mg of the 50-lb weight. These additional standards always totalled less than 200 g. Their calibration, even though routine, was known well enough so that negligible error was added to our final result from this source. The 50-lb weight was stored in the balance enclosure throughout the measurements. The full weighing bottle was allowed to equilibrate for at least 3 h inside the balance, although it was kept at room temperature in both the mass metrology laboratory and the acoustics laboratory. During equilibrium, the weighing-bottle port was lightly capped; the cap was removed just prior to the start of weighing.

Weighing was accomplished by single-pan, double-substitution, using a scheme involving five observations [49]. The balance always showed a large drift during the first double-substitution. These measurements were discarded and the weighing continued until the drift rate reached acceptable

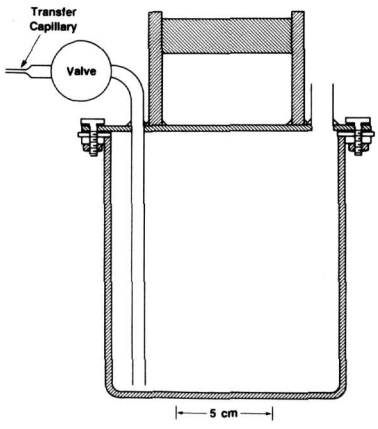

Figure 9. Sketch of weighing bottle.

beaker was modified by the addition of a flange around its rim. A top-plate was bolted onto the flange; the seal between them was made by a teflon gasket. The top plate had a stainless-steel handle welded on, a port for pressurizing or evacuating the interior, and an all stainless-steel bellows-type vacuum valve. A withdrawal tube extended from the valve to the bottom of the beaker. A long, 0.79 mm o.d., stainless-steel, transfer capillary connected to the outlet of the valve was inserted into the resonator when the mercury was transferred. The transfer capillary tube was bent in a loop around the outside of the beaker during weighing operations. As sketched in figure 9, the dimensions of the beaker were chosen so that the height to the flange approximates the diameter.

The volume of the weighing bottle must be known approximately in order to take account of the changes in air buoyancy [eq (6.1)]. For the same reason, the mass of the weighing bottle must be known approximately in order to estimate the mass and the volume of the mercury remaining in the partially emptied weighing bottle. The total mass of the empty weighing bottle was measured to be 1.3987 kg and its volume was calculated to be 191.7 cm^3. The calculation assumed that the density of the stainless-steel beaker and lid was 7.95 g/cm^3 and used separate measurements of the mass and volume of the phenolic knob on the vacuum valve. We estimate that the mass is known to 0.1 g and the volume to better than 10 cm^3.

6.4.2 Counterweights Two weights were constructed to serve as counters to the 1.5 L of mercury removed from the weighing bottle. The first weight has a nominal mass of 14.49 kg and was initially constructed with the idea that it could be used to counterbalance mercury used to fill a 1-L resonator. This weight is made in the shape of a thick disc with diameter 20.5 cm and height of 6 cm. Two small handles were welded onto the top of the disc. The weight is made of austenitic stainless-steel (type 304) and has been buffed to a lustrous finish.

The second weight has a nominal mass of 5.55 kg and is made of similar material (type 316L) with the same surface finish. This weight is tubular in shape, having a height of 9 cm, an inner diameter of 13.5 cm and a wall thickness of 2 cm. The dimensions of the weighing bottle and the two counterweights are such that they can be stacked as shown in figure 10. This assembly can just be accommodated by the balance.

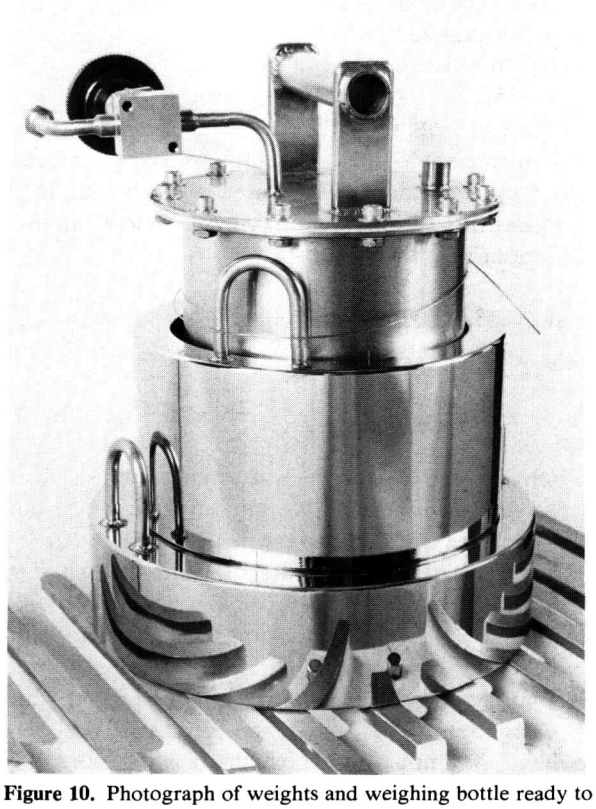

Figure 10. Photograph of weights and weighing bottle ready to be loaded into the balance.

Since the two counterweights are so important to the measurement, considerable care was taken in their calibration. First, their respective volumes were determined. Rather than rely on handbook values for the densities, we measured the density of each weight directly against distilled water. This can be a cumbersome technique for weights of this size. We managed, however, to develop a convenient method which relied on the availability of a

levels. The average of three successive double substitutions was taken as the measured difference between the weighing bottle (plus small standards) and the 50-lb brass weight. The temperature inside the balance and the barometric pressure in the room were recorded midway during each double substitution. The relative humidity inside the balance enclosure was measured at the conclusion of the weighings.

Then the port of the weighing bottle was again capped tightly with the teflon stopper. The vessel was removed from the balance and returned to the acoustics laboratory where approximately 1.5 L of mercury was transferred to the resonator in an operation that will be described in detail below. The nearly empty weighing bottle was then capped and returned to the mass metrology laboratory. Here the weighing process was repeated for the weighing bottle and the counterweights. In all, the weighing bottle was weighed on 17 different occasions against the 50-lb brass weight. (Nine times it was full of mercury and eight times it was nearly empty with counterweights added.) Each time, three double substitutions were taken. The pooled standard deviation of one double-substitution was found to be 1.6 mg (34 degrees of freedom) so that the standard deviation of the average of three double substitutions is taken to be 0.9 mg. (The variance of each set of three double-substitutions was consistent with the pooled value, account being taken of the number of degrees of freedom in each variance.)

The mass of mercury actually transferred is given by

$$m_{\mathrm{Hg}} = \frac{m_{\mathrm{cw}} - \rho_2 V_{\mathrm{cw}} + (\rho_2 - \rho_1)(V_{\mathrm{c}} - V_{\mathrm{P}}) + \epsilon_2 - \epsilon_1 + \rho_1 V_{\mathrm{S1}} - \rho_2 V_{\mathrm{S2}} + \Delta_1 - \Delta_2}{(1 - \rho_1/\rho_{\mathrm{Hg}})} \tag{6.1}$$

where

m_{cw} =	the mass of the counterweights	(20041.1783 g)
V_{cw} =	the volume of the counterweights	(2518.3 cm^3)
V_{c} =	the volume of the 50-lb, brass standard	(2702.9 cm^3)
V_{P} =	the volume of the weighing bottle plus remaining mercury	($\sim$280 cm^3)
ϵ_1 =	mass of small standards added to full weighing bottle	($<$200 g)
ϵ_2 =	mass of small standards added to nearly empty weighing bottle	($<$200 g)
V_{S1} =	volume of ϵ_1	($<$25 cm^3)
V_{S2} =	volume of ϵ_2	($<$25 cm^3)
Δ_1 =	balance difference for full weighing bottle	($\sim\pm$20 mg)
Δ_2 =	balance difference for nearly empty weighing bottle	($\sim\pm$20 mg)
ρ_{Hg} =	density of mercury	($\sim$13.5378 g/cm^3)
ρ_1 =	density of air during weighing of full weighing bottle	($\sim$1.18 mg/cm^3)
ρ_2 =	density of air during weighing of empty weighing bottle	($\sim$1.18 mg/cm^3).

Two such complete weighings were required in filling of the resonator. The total uncertainty in the mass of mercury transferred to the resonator is estimated to be 4.2 mg (0.10 ppm). This follows directly from a propagation of error in eq (6.1). This equation takes air buoyancy into rigorous account but ignores surface differences. For example, changes in relative humidity between runs could affect the mass of the stainless-steel counterweights and this is not accounted for by eq (6.1). We have made reasonable assumptions concerning the possible extent of these effects [50] and find them to be negligible.

In the course of the measurements, we made several observations which give us confidence that the weighings were accomplished to the stated accuracy. Firstly, we had an opportunity to weigh a full weighing bottle twice, 3 days apart. By chance, the ambient air density changed by 2% between the measurements. Such a change is unusually large but should be accounted for if buoyancy corrections have been correctly applied. Indeed, the apparent mass difference between the weighing bottle and the 50-lb brass weight changed by almost 20 mg but this difference was reduced to less than 0.5 mg after the buoyancy correction was applied. On another occasion, there was a 6-month hiatus between successive measurements of the same full weighing bottle. Again, results repeated to within one standard deviation. Finally, on returning a full weighing bottle to the acoustics laboratory, we accidentally allowed a few beads of mercury to escape past the teflon stopper. These were recovered and weighed. The weighing bottle was also reweighed and the results showed that we had recovered the spilled mercury within the precision of

the weighings. This observation supports our assumption that close observation of the weighing bottle and its surroundings would have revealed other mercury spills of any significance.

6.5 Filling the Resonator with Mercury

In this section we describe how mercury was transferred to the resonator and under what conditions we know the resonator's volume.

When ready for filling with mercury, the resonator was configured to look very much like a volume dilatometer. Since the electroacoustic transducers were incompatible with mercury, the ports in the wall of the upper hemisphere were replaced by plugs of special design (fig. 11). Note that the seal was made gas-tight by compression of a 1.6 mm-thick Viton [29] gasket of rectangular cross-section rather than by an O-ring. Our design has advantages over a conventional O-ring seal because the gasket completely fills the annular volume in which it is seated and its compliance does not determine the position of the inner face of the plug with respect to the inner surface of the resonator. This important distance is completely determined by metal to metal contact. A useful design detail is that the screws which compress the gasket were slotted lengthwise to facilitate helium leak testing of the seals.

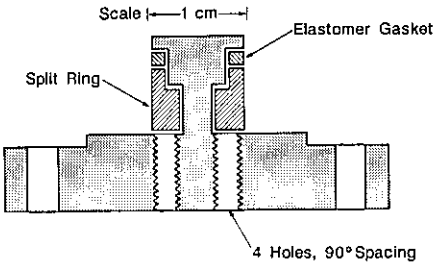

Figure 11. Plug used to seal transducer ports during the measurement of the resonator's volume.

As shown in figure 12, the valve at the top of the resonator was replaced with a glass capillary and expansion volume assembly. The assembly was sealed to the resonator by compressing a thin (50 μm) mylar gasket as shown in greater detail in figure 13. The expansion volume was fitted with a side arm, which was used to evacuate the resonator and to back-fill it with argon. A vacuum coupling at the top of the expansion volume assembly was used to seal the stainless-steel transfer capillary which carried mercury from the weighing bottle into the resonator. After the transfer capillary was withdrawn for the weighings, the coupling was sealed with a plug.

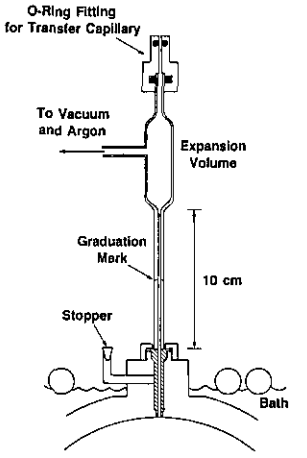

Figure 12. Expansion volume assembly installed on the resonator for the measurement of the resonator's volume.

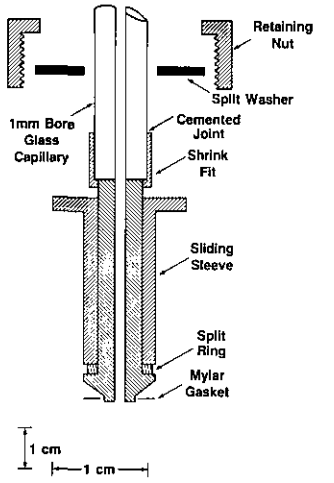

Figure 13. Fitting for sealing the resonator to the glass capillary and expansion volume assembly during transfers of mercury. Note: horizontal scale is magnified 2× compared with vertical scale.

The resonator was immersed in a stirred bath of water and methanol whose temperature was controlled to ±1 mK at a nominal 273.16 K. The upper surface of the water was insulated with a layer of hollow polypropylene spheres. The temperature of the resonator at its equator was measured with a calibrated PRT. Thermal gradients about the outside of the resonator were found to be insignificant.

We now describe a typical sequence of operations necessary to fill the resonator with mercury and to determine the volume filled under precisely defined conditions of temperature and pressure.

To begin, plugs were installed in the transducer ports and tested for leaks using a helium detector. The resonator was backfilled with argon and was lowered into the constant-temperature bath. The weighing bottle was placed on a top-loading electronic balance and the stainless-steel transfer capillary was threaded through the expansion volume assembly (fig. 12) into the resonator. The system was evacuated for 15 min in this configuration in order that any mercury in the stainless-steel capillary would be blown into the resonator rather than into the glass expansion volume. The stainless-steel capillary was then withdrawn (sliding through the O-ring seal) as far as the expansion volume so as not to block the glass capillary. The resonator was then evacuated by a diffusion pump fitted with a trap cooled by a slurry of solid CO_2 and alcohol. Evacuation was slow because of the low conductance of the 1.1 mm i.d. glass capillary tube. The minimum time required for sufficient evacuation was calculated to be 3 hours but we preferred to pump the system overnight.

After evacuation, the stainless-steel capillary was slid down through the glass capillary and into the resonator. The valve on the weighing bottle was opened, and mercury flowed into the resonator under gravity. This 3-hour long process was conveniently monitored by reading the digital balance on which the weighing bottle sat. When the balance indicated that 1.5 L of mercury had been transferred, the transfer was stopped and the half-full resonator was backfilled with argon. The stainless-steel transfer capillary was withdrawn from the expansion volume assembly and the mercury which it contained allowed to drain back into the weighing bottle. The expansion volume was then plugged and the resonator again evacuated and backfilled with clean argon. At this point, the weighing bottle was reweighed, refilled with mercury, and weighed again.

The weighing bottle was then reconnected to the resonator and the transfer of mercury continued in the same way as just described. As mercury finally appeared in the expansion volume, the stainless-steel capillary (with mercury still flowing) was withdrawn to a level just below the mercury surface. This tends to prevent the formation of voids in the glass capillary. The mercury flow was then turned off, the stainless-steel capillary completely withdrawn (as described above), and the volume above the mercury surface again backfilled with clean argon.

At this stage, the mercury level was in the expansion volume. The level was lowered until the meniscus was about midway in the glass capillary by withdrawing mercury using a syringe with special needle. The excess mercury was carefully returned to the weighing bottle. Then, the resonator was again sealed and the volume above the meniscus flushed with clean argon. The now nearly-empty weighing bottle was weighed for the last time, as described above.

Since the resonator was suspended in a water bath rather than in a vat of mercury, the pressures on the inside and outside of the resonator were not equal. However, by adjusting the pressure above the mercury, we could cause the pressures at one horizontal plane to be equal inside and outside the resonator. In order to take advantage of the symmetry of the resonator, we chose the plane of equal pressure to be that of the equator. Then the upper hemisphere was under compression while the lower hemisphere was under tension of equal magnitude. This symmetry suggests that the total volume is identical with the volume of a resonator jacketed by mercury and the suggestion is confirmed by the exact solution of the partial differential equation for the elastostatic equilibrium of a thick shell [51].

Equation (6.2) gives the exterior pressure at the equator and eq (6.3) gives the interior pressure at the equator.

$$p_{\text{ext}} = p_{\text{atm}} + \rho_{\text{w}} g d \tag{6.2}$$

$$p_{\text{int}} = p + \rho_{\text{Hg}} g (h - h_{\text{b}} + a) + \frac{2\sigma}{r} |\cos\varphi_{\text{l}}|, \tag{6.3}$$

where

p_{atm} = ambient atmospheric pressure
p = argon pressure above mercury meniscus
d = depth of equator below surface of water bath
ρ_{w} = density of the bath liquid (water + methanol)
$h - h_{\text{b}}$ = height of mercury meniscus from bottom of fill tube
a = inner radius of shell
σ = surface tension of mercury $\simeq 0.46$ N·m^{-1}
r = radius of glass capillary (0.557 mm)
φ_{l} = contact angle for mercury on glass (133°)

Notice that in eq (6.3), h is itself a function of p. In order to solve eqs (6.2) and (6.3) simultaneously, it is necessary to obtain h explicitly in terms of p. This was done by linear regression analysis of h against p, where both h and h_b were measured relative to a fiducial mark on the capillary tube using a cathetometer. Given that the result of this fit is

$$h = h_0 + h_1 p, \tag{6.4}$$

the pressure p at which the interior and exterior equatorial pressures are equal is:

$$p_m = \Big(p_{atm} + \rho_w g d - \rho_{Hg} g (h_0 - h_b + a) - \frac{2\sigma}{r} |\cos\varphi_l| \Big)/(1 + \rho_{Hg} g h_1). \tag{6.5}$$

In practice, the capillary was long enough to vary the pressure above the mercury from 50 kPa to 250 kPa, and the resulting curve was also extremely useful as a diagnostic tool, as we shall explain below.

6.6 Results of Weighing

The volume of mercury which fills the resonator is calculated from the following simple formula:

$$V_R = (m_{in}/\rho_{Hg}) - V_{tube}(p_m).$$

Here m_{in} is the net mass of mercury transferred to the resonator from the weighing bottle during the two fillings; ρ_{Hg} is the density of mercury at the bath temperature (273.16 K) and at the equatorial pressure; $V_{tube}(p_m)$ is the volume of mercury in the fill assembly when the pressure above the meniscus is p_m. V_{tube} was determined as a function of h in a separate experiment with result:

$$V_{tube}(h) = -4.7\ \text{mm}^3 + 0.973\ \text{mm}^2\ (h - h_b).$$

(This expression is valid only for values of h within the glass capillary.) We measured h as a function of p, as discussed above, and we can use the experimentally determined parameters of eq (6.4) to find V_{tube} at p_m:

$$V_{tube}(p_m) = [-4.7\ \text{mm}^3 + 0.973\ \text{mm}^2 (h_0 - h_b)] + 0.973\ \text{mm}^2 h_1 p_m.$$

In all, the resonator's volume was measured three times, with results shown in table 6. Note that measurements two and three were made about 1/2-year apart. The plugs were removed and replaced between volume measurements. We can use the range in the three measurements to estimate a standard deviation of 0.51 ppm for a volume measurement [52], giving an estimated standard deviation of 0.29 ppm for the average. This estimate does not yet include errors which are systematic to the three measurements. It is interesting to note that, although our volume is an order of magnitude larger than that used by Cook [36], our relative precision is not improved over that of Cook.

Table 6. Three measurements of resonator's volume, V_R

Fill #	1	2	3
Date	1985 Sept.	1985 Sept.	1986 Apr.
T(K)	273.159	273.158	273.158
$p_{equator}$(kPa)	101.8	101.1	101.0
h_1(mm/kPa)	−0.2101	−0.2099	−0.2086
m_{in} (g)	40014.158	40014.153	40014.251
m_{out} (g)	40014.118	40014.117	
$V_R(T_0,P_0)$(cm^3)	2943.1540	2943.1515	2943.1518

Besides measuring the mass of mercury necessary to fill the resonator, we also measured the mass of mercury withdrawn from the resonator when it was emptied. This was done for the first two fillings only and is also shown in table 6 as m_{out}. Note that in both cases, a mass of about 40 mg was either left behind or lost. This corresponds to a fractional volume of 1 ppm, which would be produced by a remnant mercury droplet of radius less than 1 mm. To ensure that any such droplet was ultimately eliminated, the resonator was washed with alcohol after the first and third determinations of the volume and was evacuated at elevated temperature subsequent to the second determination of the volume.

In order to correct each result to a temperature of 273.16 K and an equatorial pressure of 101.325 kPa, it was necessary to know the thermal expansion and the compliance of the resonator's volume. The experimental determinations of these quantities and measures of their accuracy are described in the next section.

6.7 Thermal Expansion

The volume coefficient of expansion of stainless-steel was determined from a handbook [47] value for α_L, the linear coefficient of expansion in the

interval 0–100 °C. The value is:

$$\alpha_V \equiv \left(\frac{1}{\Delta T}\frac{\Delta V}{V}\right) = 3\alpha_L = 47.7\times 10^{-6}\,\mathrm{K}^{-1}.$$

We measured α_V directly, because it is conceivable that a structure consisting of two bolted hemispheres with plugged holes might not expand exactly as a homogeneous metal shell. After the second measurement of the resonator's volume and before the resonator was emptied of mercury, the bath temperature was raised to 302.927 K (the triple point of gallium). With the resonator now behaving like a thermometer bulb, mercury rose in the capillary and filled a portion of the expansion volume. Mercury was then withdrawn by syringe until the meniscus was once again about midway up the glass capillary. The mercury which had been withdrawn was weighed and the volume of the remaining mercury was determined by the methods outlined above. The result of this procedure yielded a value for the thermal expansion of the resonator between 273.16 and 302.93 K:

$$\alpha_V = 47.59\times 10^{-6}\,\mathrm{K}^{-1}$$

in remarkable agreement with the handbook value.

6.8 Compliance

The compliance of the spherical resonator was determined by three methods: 1. theoretically, based on equations for a thick, spherical shell [53] and published values for the elastic properties of 316 stainless-steel [47,54]; 2. experimentally, by measuring acoustic resonance frequency as a function of changes in the external pressure of the resonator; and, 3. experimentally, by measuring the functional dependence of h with p during volume determinations. The last technique used a published value for the compressibility of mercury which is accurate to about 0.5 percent at the pressure and temperature of interest [41,42].

6.8.1 Theoretical Values of Compliance The theory of elasticity can be used to calculate the changes in the interior volume of a thick-walled, isotropic, spherical shell in response to pressure changes [53]. The required data are: the inner radius (88.9 mm), the outer radius (108.0 mm), Young's modulus (197 GPa [47,53]), Poisson's ratio (0.297 [54]), and the initial and final interior and exterior pressures. We define the compliance of the shell as

$$\chi_s = \frac{3\Delta a}{a}\frac{1}{\Delta p},$$

where a is the nominal interior radius.

Based on this model, the two experimental determinations of compliance are expected to have significantly different magnitudes. In the first experimental determination, the internal pressure remains fixed while the external pressure is varied. In the second determination, the external pressure remains fixed while the internal pressure varies. The theoretical predictions for these two cases are:

$$\chi_{s,o} = -3.631\times 10^{-11}\,\mathrm{Pa}^{-1} \quad \text{(outer pressure varies)}$$
$$\chi_{s,i} = 3.012\times 10^{-11}\,\mathrm{Pa}^{-1} \quad \text{(inner pressure varies).}$$

In addition, we are interested in the case where the inner and outer pressures remain equal:

$$\chi_{s,e} = -6.19\times 10^{-12}\,\mathrm{Pa}^{-1} \quad \text{(equal inner and outer pressure)}$$

(Note that $\chi_{s,e} = \chi_{s,o} + \chi_{s,i}$.) These calculations are subject to significant errors from the assumed value of elastic constants (about 2%) and, perhaps more seriously, from the assumption that the elastic properties are isotropic throughout the shell. The latter assumption leads to errors in $\chi_{s,e}$ which have been "optimistically" estimated at 10% for well-annealed structures of austenitic stainless-steel [55].

6.8.2 Experimental Variation of the Outer Pressure The compliance upon variation of the outer pressure was measured in a simple auxiliary experiment which exploits the fact that the acoustic resonance frequencies are proportional to the inverse cube root of the resonator's volume. The resonance frequencies were measured with helium at a pressure of 438 kPa both inside and outside the resonator. With the pressure inside the resonator held constant, the exterior pressure was reduced to 36 kPa and the resonance frequencies were remeasured. Finally the exterior pressure was restored to its original value and the frequencies were measured a third time. The pressure change resulted in fractional changes in the resonance frequencies of four distinct acoustic modes ranging from -5.1 to -5.2 ppm. Upon restoration of the external pressure, the resonance frequencies averaged 0.1_4 ppm below their initial value. (This very small, apparent hysteresis is most likely a result of incomplete thermal equilibration.) These results can be interpreted as a measurement of the compliance:

$\chi_{s,o}=(-3.85\pm0.13)\times10^{-11}$ Pa^{-1}.

Thus the experimental compliance exceeds the theoretical compliance by about 6%; however, this difference is within the combined errors.

6.8.3 Experimental Variation of the Inner Pressure The compressibility of the resonator when the inner pressure is varied can be derived from the measurements of h as a function of p, which have been described above. When fit to a straight line, the slopes, measured for three separate fillings, have a weighted average value of −0.2098 mm/kPa with a pooled standard deviation of 0.0004 mm/kPa. Knowledge of the nominal volume of the resonator and the measured diameter of the glass capillary leads directly to the total compliance,

$$\chi_T=(6.93\pm0.01)\times10^{-11}\ \text{Pa}^{-1},$$

with a random uncertainty of only 0.2 percent. This total compliance includes the isothermal compressibility of the mercury which is $(3.90\pm0.02)\times10^{-11}$ Pa^{-1} [41,42]. When it is subtracted from χ_T, one obtains the compliance of the shell:

$$\chi_{s,i}=(3.03\pm0.03)\times10^{-11}\ \text{Pa}^{-1}$$

Remarkably, this result is only 0.6% greater than the calculated value for $\chi_{s,i}$.

The compliance determined in this experiment is subject to possible systematic errors from two sources. First, a trapped bubble of gas could have led to an erroneous result. Second, mercury may have penetrated unsuspected cracks and pores in the shell and its plugs. Such penetration will be a function of pressure and pore diameter [56] and could be misinterpreted as shell compliance. Because either of these effects might have led to a serious error in the determination of V_R, it is useful to show that they have not occurred.

Our best experimental evidence is based on an analysis of the h vs p curves. A typical plot is shown in figure 14 (top). Figure 14 (bottom) shows the residuals to the least squares fit to eq (6.4). One is immediately struck by the very small residuals and the clear evidence of hysteresis. All the residuals for points taken with the meniscus falling (caused by raising the pressure) lie above the residuals for the meniscus rising. The average difference between residuals amounts to 0.045 ppm of the resonator's volume. This very small value of the hysteresis occurred for all three measurements and might be explained as an effect of incomplete thermal equilibration or as an effect of hysteresis in the mercury-glass contact angle, as discussed in the next paragraphs.

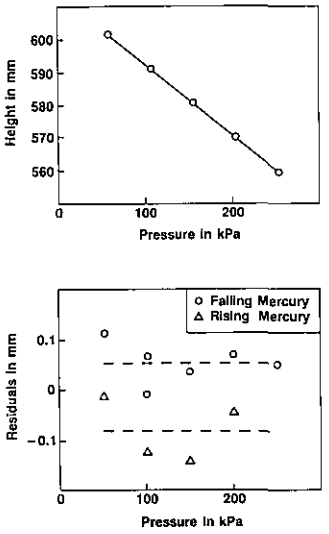

Figure 14. Top: Typical plot of the height of the mercury in the glass capillary as a function of the applied pressure. Bottom: Residuals from a linear fit to the height data.

In taking data for figure 14, the pressure was incremented or decremented in steps of about 50 kPa. When the pressure is incremented by Δp, the adiabatic temperature increment of the mercury is given by the expression

$$\Delta T=\frac{\Delta p\,\alpha_{Hg}T}{\rho_{Hg}c_p},$$

where c_p is the specific heat capacity of mercury at constant pressure [41]. When Δp is 50 kPa, ΔT is 1.3 mK. This temperature increment will relax towards the bath's temperature with a time constant which we estimate using reference [57] to be in the range 270–350 s. (The range results from different approximate treatments of the effect of the shell on the heat flow problem.) As it happened, our experimental protocol called for an equilibration time of 600 s, the time found necessary for the meniscus height to attain equilibrium within 0.1 mm. The 0.14 mm hysteresis on figure 14 is consistent with this protocol and with the condition that, at the time of the height measurement, the average temperature of the mercury had relaxed to 0.13 mK from the bath's temperature. Approximate solutions to the heat flow problem yield average tem-

perature differences at 600 s in the range 0.08–0.14 mK; thus incomplete thermal relaxation is one mechanism with the correct sign and order of magnitude to explain the observed hysteresis.

Another mechanism which might explain the hysteresis is the documented difference between the "advancing" and "receding" contact angles between mercury and glass. Ellison et al. [58] report that at 25 °C, the maximum advancing contact angle of mercury on polished glass is 147°, the minimum receding contact angle is 122°, and the equilibrium contact angle is 133°. Contact angle hysteresis could appear on the h vs p curves as a hysteresis in p as large as $(2\sigma/r)\times(\cos(122°)-\cos(147°))=510$ Pa, which corresponds to 0.11 mm on figure 14 (bottom).

6.8.4 Temperature Dependence of the Compliance As mentioned in section 6.7, the thermal expansion of the resonator was measured between the temperature of the triple point of water and the gallium point. Measurements of h vs p made at the gallium point were also used to determine the temperature coefficient of χ_T, the total isothermal compliance of the resonator filled with mercury. The measured value was in satisfactory agreement with our estimate of the sum of mercury and shell contributions. The estimate used the temperature dependence of the compressibility of mercury reported in reference [41] and the temperature dependence of the shell's compliance calculated from the thermal coefficients of the elastic constants [54].

6.9 Tests for Bubbles and Voids

In this determination of R, we have assumed that liquid mercury completely filled the resonator during the determinations of its volume. This section describes the measurements and tests which give us a high degree of confidence that this assumption is justified.

The measurements of the meniscus height as a function of the applied pressure can put an upper bound on the total volume of any "large" bubbles that might have been present in the mercury in the resonator. We consider the question: "how large a bubble volume could exist, unseen below the glass capillary, when the pressure above the meniscus was 70 kPa (the approximate gas pressure at which the resonator's volume was determined)?".

The compressibility of a bubble can be estimated with the ideal gas law. The correction for surface tension can be neglected for "large" bubbles. The pressure inside a bubble depends upon its vertical position in the resonator; however, this consideration has only a small influence on the model calculations which follow.

To answer the question, we first computed h vs p curves for various sizes of bubbles in the resonator as the pressure above the meniscus varied from 50–250 kPa. We fit these curves to straight lines and examined the residuals from the fit as in figure 14. A total bubble volume at 70 kPa of 0.1 ppm of the resonator's volume could not be distinguished from the residuals of figure 14; however, a bubble volume of 1 ppm would lead to residuals which were well off the vertical scale in both directions. We concluded that a total bubble volume of about 0.3 ppm of the resonator's volume would certainly have been detected.

A similar argument can place upper bounds on the volumes of possible pores, small bubbles, or cracks in the walls of the resonator (such as would have resulted in the unlikely event that the extrusion of the wax from the equatorial seam were incomplete). Mercury intrusion porosimetry is a well-developed analytical technique [56]. At a pressure p, mercury will fill a pore of diameter D according to the relation

$$D=4\,\sigma\,|\cos\varphi_2|/p,$$

where φ_2 is the contact angle of mercury on stainless steel [58]. Thus at 50 kPa all pores of diameter 27 μm and larger should already be filled. At the highest pressure, 250 kPa, pores down to a diameter of 5 μm will be filled. The filling of a single pore will be accompanied by a discontinuous jump in the h vs p curve. The pressure at which the jump occurs determines the diameter of the pore just filled and the magnitude of the discontinuity follows from the pore volume.

From the above single pore model and our compressibility data we concluded that the pore volume entered by the mercury between pressures of 50 kPa to 250 kPa was less than 0.1 ppm of the resonator's volume. At the other extreme from a model of discrete pores, we can imagine a continuous distribution of pore diameters and volumes which would change the slope of the h vs p line instead of producing step-wise discontinuities. The agreement between the measured value of $\chi_{s,i}$ with that calculated from the theory of thick shells would not have been possible, however, if the volume contained in such a continuous distribution were greater than 0.1 ppm of the resonator's volume.

Finally, we recall that in section 6.8.4 we reported that the measured temperature dependence of χ_T was in satisfactory agreement with the value calculated from published data for mercury and 316 stainless steel. The presence of a bubble of sufficient size would have destroyed this agreement. Based on the uncertainties involved in checking the temperature dependence of the compressibility, we put the size of a possible bubble at less than 0.3 ppm of the resonator's volume. This limit is the same as was found in the analysis of the compressibility data at 273.16 K.

6.10 Corrections from Weighing Configuration to Acoustics Configurations

The small difference in volume between the calibration and operational configurations of the resonator was determined in auxiliary experiments and calculations. The difference results from three changes: 1. the expansion volume assembly is replaced with a valve, 2. the plugs are replaced with the electroacoustic transducers, and 3. the resonator is supported from the valve at the north pole instead of three bolts tangential to the equator.

The volume displaced by the valve stem (in the closed position) was compared with that of the filling-tube adaptor by simple mechanical measurements. These were performed using a dummy valve body fabricated to the same internal dimensions as the filling port of the resonator. The surface corresponding to the inner wall of the resonator was machined flat and served as a reference plane for the measurements. Using a calibrated dial gage supported in the chuck of a milling machine, the expansion volume assembly was found to extend forward of the reference plane by $(0.20\pm0.01_3)$ mm. This measurement was performed with a mylar gasket in place and with the retaining nut tightened so as to mimic the expansion volume assembly used during calibration of the resonator. Similarly, the firmly closed valve stem was measured to be $(0.31\pm0.01_3)$ mm behind the reference plane and we therefore add (4.0 ± 0.2) mm^3 to the volume of the resonator to account for this difference.

The volume displaced by the transducer assemblies was compared with that of the stainless-steel plugs by measurements of acoustic pressure with a small sealed coupler. This scheme was adopted because the tensioned diaphragms on the transducers were too delicate to permit dimensional measurements using mechanical contacts. As shown in figure 15, the coupler consisted of a brass bar bored through to the diameter of the transducer ports. Each end of the coupler was provided with bolt holes so that either a plug or a transducer assembly could be installed. With both ends closed in this manner, the free volume within the coupler was approximately 370 mm^3. A second hole bored through the side of the coupler and fitted with an O-ring seal accommodated a microphone (B&K type 4138) [29]. The microphone was used in conjunction with a preamplifier (B&K type 2660), a lock-in amplifier, and a digital voltmeter to measure the acoustic pressure. One end of the coupler was closed by a transducer assembly which was driven as a frequency-doubling source by a constant excitation signal at 500 Hz. The other end was closed either by the second (passive) transducer assembly or by one of the two plugs. The acoustic pressure was measured (with ambient air inside the coupler) in each of the three possible configurations. The plugs and transducers were sealed in the apparatus in exactly the same way as they would be in the spherical resonator. The roles of the active and passive transducers were then reversed in order that the displacement of the second transducer could be compared with that of the plugs. In each case, the free volume V_i was taken to be inversely proportional to the measured acoustic pressure p_i so that a comparison of two configurations i and j gives

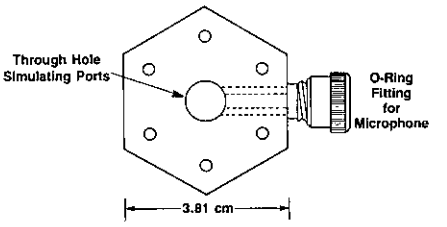

Figure 15. Acoustic coupler used to measure the difference between the volumes displaced by the electroacoustic transducers and the volumes displaced by the plugs which replaced the transducers during volume measurements.

$$(V_i/V_j)=(p_j/p_i)$$

$$V_i-V_j=V_j(p_j-p_i)/p_i\approx 370\ \text{mm}^3\,(p_j-p_i)/p_i, \quad (6.6)$$

where the approximation is valid for small differences in volume. The results are summarized in table 7 and lead us to increase the measured volume by (12.4 ± 0.1) mm^3, where the small uncertainty is based on the close agreement between the different permutations of plugs and transducers; it does not include any assessment of systematic uncertainty.

Table 7. Data for correction of volume change from configuration change

Active transducer	Passive transducer	Plug	δV, mm^3
1	2	1	1.3_8
1	2	2	1.0_3
2	1	1	11.3_6
2	1	2	11.1_4

$\delta V = V(\text{transducer}) - V(\text{plug})$.

The only significant systematic uncertainty results from the effects of the "annular" gaps which occur between the wall of the resonator or the coupler and the plugs or transducer housings. (Note: there was no centering mechanism to guarantee that the gaps were actually annular.) Beads of mercury were always found in the gaps when the plugs were removed from the resonator's ports between volume measurements, leading us to assume that mercury filled the gaps during volume measurements. The volume in the gaps was found to be (1.40 ± 0.10) mm^3 from dimensional metrology. (The diameters of the plugs were 9.51_2 and 9.50_0 mm; the distances between their ends and the gaskets were 1.78 and 1.73 mm. The diameters of the ports were 9.54_5 mm and 9.52_0 mm.)

The geometric volumes of the gaps between the plugs and the hole through coupler adds up to 1.0 mm^3. (The i.d. of the coupler is 9.52_5 mm.) The geometric volumes of the gaps between the transducer housings and the hole through the coupler add up to 5.0 mm^3. (One transducer housing extends into the coupler 8.68_2 mm and is 9.50_2 mm in diameter; the other extends 8.72_0 mm and is 9.51_2 mm in diameter.) We now consider the question: what is the effective volume of these gaps as measured by the acoustic field when the plugs or the transducers were in the coupler? In all these cases, the widths of the gaps were much less than the viscous and thermal penetration lengths (70 μm and 81 μm, respectively) for motions of air at the measuring frequency (1 kHz). Under such conditions, sound propagation in the gaps is essentially isothermal and the effective volume of the gaps can exceed the geometric volume by a factor as large as γ ($\gamma \approx 1.4$ for ambient air), if attenuation in the gaps is neglected. If attenuation in the gap is considered, the effective volume can be much smaller than the geometric volume. The effective volume can be calculated for a long slot of depth D with plane walls separated by a distance d. The result is [27]:

$$V_{\text{eff}} = (-i\beta/kD)V_{\text{geometric}},$$

where $k = 2\pi f/c_{\text{air}}$ is the propagation constant for sound in air and β is the specific acoustic admittance given by

$$\beta \approx \{(1+i)(3\gamma)^{1/2}/6(\delta_s/d)\} \times \tanh\{(1+i)(3\gamma)^{1/2}(\delta_s/d)kD\}. \quad (6.7)$$

For each of the gaps under discussion, V_{eff} is a comparatively small complex quantity whose real part must be added to the much larger "free volumes," (V_i and V_j) in eq (6.6) to obtain the volume difference from the measurements of the amplitudes of acoustic pressures [p_i and p_j in eq (6.6)]. For each gap, V_{eff} was calculated twice using eq (6.7) with different assumptions representing two extreme cases. First, we assumed that the gap was exactly annular and that its width, d, was half the difference between the diameter of the hole in the coupler and that of the inserted object. Second, we assumed that the inserted object was in contact with the wall of the coupler somewhere on the circumference. This led to a gap whose width varied as $d \cdot \sin^2(\theta)$ where θ measures the angle from the point of contact. In this case a numerical integration of eq (6.7) was necessary. Under these different assumptions, the real parts of the effective volumes for the plugs in the coupler totalled 1.3_2 mm^3 and 1.3_1 mm^3, respectively. For the transducer housings in the coupler, the effective volumes totalled 1.5_3 mm^3 and 2.7_6 mm^3. We shall take the average of the effective volumes computed under the two extreme assumptions as the best estimate of their values. For purposes of propagation of errors, we shall take 1/3 of their difference as an estimate of the standard error in the calculations. Another contribution to the error in these calculations results from the imperfect measurements of the average width of each gap (± 0.0018 mm) and is added in quadrature.

Several other phenomena enter into the comparison of the volumes displaced by the plugs to the volumes displaced by the transducers; however these had negligible effects on the results. For example, the volumes were compared at room temperature; however their difference must be known at T_t. The plugs were made of type 304 stainless-steel and the transducer housings were made of brass; however, the effect of the difference in their thermal expansions is very small (≈ 0.02 ppm of the resonator's volume). A portion of the volume displaced by the transducers is bounded by a compliant diaphragm. The compliance increases the apparent volume displaced in the coupler by a very

small amount which is proportional to (pressure/frequency) at frequencies well below the diaphragm's resonance ($\approx$100 kHz). From information provided by the manufacturer, the equivalent extra volume is on the order of 0.15 mm^3 (0.05 ppm) for each transducer under the conditions of the comparison.

While the resonator's volume was measured, the resonator hung in the water bath from three vertical bolts which were screwed into holes in the cylindrical portion of the resonator near the equator. While the acoustic measurements were carried out, the resonator was hung from the valve body attached to the north pole. In this latter configuration, the sagging of the resonator under its own weight increased its volume by 0.04 ppm over that determined in the weighing configuration. This increase was estimated from an exact solution to the partial differential equation for elastostatic equilibrium for a thick, homogeneous, spherical shell [51].

We shall now summarize the results of this section. The volume of the resonator determined by weighing the mercury required to fill it must be corrected in the following six ways. 1. A volume of (4.0$\pm$0.2) mm^3 must be added to account for the replacement of the expansion volume assembly by the valve atop the resonator. 2. A volume of (1.4$\pm$0.1) mm^3 must be subtracted to account for the mercury intrusion in the gaps between the plugs and the ports on the resonator. 3. The volume of (12.4$\pm$0.1) mm^3 which was determined by acoustic measurements with the coupler must be added to account for the replacement of the plugs by the transducer assemblies. 4. The calculated volume (2.15$\pm$0.41) mm^3 must be subtracted to account for the acoustic effects of the gaps between the transducers and the coupler. 5. The calculated volume (1.31$\pm$0.13) mm^3 must be added to account for the acoustic effects of the gaps between the plugs and the coupler. 6. The calculated volume 0.04 ppm must be added to account for the sagging of the resonator under its own weight. The net correction is (14.2$\pm$0.5) mm^3 out of 2943 cm^3.

7. Determination of M/γ_0

Our determination of M/γ_0 is ultimately based on a sample of nearly monoisotopic Ar^{40} especially manufactured and analyzed for the present determination of R. We removed the chemically reactive impurities from this sample and measured the relative abundances of the remaining noble gas impurities sufficiently well to establish M for this sample within 0.7 ppm. As discussed below, we assumed $\gamma_0 \equiv 5/3$ for this sample. A series of acoustic resonance frequency measurements was used to compare the standard sample to the working sample of argon (which was actually used for the determination of R). This series was optimized to determine the ratio of the speeds of sound between the two gases and it established M/γ_0 of the working sample with a total inaccuracy of 0.8 ppm, as indicated in table 8.

Table 8. Values of M/γ_0 for various gases

Gas	M/γ_0 in g/mol
Ar-40 (standard, purified >26 h)	23.97751_1 ($\pm$0.7 ppm)
Ar-M (working, commercial)	23.96868_4 ($\pm$0.8 ppm)
Ar-A (commercial)	23.96867_0 ($\pm$0.8 ppm)
Ar-commercial, from Nier[a]	23.96867 ($\pm$2.0 ppm)
Ar-commercial, from Nier[b]	23.96865 ($\pm$1.9 ppm)

[a] Re-evaluated in this work.
[b] Re-evaluated in reference [1].

We have independently estimated M/γ_0 for the working sample of argon by assuming that it had the same relative isotopic abundance ratios as those measured by Nier in commercially supplied argon. This estimate, also included in table 8, has a precision of 2.0 ppm and is in agreement with the value of M/γ_0 we obtained using the nearly monoisotopic Ar^{40}. After we made this estimate, we learned that Cohen and Taylor [1] also reevaluated Nier's data. Their value for M/γ_0 and its error are the last entries in table 8. Cohen and Taylor's conclusions are consistent with our own.

We had intended to redetermine R using both argon and helium samples; however, progressive contamination of the helium within the resonator prevented us from making reliable measurements. Common impurities (such as air and water) change the speed of sound in helium 10–30 times more than they change the speed of sound in argon. Thus the contamination that interfered with the helium measurements did not affect the argon measurements.

In this section, we shall describe the sources and analysis of the gases we used, the effects of impurities, the determination of the speed of sound ratios used to determine M/γ_0 of the working gas, and finally our independent estimate of M/γ_0 using published values of isotopic abundance ratios of argon.

7.1 Chemical Composition of the Gases Used

Information concerning the chemical composition of the gases we used was provided by the manufacturers and will be listed here. This information was supplemented by our analysis of certain gas samples subsequent to their use, particularly for trace amounts of other noble gases.

We have used argon samples from three different sources and helium samples from two different sources. The standard argon sample, denoted Ar-40, was purchased from the Mound Facility of the U.S. Department of Energy, Miamisburg, Ohio, [29] in 1984. This sample of nearly monoisotopic Ar^{40} was prepared for these measurements of R. The supplier provided a detailed report based on mass spectroscopy which showed the following abundances: $Ar^{36}<3$ ppm; Ar^{38}, 30.8 ± 3 ppm; N_2, 12 ± 5 ppm; O_2, 5 ± 2 ppm; CO_2, 4 ± 1.2 ppm; $Kr<6$ ppm; and $Xe<7$ ppm. Here, the error and detection limits are two standard deviations, based on four replicate analyses. As discussed in section 7.2, our measurements of the speed of sound in portions of this sample provided evidence that in May 1987 the gas in the supplier's container included approximately 35 ppm of CO_2, in serious disagreement with the supplier's analysis. In July 1987, the supplier re-analyzed the remaining gas. The analysis showed that the relative abundances of Ar^{36} and Ar^{38} were unchanged and that CO_2 and mass 28 (CO or N_2) impurities were present. Such chemically reactive impurities were removed from this gas prior to its use as a standard by the procedures described below. Thus their presence in the supplier's container did not degrade the accuracy of the redetermination of R.

The working argon sample, denoted Ar-M, was purchased for Matheson Gas Products [29] in 1984. From a lot analysis (lot E30 000 6D8, cylinder 45024T), the supplier provided the following upper bounds for impurities: $N_2<3$ ppm; $O_2<1$ ppm; $H_2O<1$ ppm; and total hydrocarbons <0.5 ppm. A third argon sample, denoted Ar-A, was purchased from Airco Inc. [29] in 1986. The supplier provided an analysis (test number AN28, cylinder number CC-58939) which stated: total impurities <1 ppm, including traces of O_2 and N_2.

One helium sample, denoted He-M, was purchased from Matheson Gas Products [29] in 1985 (Lot No. G55-0158-B1). From a lot analysis, the manufacturer stated that the minimum purity was 99.9999 mole percent. Upper bounds were provided for certain impurities: $O_2<0.1$ ppm; $N_2<0.4$ ppm; $Ar<0.1$ ppm; $CH_4<0.1$ ppm; $CO<0.1$ ppm; $CO_2<0.1$ ppm; and $H_2O<1$ ppm. The second helium sample, denoted He-BM was obtained from the Bureau of Mines Helium Research Center in about 1970 (Cylinder No. 139177) and has an unbroken chain of custody. Portions of this gas had been used to calibrate Burnett *PVT* apparatus. The Bureau of Mines provided the remarkable analysis: H_2, 0.16 ppm; $CH_4<0.005$ ppm; H_2O, 0.5 ppm; Ne, 0.40 ppm; N_2, 0.08 ppm; O_2, 0.01 ppm; $Ar<0.005$ ppm; CO_2, 0.03 ppm.

Gas chromatographic analyses of three gas samples were conducted with the help of Mark Sirinides of the Quality Control Laboratory of Airco Industrial Gases, Riverton, N.J. [29]. Samples of Ar-40 and Ar-M which had been used for acoustic measurements were condensed out of the resonator into cylinders prepared for their storage. Portions of these "used" gases were analyzed in November 1986 with the following results. For Ar-40 we found: Ne, 0.9 ± 0.3 ppm; Kr, 2.2 ± 0.3 ppm; Xe, 1.3 ± 0.3 ppm and N_2, <4.5 ppm. The imprecision in the measurement of the xenon abundance is the largest source of the imprecision in the determination of M/γ_0 for this standard sample. The calibration of the chromatograph for the important xenon analysis was based on two standard mixtures, one prepared by Mr. Sirinides, and a second prepared by us, independently. The comparatively coarse upper bound on any possible N_2 impurity was a consequence of our inability to thoroughly purge the inlet to the chromatograph with the small sample of "used" Ar-40. The chromatographic analysis of Ar-M detected no impurities and established the bounds: $Ne<0.3$ ppm; $Kr<0.3$ ppm; $Xe<0.3$ ppm; and $N_2<2.5$ ppm. The chromatographic analysis of He-M detected no impurities. Two bounds were established for He-M: $Ne<0.3$ ppm and $N_2<1.8$ ppm.

In September 1987, the remaining Ar-40 in its original container was shipped to the Helium Field Operations Facility of the U.S. Bureau of Mines in Amarillo, Texas to be analyzed for possible helium content. This was accomplished with a special mass spectrometer which had been built to redetermine the relative abundance of helium in the atmosphere. [59] The analysis yielded the result (1.5 ± 1.0) parts per billion ^4He in the argon.

7.2 Effects of Impurities and Purification

7.2.1 Effects of Impurities For low densities, the speed of sound in a gas mixture can be estimated from the relation $c_0^2=C_p^0RT/(C_V^0M)$. For mixtures, C_p^0, C_V^0, and M are mole fraction averages of C_p^0,

C_V^0, and M of the components. We have used these relations to calculate the derivative of c_0^2 with respect to mole fraction of various possible chemical impurities. The results for helium and argon, along with the values of γ_0 which were used to calculate C_p^0 and C_V^0, are listed in table 9. From table 9 one can conclude, for example, that 1 ppm of water in helium will decrease c_0^2 by 3.93 ppm and that 1 ppm of water in argon will increase c_0^2 by 0.12 ppm.

Table 9. Sensitivity of c_0^2 to impurities

Impurity	M (g/mol)	γ_0	$\frac{1}{c_0^2}\frac{d(c_0^2)}{dx}$ in He	in Ar
H_2	2	1.4	0.23	0.68
He	4	5/3		0.9
H_2O	18	1.32	−3.93	0.12
Ne	20	5/3	−4.0	0.5
N_2	28	1.4	−6.27	0.03
O_2	32	1.4	−7.3	−0.07
Ar	40	5/3	−9.0	
CO_2	44	1.4	−10.3	−0.37
Kr	84	5/3	−20.0	−1.1
Xe	131	5/3	−31.8	−2.3
Hg	201	5/3	−49.0	−4.0

When the resonator was filled with helium, we measured a slow decrease in the resonance frequencies. In a typical case the decrease was 9.3 ppm/100 h with 438 kPa of He-M in the resonator. In contrast, when the resonator was filled with argon, we never observed a secular change in the frequencies. (In one case, a change of ±0.5 ppm/100 h would have been detected with Ar-M in the resonator at 100 kPa.) We speculate that slow desorption of impurities is responsible for these effects. Possible sources of water etc. are the "Viton" [29] O-rings which seal the microphone ports and the fill port of the resonator. From table 9 it is clear that the speed of sound in helium is much more sensitive to most impurities than the speed of sound in argon. For common impurities, levels below 1 ppm would be disastrous in helium yet they would be barely detectable by speed-of-sound measurements in argon.

One might imagine that a tiny droplet of mercury remained in the resonator after the volume determinations. Such a droplet would have a vapor pressure of 25 mPa near T_t. If mercury were present at this partial pressure in argon under typical measurement conditions (300 kPa) and if it were not accounted for, the resulting value of R would be 0.3 ppm too small. In practice, the speed of sound was fitted to a function of pressure which included a p^{-1} term, primarily to account for the effects of the thermal accommodation length. This term would account for the effect of saturated mercury vapor, if vapor were present.

7.2.2 Apparatus and Procedures for Purification The manifold used for loading the resonator, measuring the pressure, purifying the Ar-40, and collecting samples of gas for analysis, is diagrammed in figure 16. The portion of the manifold which is enclosed by the "Boundary of Bakeout" on figure 16 was made entirely of metal and was baked at temperatures above 100 °C prior to use. The valves used metal bellows for stem seals and the demountable joints were sealed with nickel gaskets. Except for very short transition pieces, the tubing had a diameter of at least 0.95 cm (3/8 inch).

A purification procedure was followed with the Ar-40 used to standardize the Ar-M. The gas to be purified was admitted to a stainless-steel cylinder (10 cm i.d. and 55 cm high) hung from the manifold on a 4 cm i.d. tee. (See fig. 16.) The temperature of one side of the cylinder was increased to 80 °C using a heating tape, in order to force circulation of the gas within it. The side-arm of the tee atop the cylinder opened to a zirconium-aluminum alloy getter (Model GP50, S.A.E.S. Getters Inc. [29]) which was maintained at a temperature near 400 °C. Data provided by the manufacturer of the getter indicated that it is very effective in removing active gases (such as CO, CO_2, O_2, N_2, and H_2) from the noble gases and it is moderately effective in removing hydrocarbons.

In an early test of the purification procedure, about half the impurity (probably CO_2) was removed from an Ar-40 sample at 500 kPa in 28 h. In subsequent use, the getter was maintained at a higher temperature, the convective mixing was improved, and the purification was conducted at pressures of 280 kPa or lower. With these changes, more than 90% of the impurities in an Ar-40 sample were removed in 26 h. This can be seen from table 10: in 26 h the ratio c(Ar-40)/c(Ar-M) changed 90% of the way from its value for unprocessed Ar-40 towards its value for Ar-40 purified for 120 h, or more.

The purification procedure we have described did not change the speed of sound in two Ar-M samples by more than 0.3 ppm.

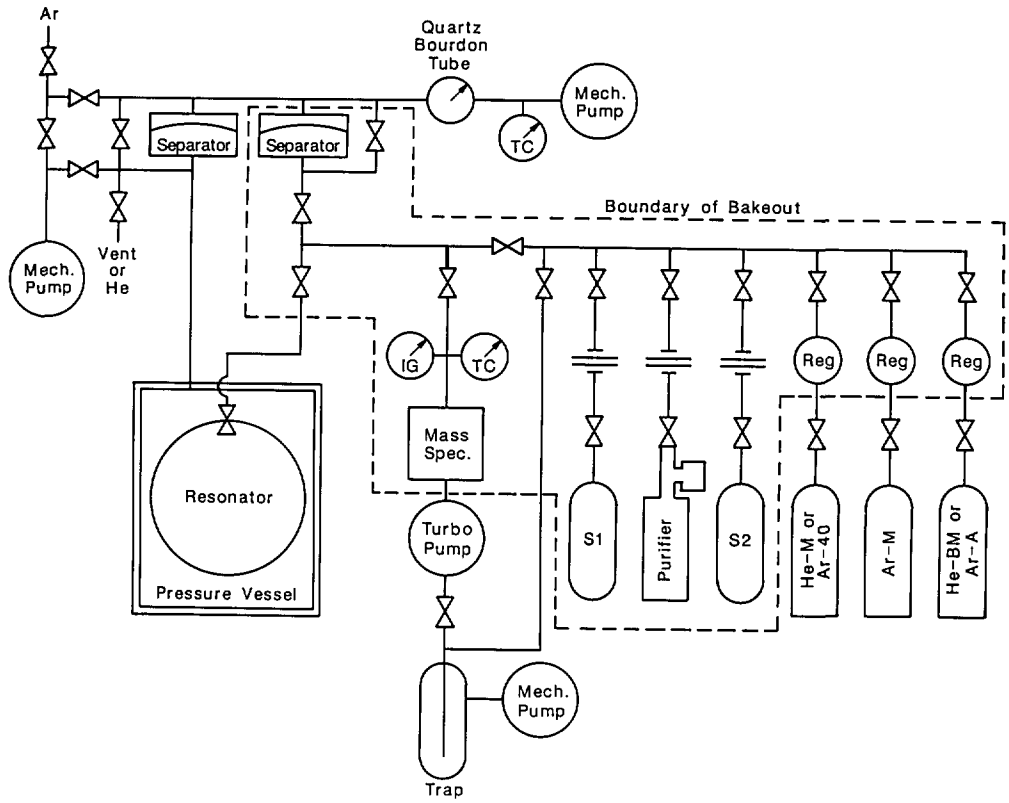

Figure 16. Schematic diagram of gas handling system.

Table 10. Speed of sound ratio determinations

Gas	Comment	$10^6\left(\frac{c(\text{gas})}{c(\text{Ar-M})}-1\right)$	Pressure (kPa)	Date
Ar-A		0.22	115	May 1, 1987
Ar-A		0.27	151	May 2, 1987
Ar-A		0.35	117	May 21, 1987
Ar-40	unprocessed	−191.5[a]	105	May 5, 1987
Ar-40	purified 26 h	−184.63	105	May 4, 1987
Ar-40	purified 120 h	−183.92	131	May 14, 1987
Ar-40	purified 240 h	−184.35	117	May 20, 1987
Ar-40	purified 240 h	−184.00	104	May 22, 1987

[a] The value listed is the mean determined from the (0,2)–(0,6) modes. The rms deviation from the mean for a single ratio was 1.0 ppm for the unprocessed Ar-40 and about 0.1 ppm for all other cases.

The speed of sound in the unprocessed Ar-40 had a measurable dispersion which was eliminated by the purification. Purification for 120 hours increased the speed of sound in Ar-40, as determined from the (0,2)–(0,6) modes at 100 kPa by 9.2, 8.0, 7.5, 7.0, and 6.8 ppm, respectively. Purification also reduced the excess half-widths of the same modes by 2.4, 2.3, 2.0, 1.7, and 1.5 ppm of their respective frequencies.

The dispersion and the excess half-widths in the speed-of-sound data for the unprocessed Ar-40 can be quantitatively interpreted as effects of a relaxing impurity such as CO_2. Simpson et al. [60] determined the relaxation time τ_m of a $(0.1CO_2+0.9Ar)$ mixture. Their results can be applied to other CO_2+Ar mixtures using the mole fraction dependence established by Kneser and Roesler [61]:

$$\frac{1}{\tau_m}=\frac{1-x}{\tau_{Ar}}+\frac{x}{\tau_{CO_2}},$$

with the parameters $\tau_{CO_2}=(8\pm1)$ μs and $\tau_{Ar}=(50\pm10)$ μs at 273 K and 100 kPa, and where x is the mole fraction of CO_2. Consequently, the CO_2 impurity in argon would increase the half-widths by δg where

$$\frac{\delta g}{f}=\frac{2x}{15}\frac{\omega\tau}{1+(\omega\tau)^2}.$$

This formula fits the decreases in the half-widths produced by the purification of Ar-40 with the parameters $\tau_{Ar}=46$ μs and $x=35\times10^{-6}$. These parameters can be used to predict changes in the resonance frequencies with the relation

$$\frac{\delta f}{f}=-\frac{2x}{15}\left[1+\frac{1}{1+(\omega\tau)^2}\right]-\frac{x}{20}.$$

The predicted frequency changes are 9.5, 8.3, 7.6, 7.2, and 7.0 ppm for the (0,2)–(0,6) modes. All are within 0.3 ppm of the measured changes. This agreement and the agreement of the measured relaxation time with the literature value for CO_2 strongly suggested that the unprocessed Ar-40 contained much more CO_2 than indicated in the manufacturer's original analysis.

The study of the purification process and the determination of speed-of-sound ratios discussed in the next section were completed in May 1987. Then, the remaining Ar-40 was returned to the manufacturer in its original stainless-steel container. The manufacturer re-analyzed the gas in July 1987 via mass spectroscopy and reported the following abundances: Ar^{36}, <3 ppm; Ar^{38}, 35 ppm; CO_2, 32±5 ppm; O_2, 7±2 ppm; N_2+CO, 37±15 ppm. As one might expect, the relative abundances of the argon isotopes did not change. The lack of change in O_2 demonstrates that air leakage was not a factor. The manufacturer speculated that CO_2 and CO were being formed in the container by a reaction involving the metal oxide, adsorbed hydrocarbon films, and possibly adsorbed water. In any event, the presence of chemically reactive impurities in the supplier's container does not degrade the accuracy of the re-determination of R because these impurities were removed prior to the determination of the ratios.

7.3 Determination of Speed of Sound Ratios

The last part of the laboratory work in the present determination of R was a series of measurements to determine the ratios of the speeds of sound in Ar-40 and Ar-A samples to the speed of sound in the working gas, Ar-M. The ratio determinations had an imprecision of only 0.2 ppm in c and were used to determine M/γ_0 for the Ar-A and Ar-M samples from the value of M/γ_0 computed for Ar-40 sample.

The speed of sound ratios were obtained from measurements of the acoustic resonance frequencies at temperatures near T_t when the resonator was sucessively filled with an Ar-M sample and another gas sample. The successive fillings were at very nearly the same pressure and temperature. Each pair of fillings and its associated resonance measurements were completed within 4–12 h. These precautions minimized the effects of drifts in the pressure transducers and in the resistance bridge used for temperature measurement. To minimize the effects of imperfections in the resonator's geometry and imperfections in our model of its elastic properties, the speed of sound ratios were obtained from a mode by mode comparison of the resonance frequencies, after application of the usual corrections for the thermal boundary layer, the accommodation length, and the resonator's compliance. (The mass dependence of the transport properties and virial coefficients can be neglected.) Typically these ratios determined from the (0,2)–(0,6) modes had an rms deviation from their mean of 0.1 ppm; thus, the 0.2 ppm error in the ratio determination results from another source, probably the thermometry. The results of the ratio measurements are listed in table 10. The frequencies that were used in the important comparison of Ar-40 to Ar-M are tabulated in Appendix 3. For these ratio determinations only, the frequencies were determined from 6-parameter fits of eq (4.1) to the voltage vs frequency data. Thus, we exploited the fact that 6-parameter fits yielded more precise frequency measurements than 8-parameter fits. Although the 6-parameter fits are influenced by the systematic effects of mode overlap, the mode by mode comparison of frequencies accounts for these effects.

7.4 Determinations of M/γ_0 for the Working Gas

After purification, the Ar-40 sample was a mixture of argon isotopes and other monatomic gases. Thus, neither rotational nor vibrational degrees of freedom need be considered in the calculation of γ_0. The lowest electronic state of argon is 11.7 eV above the ground state. It follows that at T_t and the densities of interest here, electronic contributions

to γ_0 are negligible. Thus we take $\gamma_0=5/3$ for Ar-40. The mole fraction averaged atomic mass is calculated using the isotopic abundances provided by the manufacturer ($Ar^{36}=0\pm3$ ppm; $Ar^{38}=31\pm3$ ppm), the noble gas abundances measured by chromatography, (Ne=0.9±0.3 ppm; Kr=2.2±0.3 ppm; Xe=1.3±0.3 ppm) and the atomic masses from the 1983 atomic mass evaluation [62]. For the present purpose the most important value is 39.9623837 g/mol (±0.035 ppm) for Ar^{40} on the carbon-12 scale. The resulting value of M/γ_0 for the purified Ar-40 sample is 23.97751_0 g/mol with an uncertainty of ±0.7 ppm originating from the uncertainty in the chromatographic measurement of the xenon in the Ar-40.

To calculate M/γ_0 for Ar-M from the value for the Ar-40 sample, we assumed the M/γ_0 varies inversely as the square of the measured speed-of-sound ratio. The measurements were at nonzero pressure; thus we neglected the very small differences in the virial coefficients of the different argon samples. The mean value of the square of the ratio for the Ar-40 samples purified longer than 26 h (table 10) has an rms deviation of 0.4 ppm. This value leads to the $M/\gamma_0=23.96868_1$ g/mol for the working gas with a combined uncertainty of 0.8 ppm.

7.5 Estimating M/γ_0 from Isotopic Abundance Ratios

For the Ar-M and Ar-A samples prepared commercially from liquid air, we can estimate M/γ_0 using Nier's measurements [63] of the relative abundances of the isotopes in argon from liquid air. Nier found slightly less Ar^{36} and Ar^{38} in argon purchased from a commercial supplier than in argon which he obtained by passing air over hot lithium metal. Nier's "weighted grand mean" data for commercial argon yields abundance ratios: $Ar^{36}/Ar^{40}=(3346\pm6)\times10^{-6}$ and $Ar^{38}/Ar^{40}=(630\pm1)\times10^{-6}$. (Here, the errors are Nier's "probable errors" which we take to mean 0.674 standard deviations.) These abundances can be combined with the 1983 atomic masses to obtain an average molecular mass for Nier's commercial argon of 39.947815 g/mol.

We must now address two issues. One is the accuracy to be assigned to Nier's data, and the second is the likelihood that the Ar-M and Ar-A samples had the same relative abundances as Nier's argon. Nier's "probable error" of his "weighted grand mean" propagates into a standard deviation of 0.96 ppm in M, the average molecular mass. Nier used two different mass spectrometers which were calibrated with different standards which he made from isotopically separated samples. Nier's table II and table III provide sufficient data that one can recalculate both the "grand mean" and its standard deviation. We have done so in a manner which makes a more conservative allowance for the few degrees of freedom present. (There are only three measurements of the important abundance ratio Ar^{36}/Ar^{40} with each spectrometer.) On the basis of this recalculation, the most probable value of M is 39.94779 g/mol, 0.6 ppm smaller than Nier's value. On the basis of our calculation, we have enlarged the estimate of the error in M to 2.0 ppm.

We now consider whether or not the Ar-M sample purchased in 1984 and the Ar-A sample purchased in 1986 are equivalent to Nier's argon which was commercially supplied 35 years earlier. Evidence concerning the equivalence of "recent" argon and Nier's argon is provided by abundance ratio measurements made in connection with Quinn, Colclough, and Chandler's [64] 1976 remeasurement of R. The ratio of the abundance of Ar^{36} to the abundance of Ar^{40} was measured for two commercially supplied samples and one sample obtained by chemical removal of the reactive components of air. The abundance ratio was 0.4% and 0.6% smaller for the commercially supplied samples than the ratio for chemically purified argon. (The same abundance ratio for Nier's commercially supplied argon was 1% smaller than the ratio for Nier's chemically purified argon.) We conclude first, that the commercial process for extracting argon from liquid air does indeed change isotopic abundances. (Nier also measured comparable changes in relative isotopic abundances for other gases produced from liquid air.) We also conclude that the 0.5% difference between the two measurements of the abundance ratios is an independent assessment of certain possible errors in Nier's mass spectroscopy. This difference is equivalent to 1.5 ppm in M. Finally, we note that the $(0.2_8\pm0.1_3)$ ppm difference between speed of sound in Ar-A and Ar-M is equivalent to $(0.5_6\pm0.2_6)$ ppm in M. Such a small difference could not have been resolved by Nier's measurements.

In this assessment of M for commercially supplied argon, we have not used the more recent data of Melton et al. [65]. Melton et al. did not use synthesized standards to calibrate their mass spectrometer and they relied, in part, upon Nier's data as evidence that fractionation did not occur within their mass spectrometer's inlet system.

We note that Quinn et al. [64] have interpreted the published data concerning the relative abundances of the isotopes of argon in a quite different way. In particular, they have chosen to rely on the abundance data obtained by Melton et al. [65] with commercially supplied argon and they have accepted the conclusion of Melton et al. that the isotopic compositions of commercially supplied and atmospheric argon are the same. Thus, Quinn et al. adopted a value for M which is 4.8 ppm smaller than the one we have used and they attributed to it an overall uncertainty of 5 ppm.

After we completed this assessment, we learned that Cohen and Taylor [1] also reevaluated Nier's data. Their conclusions concerning the value of M/γ_0 and its error are the last entries in table 8. Cohen and Taylor's conclusions are much closer to our own than those of Quinn et al. [64].

8. The Pressure and Other Thermodynamic and Transport Properties

The "working equation" discussed in sections 2.8 and 2.9 demonstrates that the present determination of R requires measurements of the pressure and values for the thermal diffusivity of the gases; however, these quantities need not be known to nearly the same accuracy as the primary quantities (resonance frequencies, volume, temperature, and M/γ_0). From the information presented below, we conclude that the error in the measurement of the pressure makes a negligible contribution to the error in R. We also conclude that the uncertainty in the value of the thermal conductivity obtained from the literature contributes 0.30 ppm to the error budget for R for the argon data.

We shall also cite expressions for the viscosities of the gases used. The viscosity was useful for comparing the measurements of the half-widths of the acoustic resonances with the theory of the resonator and might have revealed systematic errors.

8.1 Measurement of the Pressure

From the "working equation," one can see that the sensitivity of R to errors in pressure measurements is greatest through the dependence of the speed of sound upon pressure. For argon $(1/c^2)\cdot(\mathrm{d}(c^2)/\mathrm{d}p)=0.002$ MPa^{-1}. It follows that pressure measurements must have an imprecision no greater than 100 Pa to insure that this imprecision contributes no more than 0.2 ppm to the uncertainty in R. This certainly was achieved in the present work. The accuracy required of the pressure measurements is on the order of 200 Pa at 100 kPa and declines at higher pressures. (For helium $(1/c^2)\cdot(\mathrm{d}(c^2)/\mathrm{d}p)=0.01$ MPa^{-1}, a value 5 times larger than for argon. To determine R with helium, the bounds on the allowable imprecision and inaccuracy of the pressure measurements are 5 times smaller than for argon, under corresponding conditions.)

The pressure measurements were made with a fused-quartz-bourdon-tube differential pressure gage. This gage (Model No. 6000-801-1, Ruska Instrument Corporation [29]) uses an optical readout of the bourdon tube's position and a magnetic feedback system. The manufacturer's calibration data indicated that the gage had a full scale range of 1 MPa and was linear to 1 part in 10^5. The reference side of the gage was continuously evacuated by a mechanical vacuum pump. The pressure on the reference side was monitored with a thermocouple-type vacuum gage and was in the range 1–2 Pa. The zero-pressure indication of the gage was found to change by as much as 27 Pa between checks; however, changes were generally much smaller. At the conclusion of all the measurements, the pressure gage was compared with a calibrated barometer. The gage read 6 Pa higher than the barometer.

As indicated in figure 16, the gas in the resonator and the manifold was always separated from the pressure gage by a diaphragm. This arrangement was required when helium was the test gas. (If helium at high pressures were to come in contact with the bourdon tube it would diffuse into the fused quartz and change the calibration in a time-dependent manner.) The separator arrangement was also convenient for preserving the cleanliness of the test gases. The separating diaphragm was a variable capacitance differential pressure transducer (Type 315BD-00100 sensor head with Type 270B electronic display unit, MKS Instruments, Inc. [29]) constructed of stainless-steel and inconel. The full-scale range of this unit was 13 kPa. Between checks, the zero-differential-pressure indication of the separator was found to change by as much as 53 Pa; however the changes were generally much smaller.

The pressure of the test gas was always measured while the valve atop the resonator was being closed. This was always done when the resonator was sufficiently near thermal equilibrium that its temperature could be defined with the accuracy required for the pressure measurements. We discovered that while the valve was being closed the pressure increased, as one might expect, from com-

pressing the bellows stem seal of the valve. A small correction was made for this effect by plotting the indicated pressure as a function of the position of the valve's handle and extrapolating the plot to the closed position.

8.2 Thermal Conductivity and Viscosity of the Gases

An error in the thermal conductivity, λ, of the gas leads to an error in the determination of R through the thermal boundary layer correction. The correction to R varies as λ and is 125 ppm, averaged over the (0,2)–(0,6) modes for argon at 100 kPa. The 0.3% uncertainty in λ led to a 0.30 ppm contribution to the error budget for R when R was determined from the argon data described in the next section. This error propagation was established by numerical experiments in fitting the weighted speed of sound data on the isotherm T_t.

We have used the expression

$$\lambda/(\mathrm{Wm^{-1}K^{-1}})=(1.6382+0.0052\{(T-T_t)/\mathrm{K}\})\times 10^{-2}+216\times 10^{-5}(\rho/\mathrm{kg\cdot m^{-3}})$$

for the thermal conductivity of argon. The zero-density values of the thermal conductivity were obtained from the "HFD-B2" potential by Aziz and Slaman [66]. As discussed by these authors, the thermal conductivity calculated from the potential is in agreement with recent measurements of the thermal conductivity near 300 K, within experimental errors which range from 0.2–0.3%. The same potential is consistent with the dispersion coefficient, spectroscopy, scattering, and bulk data. Our confidence in the derived thermal conductivity is enhanced by the fact that the same potential was used to calculate the viscosity and diffusion coefficients near T_t and these transport properties also agree with direct measurements within experimental errors on the order of 0.3%. The density coefficient of the thermal conductivity of argon is the value tabulated for 27.5 °C by Maitland et al. [67] and is based upon direct measurements. From the same two sources, we have obtained the expression for the viscosity of argon:

$$\eta/(\mathrm{Pa\cdot s})=(2.0973+0.0064\{(T-T_t)/\mathrm{K}\})\times 10^{-5}+1.111\times 10^{-8}(\rho/\mathrm{kg\cdot m^{-3}}).$$

The corresponding expressions for helium are:

$$\lambda/(\mathrm{Wm^{-1}K^{-1}})=(1.4573+0.00368\{(T-T_t)/\mathrm{K}\})\times 10^{-1}+2.91\times 10^{-4}(\rho/\mathrm{kg\cdot m^{-3}})$$

and

$$\eta/(\mathrm{Pa\cdot s})=(1.8638+0.0046\{(T-T_t)/\mathrm{K}\})\times 10^{-5}-1.064\times 10^{-8}(\rho/\mathrm{kg\cdot m^{-3}}).$$

Here, the zero-density values were obtained from reference [68] and the density coefficient was obtained from reference [67].

8.3 Density and Heat Capacity of the Gases

In order to make the correction for the thermal boundary layer, we require the density and heat capacity of the gases as functions of pressure. To obtain the density, we inverted the virial equation of state. To obtain the pressure dependence of the heat capacities, we also used the virial equation to obtain the relations:

$$C_p=\frac{5}{2}\cdot R-T\cdot p\cdot\frac{\mathrm{d}^2B}{\mathrm{d}T^2}$$

$$\gamma=\frac{5}{3}\left(1+2(\gamma-1)\frac{\mathrm{d}B}{\mathrm{d}T}\cdot\frac{p}{R}+(\gamma-1)^2\cdot T\cdot\frac{\mathrm{d}^2B}{\mathrm{d}T^2}\cdot\frac{p}{R}\right).$$

The second virial coefficient, B, and its temperature derivatives were calculated at T_t from the HFD-B2 potential [66] for argon. The results are

$$B/(\mathrm{cm^3\cdot mol^{-1}})=34.25-1.170\times 10^4(\mathrm{K}/T)-9.56\times 10^5(\mathrm{K}/T)^2$$

including the leading quantum corrections. For helium, the expression given by Guildner and Edsinger [69] was used:

$$B/(\mathrm{cm^3\cdot mol^{-1}})=12.00-0.0044\{(T/\mathrm{K})-273.15\}.$$

9. Determination of c_0^2 in the Working Gas

In this section we describe our speed-of-sound measurements and their analysis for the working gas Ar-M along the isotherm at T_t. These measure-

ments were fitted to various models and they established $c_0^2 = A_0 = (94756.17_8 \pm 0.06_5)$ m^2/s^2 for the working gas. The 0.68 ppm imprecision in A_0 from the fit includes the effects of imperfect measurements of the resonance frequencies, random errors in the temperature measurements, and imperfect thermal accommodation between the gas and the shell. The values of A_0 determined from the resonance frequencies of the (0,2)–(0,6) modes, each fitted separately, were consistent, within the precision stated; thus the final value of A_0 is based on an average of the the data for these five modes. At the end of this section, we discuss a possible problem in defining the location of one transducer during the determination of A_0. This possible problem has led us to add an additional error term of 0.59 ppm to table 1, which could have been eliminated if the opportunity to repeat the measurements at T_t were available.

9.1 Preparation of the Resonator

The measurements which determined A_0 were performed during the period of time between the thermometer calibrations of March and April 1986, and thus also lie between the second and third determination of the volume of the spherical resonator.

After the second volume determination, the resonator was carefully cleaned and "baked" for 2 days under vacuum to remove the last traces of mercury. The valve mechanism and transducers were installed. The resonator was mounted in the thermostat and connected to the gas handling system where it was evacuated and "baked" for a further period of 48 h. During this time the resonator was maintained at a temperature of 60 °C (approximately 25 °C below the softening temperature of the vacuum wax in the equatorial joint) while all remaining components accessible to the experimental gases were maintained at or above 100 °C. Residual gases in the vacuum system were monitored using the ionization gage and mass spectrometer. Initially, a considerable number of impurities with mass numbers up to 200 were evident and these could be traced, by closing valves, mainly to the resonator. We suspect that heavy hydrocarbon impurities were evolved from the wax joint at the elevated temperature. Towards the end of the bakeout all the high-mass impurity peaks showed considerable reduction and when the system was cooled down to T_t the total pressure reading fell from about 0.5 mPa to below 4 μPa. At the same time almost all of the remaining peaks in the mass spectrum disappeared leaving resolvable peaks at $m/e = 1$, 12, 14, 16, 17, 18, 19, 28, and 44 amu/e only. Of these, hydrogen had a relative intensity of 111, mass numbers 19 and 28 had intensity 10, and all others less than 3. Finally, the resonator and gas handling system were flushed with the working gas, Ar-M, up to a maximum pressure of 500 kPa (venting through the vacuum pumps) before filling with Ar-M for the first set of measurements.

9.2 Speed of Sound Measurements

The measurements considered in this section were performed in three separate runs. The first started at a pressure near 500 kPa and proceeded to lower pressures in steps of approximately 100 kPa; the second commenced at 450 kPa and continued down to 50 kPa in decrements of 100 kPa; and, the third started near 100 kPa and ended near 25 kPa with decrements of 25 kPa. At each point on the isotherm, the resonator was allowed to approach to within a few millikelvins of the thermal steady state before the pressure was measured and the valve atop the resonator closed. A further period of time was then allowed for the thermal transient caused by this operation to decay before the measurements proceeded. In every case, the steady-state temperature was within approximately 5 mK of T_t and was stable to better than 0.4 mK (typically 0.2 mK) during the period of about 45 min required to measure a complete set of resonance frequencies. The temperatures reported here are always the mean of those measured at the north and south poles (for the present measurements these correspond to thermometers #835B and #1888002, respectively). Frequency measurements were performed on the lowest six radial modes starting with (0,2) and working up to (0,7); they were then repeated in reverse order, finally ending with (0,2). (As discussed in sec. 4.3.1, the data for the (0,7) mode were omitted from the analysis, because they overlapped with the (13,2) mode.) During the frequency measurements for each mode, the resistances of both thermometers were measured so that every resonance frequency is associated with a unique determination of the mean temperature. At the completion of such a set, the valve between the resonator and the gas-handling system was opened and the pressure measurement was checked. Because the external pipework was not thermostatted, small changes (up to 50 Pa) were observed; however, they were inconsequential. The pressure was then reduced by pumping gas out through the vacuum system, and the temperature of the resonator

(which fell by adiabatic cooling during the expansion) was restored as close as possible to T_t by supplying power to the equatorial heaters. After about 2 h the system again attained a steady state and was ready for the next point on the isotherm.

9.3 Speed of Sound Results

In Appendix 1 we list the measured resonance frequencies and half-widths, together with the corresponding averages of the polar temperatures, for each pressure studied. Appendix 1 includes two measurements of frequency and half-width for each of six modes at each of 14 pressures for a total of 168 frequencies and 168 half-widths. Speeds of sound at T_t and the experimental pressures were obtained from these data as follows. First the data for the (0,7) mode were discarded because of the mode overlap problem discussed in section 4.3.4. The resonance frequencies for the (0,2) mode were multiplied by the factor $1+0.7\times10^{-6}$ to correct for the shape perturbation resulting from the unequal diameters of the hemispheres, as mentioned in section 3.4. Then, all the resonance frequencies were corrected for the thermal boundary layer using eq (2.32) and for coupling of gas and shell motion using eqs (2.20) and (2.22), as well as the transport and equilibrium properties from sections 8.2 and 8.3. The thermal boundary layer correction requires a value for the thermal accommodation coefficient h in eq (2.24). At this point in the analysis (and in Appendix 2) we assumed $h\equiv1$; however, this assumption is relaxed below. The corresponding speeds of sound at the experimental temperatures and pressures were then obtained using the volume of the spherical cavity (at the temperature and pressure of the measurement) given in section 6.1 and, finally, these speeds were corrected with negligible additional uncertainty to exactly T_t according to

$$c^2(T_t,p)=(T_t/T)\,c^2(T,p). \tag{9.1}$$

The corrected values for the speed of sound in Ar-M at T_t are listed in Appendix 2.

9.4 Analytical Representations of the Speed of Sound

We have chosen to fit the speed of sound to the physically motivated expression

$$V^{2/3}(f_{0,n}/\nu_{0,n})^2_{\rm corr}-A_3p^3=$$

$$c^2-A_3p^3=A_0+A_1p+A_2p^2+A_{-1}p^{-1} \tag{9.2}$$

from which we obtain A_0 for Ar-M at T_t and ultimately the value of R. In using eq (9.2), we have assumed $A_3=1.45\times10^{-18}$ m^2·s^{-2}·Pa^{-3}, the value obtained by Goodwin [28] from speed of sound data at pressures up to 7 MPa where this term contributes 500 ppm to c^2. (The best value of A_3 is 1.2×10^{-18} m^{2}s^{-2}Pa^{-3} if Goodwin's data are fit subject to the constraint that A_1 and A_2 equal the values we report in table 11.) In any case, the contribution of A_3 to the fit to our data is so small that we could have assumed $A_3\equiv0$. If we had done so, A_0 and R would have been increased by 0.42 ppm which is only 0.6 of the standard deviation of A_0 and only 0.25 of the standard error in R.

Equation (9.2) was fit to the data using the least squares procedures published by Bevington [70]. Before fitting, the two values of c^2 derived at a given pressure from a given radial mode were averaged yielding a total of 70 observations corresponding to the lowest five radial modes at the 14 pressures studied. Each observation was weighted inversely by the square of its estimated standard deviation which was taken to be the sum of two terms added in quadrature. The first term, $1.414\times10^{-7}c^2(1+(10^5\ \text{Pa}/p)^2(6\ \text{kHz}/f_{0,n})^2)$, is an estimate for the errors in frequency measurements from eq (4.2). The second term in the estimated standard deviation is $3.7\times10^{-7}c^2$. It was chosen such that $\chi^2=1$ for a "good" fit as judged by deviation plots. If the second term were entirely the result of random errors in the measurement of temperature on the time scale of 4–8 h, it would correspond to a temperature error of 0.1 mK, which is consistent with the experimental procedures.

Table 11. Results of fits to speed-of-sound isotherm at T_t

Parameter/Unit	1	2
A_0/m^{2}s^{-2}	94756.178±0.065	94756.234±0.023
10^4A_1/m^{2}s^{-2}Pa^{-1}	2.2502±0.0035	2.2476±0.0019
$10^{11}A_2$/m^{2}s^{-2}Pa^{-2}	5.321±0.062	5.357±0.034
$10^{-3}A_{-1}$/m^{2}s^{-2}Pa	2.7±2.9	0
χ^2	1.30	1.30

The fitted coefficients for eq (9.2) and their errors are listed in table 11, column 1. In each case, the error quoted is the diagonal element of the error matrix multiplied by the square root of χ^2 divided by the number of degrees of freedom. In figure 17, we show fractional deviations of c^2 for

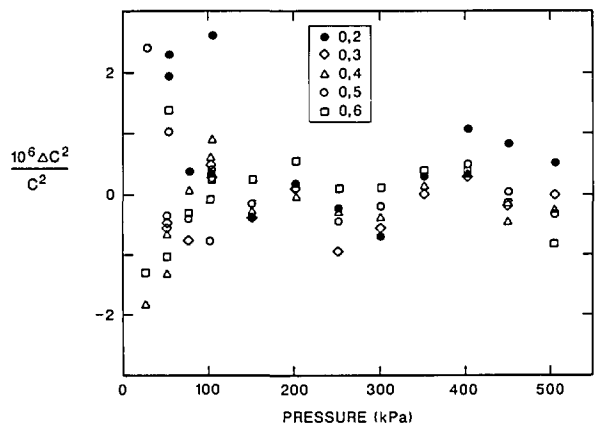

Figure 17. Fractional deviations of 70 observations of c^2 from eq (9.2) with the parameters from column 1 of table 11. (Δc^2=observed c^2−calculated c^2.) The symbols used to identify the various modes are indicated in the inset.

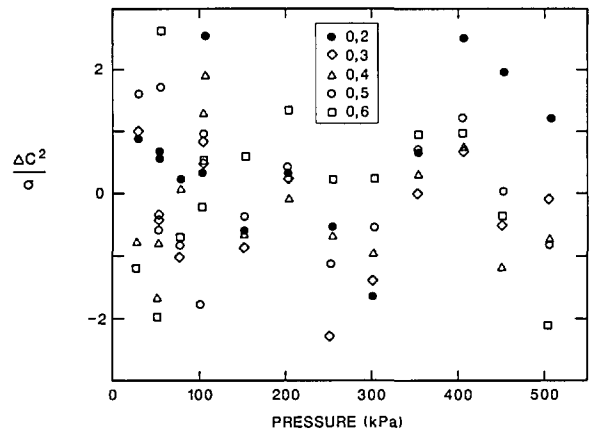

Figure 18. Deviations of 70 observations of c^2 from eq (9.2) with the parameters from column 1 of table 11, in units of the pressure- and frequency-dependent standard deviation calculated in section 9.4. (Δc^2=observed c^2−calculated c^2.) The symbols used to identify the various modes are indicated in the inset.

each mode from the fit. All but 13 of the 70 observations deviate by less than 1 ppm and 11 of these 13 are in the narrow region below 100 kPa where the signal-to-noise ratio is reduced. In figure 18 the deviations from the same fit are shown, now scaled by the pressure- and frequency-dependent standard deviation in the speed of sound. All 70 data fall within 2.6 standard deviations of the fit. There are no obvious trends in the deviations with pressure or frequency. The fit establishes A_0 (c_0^2 in table 1) with an imprecision of 0.68 ppm. This small imprecision is a direct consequence of the narrowness of radially symmetric resonances and the high signal-to-noise ratio obtained with the spherical resonator.

9.5 Discussion of the Isotherm Parameters A_{-1}, A_1, and A_2

If the parameter A_{-1} is interpreted as arising solely from imperfect thermal accommodation, (and not from an impurity of fixed partial pressure) its value in column 1 is equivalent to an accommodation coefficient $h=0.93\pm0.07$. This value is consistent with the value $h=0.84\pm0.05$ obtained by Ewing, McGlashan, and Trusler [10] in studies of argon in an aluminum resonator at pressures ranging from 15–248 kPa. Shields and Faugh also report that thermal accommodation between heavy molecules and machined metal surfaces is very efficient [22].

We have used the value $h=0.93$ (obtained from the value of A_{-1} in table 11, column 1) to redetermine c^2 from the resonance frequencies and then refit eq (9.2) to the revised values of c^2. In doing so, we have relaxed the assumption $h\equiv1$ made above. The changes in A_0, A_1, and A_2 were negligible.

If the speed-of-sound data are fitted with the constraint $A_{-1}\equiv0$, (or, equivalently, the accommodation coefficient is constrained to be exactly 1) then A_0 is increased by 0.59 ppm and χ^2 is increased by 0.2%. (Table 11, column 2.) As expected, this constraint greatly reduces the correlation between the remaining parameters; thus, statistical measures of their imprecision are much smaller; however, there is no a priori reason for assuming A_{-1} is exactly 0.

Before comparing the value of A_1 with independent values, we mention two sources of systematic error in this parameter. First, in section 3.8 it was shown that uncertainty in the shell's compliance ($\pm6\%$) contributed an uncertainty of $\pm0.09\%$ in A_1. Second, we have not corrected the data for the compliance of the transducers. We now argue that this correction increases A_1 by 0.13% and the systematic error in this correction is much smaller than $\pm0.13\%$ of A_1.

We used the value 1.1×10^{-10} m·Pa^{-1} for the transducers' compliance in argon at T_t throughout the pressure range 25–500 kPa. This compliance reduces the resonance frequencies by 0.83 ppm at 500 kPa and proportionately less at lower pressures.

This value of the compliance is based on information provided by the manufacturer [31] and is correct when the transducers are in air at 20 °C and 100 kPa and are used at frequencies well below their resonance at 40 kHz. Under these conditions the air inside the transducers provides only 10% of their stiffness; the tension in their diaphragms provides the rest. Thus, replacing the air by argon and reducing the pressure below 100 kPa has little effect on the compliance. Increasing the pressure of the air from 100 kPa to 500 kPa reduces the compliance by 30% [31]. We neglect these effects, thereby introducing a systematic error in the compliance which is a fraction of the compliance. Our estimate of the compliance of the transducers is equivalent to 9.5% of the static compliance of the shell. We corrected the data in Appendix 1 for this additional compliance, recalculated the speed of sound from each frequency, and repeated the fit of eq (9.2) to the data. As expected c_0^2 was unchanged; A_1 was increased by 0.13% to $(2.2533\pm0.0035)\times10^{-4}$ $m^2\cdot s^{-2}Pa^{-1}$. The changes in A_2 and A_{-1} were negligible. For comparison with other work we shall use this corrected value of A_1 and we shall enlarge the estimate of its standard error to 0.19%. The standard error was calculated adding in quadrature the standard deviation of A_1 from the fit (0.16%), the effect of the uncertainty in the shell's compliance (0.09%), and 1/3 of the effect of the transducers' compliance (0.04%). We note that all previous determinations of A_1 from acoustic resonances were influenced by the compliances of the resonators and the transducers; however, the consequences of these compliances were usually ignored.

Several independent determinations of A_1 exist and these may be compared by considering the, perhaps more familiar, second acoustic virial coefficient $\beta_a=(M/\gamma_0)A_1$. Firstly there are direct acoustic measurements, secondly estimates based on the volumetric second virial coefficient B, using

$$\beta_a=2B+\frac{4}{3}T\frac{dB}{dT}+\frac{4}{15}T^2\frac{d^2B}{dT^2}, \tag{9.3}$$

and finally calculations of β_a based on intermolecular pair potentials $U(r)$ and

$$\beta_a=4\pi N_A\int_0^\infty[1-\{1+\frac{2}{5}(U/kT)+\frac{2}{15}(U/kT)^2\}\exp(-U/kT)]\,r^2dr. \tag{9.4}$$

(N_A is Avogadro's constant.) In the first category, the results of Colclough et al. [13] yield $\beta_a=(4.84\pm0.07)$ $cm^3\cdot mol^{-1}$, while the precise measurements of Ewing et al. [10] using a spherical resonator at pressures up to 250 kPa give $\beta_a=(5.24\pm0.06)$ $cm^3\cdot mol^{-1}$. The difference between the present value $\beta_a=(5.401\pm0.010)$ $cm^3\cdot mol^{-1}$ and that of Ewing et al. [10] is about twice the combined standard deviation but nevertheless still remarkably small.

Estimates of β_a from (p, V_m, T) measurements were obtained by Rowlinson and Tildesley [71] and range from 4.9_6 $cm^3\cdot mol^{-1}$ to 5.9_9 $cm^3\cdot mol^{-1}$, encompassing the present result.

We have calculated β_a from eq (9.4) using the most recent determination of $U(r)$ (the HFD-B2 function of Aziz and Slaman [66]) and also, for purposes of comparison, an earlier determination (the HFD-C function [72]). Contrary to the assertion of Rowlinson and Tildesly [71], we find that the leading quantum correction to β_a makes a small but significant contribution (0.16 $cm^3\cdot mol^{-1}$) at T_t. Accordingly, we have combined this term with the results obtained with eq (9.3) to give $\beta_a=5.15$ $cm^3\cdot mol^{-1}$ from the HFD-B2 and $\beta_a=5.51$ $cm^3\cdot mol^{-1}$ from the HFD-C. The uncertainty associated with these values is difficult to assess but must be on the order of the difference between them since the differences between the functions themselves are slight. We regard the agreement with our value as excellent.

Clearly, these independent estimates of β_a for argon at T_t are in close agreement by the standards of the most precise measurements of virial coefficients and all lie close to our determination. Nevertheless, the differences among the values corresponds to about 25 ppm in c^2 at the lowest pressure of our experiment.

Our data constitute the most precise set ever obtained for c^2 in argon at T_t and pressures up to 500 kPa; thus we must look to measurements at higher pressures for a value of A_2 of comparable precision. We considered the measurements of Colclough et al. [13] which extend up to 1.3 MPa and yield $A_2=(6.96\pm0.37)\times10^{-11}$ $m^2\cdot s^{-2}\cdot Pa^{-2}$. Unfortunately, we find this value to be inconsistent with our data as shown in figure 19. Here the dashed curve represents the function obtained when A_0, A_1, and A_{-1} were fit to the 70 observations, with A_2 constrained to be the value of Colclough et al. The deviations are large compared with our imprecision. We note that two groups (Colclough et al. [13] and Ewing et al. [10]) obtained values of A_2

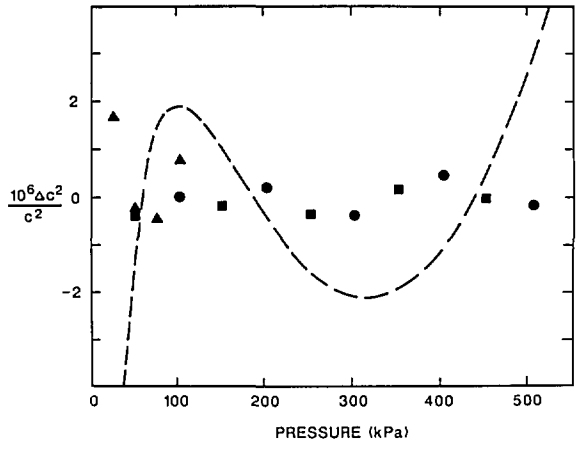

Figure 19. Fractional deviations $\Delta c^2/c^2$ of c^2 from eq (9.2) with the parameters from column 1 of table 11. The 14 points represent the deviations of the mean value of c^2 computed for the five modes at each of the 14 pressures. Each of the three runs mentioned in section 9.2 is distinguished by a different symbol. The dashed curve represents eq (9.2) with the parameters which best fit the data, except for A_2 which was constrained to be 6.96×10^{-11} $m^2s^{-2}Pa^{-2}$, the value obtained in reference [13].

that are greater than the present value and values of A_1 that are smaller. Perhaps these differences are correlated to some degree. Note added in proof: The same isotherm from which we obtained A_3 yields $\beta_a=(5.464\pm0.008)$ cm^3 mol^{-1} and $A_2=(5.084\pm0.014)\times10^{-11}$ m^2s^{-2} Pa^{-2}. This isotherm [28] extending to 7 MPa had less correlation between terms and is closer to ours.

Previous measurements of A_1 and A_2 are not accurate enough to use in extrapolating our measurements to the limit $p=0$ without significant loss of accuracy in A_0. Furthermore, one must assume that the accommodation coefficient is an apparatus-dependent parameter; thus the parameter A_{-1} must also be fit to our data. We conclude that fitting eq (9.2) to the data in Appendix 2 is the best method of determining A_0.

9.6 Possible Transducer Location Problem

In the early sections of this manuscript, we have discussed three factors increasing the inaccuracy of A_0 beyond the 0.68 ppm imprecision resulting from the fit to the isotherm. These factors were the uncertainty in the volume, the uncertainty in the thermal boundary layer correction arising from the uncertainty in the transport properties, and the errors in temperature measurements. The contributions to these items to the error budget appear in table 1. We now consider another possible source of systematic error which appears in table 1 as "possible error in location of transducers."

Upon disassembly of the apparatus after the speed-of-sound measurements at T_t and just prior to the final volume determination, we found that a bolt used to hold one of the transducer assemblies in the shell was binding. (The bolt was too long for the blind tapped hole.) The binding may have prevented the transducer assembly from seating correctly in place, with a possible error in the volume of the cavity. Mechanical measurements on its location were difficult (in the absence of a proper reference plane) and ambiguous at the level of 1 ppm. Accordingly, after the third volume determination in April 1986, the carefully cleaned resonator was reconfigured for acoustic measurements with the transducers correctly installed. Because of the possibility of a volume change occurring as a result of heating, the resonator was "baked" at only 35 °C (the remainder of the system was baked as before). Six sets of measurements on three different samples of Ar-M (taken directly from the cylinder) were obtained near T_t and 100 kPa. For each set, the mean value of c^2 was computed from data for the (0,2) through (0,6) modes weighted according to eq (4.2). The results are given in table 12 together with the fractional deviations of c^2 from the four-term fit to eq (9.2). Also shown in table 12 are the results of the two sets of measurements near 100 kPa which were part of the isotherm at T_t used in the fit to eq (9.2). With one exception, the data after re-seating the transducer are within 1 ppm of the data used to fit eq (9.2). The average difference between the sets of data is 0.59 ± 0.76 ppm, or about 0.87 standard deviation of A_0. (If the first line of table 12 were omitted, the difference would be 0.34 ± 0.45 ppm.) We conclude that the error in the volume, if any, is within the imprecision of our measurements and neglect it. However, we include a contribution of 0.59 ppm in the estimated uncertainty of R arising from this problem.

Table 12. Measurements of the speed of sound in Ar-M at T_t near 100 kPa

$c^2/(m/s)^2-94779$	p/kPa	Date	$10^6(c^2-c^2_{calc})/c^2$
Transducers correctly installed			
0.869	101.85	May 8, 1986	2.04
0.573	101.29	May 8, 1986	0.30
0.572	101.29	May 9, 1986	0.28
0.842	102.25	May 9, 1986	0.74
0.839	102.25	May 10, 1986	0.71
0.833	102.25	May 11, 1986	0.56
Transducer position uncertain			
0.293	100.26	Mar. 30, 1986	−0.10
0.607	101.37	Apr. 4, 1986	0.46

10. Other Tests for Systematic Errors

The present determination of R requires an understanding of the behavior of a spherical acoustic resonator to a degree which has not been demonstrated heretofore. Thus, any indication of possible systematic errors is relevant to evaluating the spherical resonator method. In this section we shall report the differences between the experimental and theoretical values for the half-widths of the acoustic resonances. At the lowest pressures, this measure of our incomplete understanding of the present spherical resonator approaches zero. In the range of the measurements it is smaller than, but comparable to, the uncertainty in A_0 discussed in the preceding section. We shall also mention small internal inconsistencies of the resonance frequencies measured with helium in the shell. They do not indicate important systematic errors in the acoustic model.

10.1 Excess Half-Widths

The half-widths of the resonances are calculated without fitted parameters from eq (2.32) using the transport properties listed in section 8.2. The excess half-width, Δg, is defined as the amount by which a measured half-width exceeds the calculated half-width. Figure 20 displays Δg for measurements in Ar-M at T_t as a fraction of the measured frequency in parts per million. At low pressures, the $\Delta g/f$ of the (0,7) mode increases sharply as a result of the overlap of this mode with the neighboring (13,2) mode. For the other modes which were used in the determination of A_0, $\Delta g/f$ decreases with decreasing pressure and appears to approach 1 ppm near zero pressure. To prepare figure 20, we used the same 8-parameter fits of eq (4.1) to the detector-amplitude vs frequency data which we used to determine the speed of sound and A_0. If we had used 6-parameter fits, $\Delta g/f$ would be 0.5–1 ppm smaller for almost all the data displayed in figure 20. We have no explanation for the differing results with the differing fitting procedures and we did not encounter this difference when helium was in the resonator.

Figure 21 displays the $\Delta g/f$ for five modes with helium in the resonator. The excess half-width of the (0,3) mode is not displayed; it varies from 5–17 ppm over the 75–1003 kPa pressure range studied. These unusually large values of Δg for the (0,3) mode undoubtedly occur because the (0,3) resonance in helium at T_t is at 13.4 kHz, in accidental coincidence with the frequency of the breathing resonance of the shell.

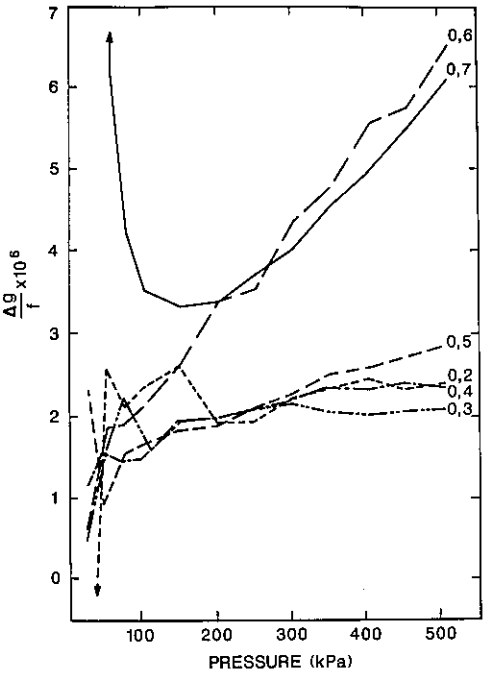

Figure 20. Excess half-widths of $(0,n)$ resonances with argon in the resonator scaled by 10^6/frequency. Δg = measured g minus calculated g.

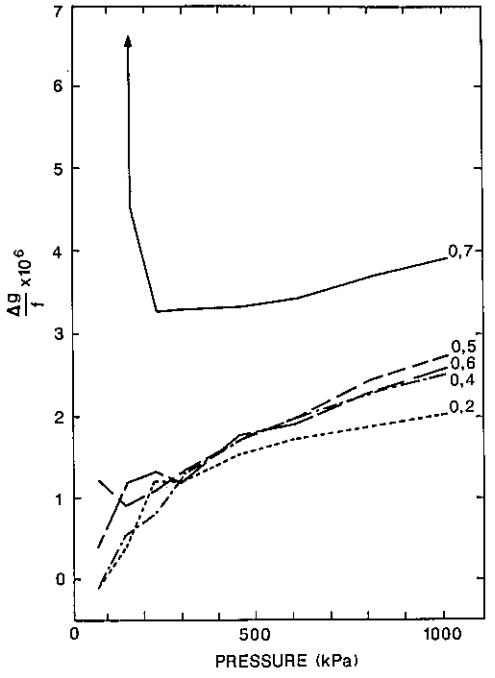

Figure 21. Excess half-widths of $(0,n)$ resonances with helium in the resonator scaled by 10^6/frequency. Δg = measured g minus calculated g.

The similarity of figure 20 to figure 21 is particularly striking upon recalling that the resonance frequencies are 3.162 times higher with helium than with argon. As for argon, $\Delta g/f$ of the (0,7) mode in helium increases sharply at low pressures and is consistent with our interpretation of this effect as being a result of the overlap with the (13,2) mode. As for the argon data shown in figure 20, $\Delta g/f$ of the well separated modes in helium decreases with decreasing pressure and never exceeds 3 ppm. In contrast with argon, $\Delta g/f$ for helium is the same for 6-parameter and 8-parameter fits to data for each resonance.

In figure 22, we have replotted $\Delta g/f$ scaled by $10^6/gf$ and omitted the data for the (0,7) mode. It is encouraging that as the pressure is reduced, $\Delta g/f$ clearly approaches zero for both gases. We have no explanation for the pressure and frequency dependences of Δg. These dependences are not consistent with the addition of a phenomenological damping term to the equation of motion for the shell or with a model for the acoustic radiation from the outer surface of the shell into the surrounding gas (which was nearly the same as the gas within the shell [9]).

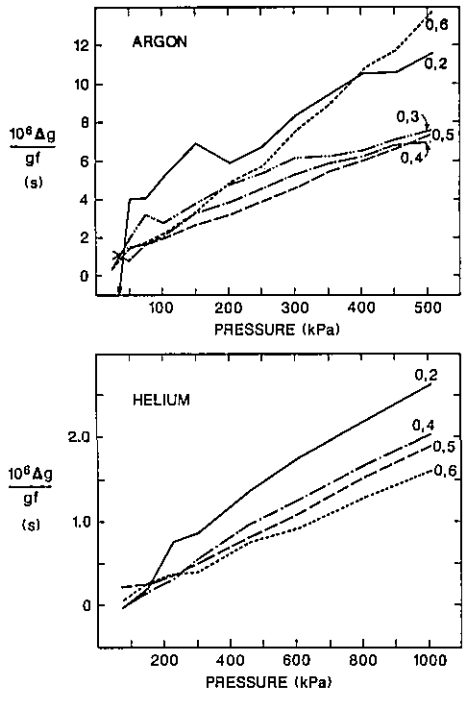

Figure 22. Excess half-widths of $(0,n)$ resonances with argon (top) and helium (bottom) in the resonator scaled by $10^6/$(frequency × half-width). Δg = measured g minus calculated g.

We interpret the fact that Δg does approach zero for both gases as providing an important check of the boundary layer correction to the resonance frequencies. If either the acoustic model or the thermal conductivities were seriously in error, Δg would not be small. The same model and data are used in the calculation of the thermal boundary layer correction; thus, we believe that the calculation has firm experimental support.

10.2 Acoustic Resonances in Helium

We have mentioned that the acoustic measurements with helium in the shell showed evidence of progressive contamination which made them unsuitable for the most accurate determination of R. The contamination rate was sufficiently low that *relative* frequency measurements could be used to test the understanding of the resonator's performance at higher frequencies which straddle the breathing mode of the shell near 13 kHz. As the pressure was decreased from 1.0 MPa to 0.22 MPa, the rms deviation of c^2 from its mean (as derived from the (0,2), (0,4), (0,5), and (0,6) modes) decreased from 2.4 ppm to 1.5 ppm, depending rather sensitively on the frequency used in the model of the breathing mode of the shell. The deviations were systematic. For example, the (0,6) mode consistently yielded values of c^2 which were 2–3 ppm higher than the values of c^2 from the (0,2) mode. We do not consider these systematic deviations to be a cause for concern. They were only 1/10 as large as the frequency shifts caused by contamination and probably indicate dispersion in the contaminated helium as well as failure of the simple, one-breathing-mode model of the shell's elastic response at high frequencies, where the shell has many modes of vibration [7].

11. Summary

We have measured the volume of a spherical resonator at the temperature T_t by weighing the mercury required to fill it. The result was (2943.1524 ± 0.0036) cm^3. Upon converting this volume from the weighing configuration to that used for acoustic measurements, the volume was increased by (0.0108 ± 0.0005) cm^3. The total uncertainty in the volume of 1.22 ppm includes all known systematic and random effects and it contributes just 0.80 ppm to the uncertainty in the redetermination of R. The compliance of the resonator was studied by the application of internal

pressure when it was filled with mercury, by acoustically measuring the volume change upon reduction of external pressure, and by measuring some of the resonant frequencies of the shell. This well characterized spherical resonator was used to measure the pressure dependence of the speed of sound at the temperature T_t in the working gas, a commercially supplied sample of argon. The speed-of-sound data were fitted and extrapolated to zero pressure, thus determining $A_0=(94756.178\pm0.065)$ m^2s^{-2} at T_t for the working gas. The error of 0.95 ppm includes a random component of 0.68 ppm from fitting the isotherm and a systematic component of 0.59 ppm from a possible problem in determining the location of the transducers during the measurements. An additional systematic uncertainty of 0.30 ppm results from the uncertain thermal conductivity's effects on the correction to the measured resonance frequencies for the thermal boundary layer. The temperature of the speed-of-sound measurements is subject to possible systematic errors from calibration and from temperature gradients in the resonator. This contributes terms of 0.8 ppm and 0.4 ppm to the standard error in R. The heat capacity ratio at zero pressure, γ_0, was taken to be exactly 5/3 for all of the argon samples used. The molar mass of the working gas was determined by comparing it to a special lot of argon whose chemical and isotopic composition was defined well enough to determine M to 0.7 ppm. The comparison used a series of extremely precise speed-of-sound ratio measurements at T_t and p_0. The comparison showed that $M/\gamma_0=(23.968684\pm0.000019)$g/mol for the working gas. Most of the 0.8 ppm uncertainty in M/γ_0 came from gas chromatographic measurements of noble gas impurities in the special lot of argon. These results were combined to re-determine the universal gas constant $R=(8.314471\pm0.000014)$ $J\cdot mol^{-1}\cdot K^{-1}$ with an uncertainty of 1.7 ppm.

We now consider an alternative statement of the uncertainty in the present redetermination of R. The form of the statement was inspired by an anecdote repeated by Dr. H. Ku, a statistician retired from NBS. Ku's remarks at a "Round-table discussion on statement of data and errors," [73] include:

"...In the 1930's, C. H. Meyers et al. conducted an elaborate experiment to determine the specific heat of ammonia. After several years of hard work, they completed the experiment and wrote a paper reporting their results. Toward the end of their paper, Meyers declared: "We think our reported value is good to 1 part in 10000: we are willing to bet our own money at even odds that it is correct to 2 parts in 10000. Furthermore, if by any chance our value is shown to be in error by more than 1 part in 1000, we are prepared to eat the apparatus and drink the ammonia."

Paraphrasing Meyers, we are willing to bet our own money at even odds that our reported value is correct to 5 parts in 10^6, and if by any chance our value is shown to be in error by more than 10 parts in 10^6, we are prepared to eat the apparatus, drink the mercury, and breathe the argon!

Acknowledgments

One of us (JPMT) gratefully acknowledges the award of a Lindemann Fellowship which made participation in this research possible.

Numerous individuals contributed to the success of this research. Ralph Hudson presented the challenges of improving the measurement of R, while he was Chief of the Heat Division of NBS. Meyer Waxman participated in the earliest phases of this research. Martin Greenspan was a collaborator in the development of the spherical resonator method of measuring the speed of sound and he has been a source of continuing inspiration. NBS Director Ernest Ambler and Deputy Director Raymond Kammer had the foresight to recognize the power of the method and provided stable support for a number of years. Within NBS, Harry Davis fabricated much of the apparatus used and provided advice in the fabrication of the rest. George Furukawa provided advice and a triple point cell for temperature calibration. Graham Morrison provided many useful suggestions and was particularly helpful in designing the chromatographic analysis. Lynus Barnes had custody of the mercury which Cook had standardized and permitted us to use 4 liters of it. William Reed lent us a balance. R. E. Ellefson and W. J. Roos of the Mound Facility of the U.S. Department of Energy prepared the isotopically enriched argon sample and a mass spectroscopic analysis of it. Mark Sirinides of Airco Industrial Gases collaborated in the actual chromatographic analysis. Phillip Holland of the Helium Field Operations of the Bureau of Mines measured the helium content of our argon standard. David Prowse and James Patterson of CSIRO, Australia compared the density of the mercury we used with a sample of their mercury which also had been standardized by Cook. Ronald Aziz of the Univ. of Waterloo, Canada provided us

with values of the transport properties of helium and argon, prior to their publication. Anthony Goodwin of University College, London provided us with his value of A_3 prior to its publication.

About the authors: Michael Moldover is a senior physicist in the Thermophysics Division of the NBS Center for Chemical Engineering. Martin Trusler, a guest scientist at NBS from the Chemistry Department of University College London, was a Lindemann Fellow during his participation in this project. His current address is: Department of Chemistry, University College London, 20 Gordon Street, London WC1H OAJ, United Kingdom. Terry Edwards, a guest scientist at NBS, now has the address: School of Mathematical and Physical Sciences, Murdoch University, Murdoch WA 6150, Australia. James Mehl is a Professor of Physics at the University of Delaware. Richard Davis is a physicist in the Length and Mass Division of the NBS Center for Basic Standards.

References

[1] Cohen, E. R., and Taylor, B. N. "The 1986 Adjustment of the Fundamental Constants," Codata Bulletin **63**, pp. 1–32 (1986).

[2] Colclough, A. R., "Methods for the Determination of the Gas Constant," Precision Measurement and Fundamental Constants II, B. N. Taylor and W. D. Phillips, Eds., Natl. Bur. Stand. (U.S.), Spec. Publ. 617 (1984), pp. 263–275.

[3] Deslattes, R. D., "The Avogadro Constant," Ann. Rev. Phys. Chem. **31**, 435 (1980).

[4] Campbell, I. D., "Gaseous Oscillations within a Perturbed Spherical Resonator," Acustica **5**, 145 (1955).

[5] Moldover, M. R., Waxman, M., and Greenspan, M., "Spherical Acoustic Resonators for Temperature and Thermophysical Property Measurements," High Temp. High Pressure **11**, 75 (1979).

[6] Mehl, J. B., "Resonance frequencies of deformed spherical resonators," J. Acoust. Soc. Am. **71**, 1109 (1982).

[7] Mehl, J. B., "Spherical acoustic resonator: Effects of shell motion," J. Acoust. Soc. Am. **78**, 782 (1985).

[8] Mehl, J. B., "Acoustic resonance frequencies of deformed spherical resonators II," J. Acoust. Soc. Am. **79**, 278 (1986).

[9] Moldover, M. R., Mehl, J. B., and Greenspan, M., "Gas-filled spherical resonators: theory and experiment," J. Acoust. Soc. Am. **79**, 253 (1986).

[10] Ewing, M. B., McGlashan, M. L., and Trusler, J. P. M., "The Temperature-Jump Effect and the Theory of the Thermal Boundary Layer for a Spherical Resonator. Speeds of Sound in Argon at 273.16 K," Metrologia **22**, 93 (1986).

[11] Mehl, J. B., and Moldover, M. R., "Precision acoustic measurements with a spherical resonator: Ar and C_2H_4," J. Chem. Phys. **74**, 4062 (1981).

[12] Mehl, J. B., and Moldover, M. R., "Measurement of the ratio of the speed of sound to the speed of light," Phys. Rev. A **34**, 3341 (1986).

[13] Colclough, A. R., Quinn, T. J., and Chandler, T. R. D., "An acoustic redetermination of the gas constant," Proc. R. Soc. London Ser. A **368**, 125 (1979).

[14] Kirchhoff, G., "Über den Einfluss der Wärmeleitung in einem Gase auf die Schallbewegung," Ann. Physik Chem. (Fifth Ser.) **134**, 177, (1868); English translation "On the Influence of Heat Conduction in a Gas on Sound Propagation," by R. B. Lindsay in Benchmark Papers in Acoustics: Physical Acoustics, R. B. Lindsay, Ed., Dowden, Hutchinson, & Ross, Stroudsburg, Pennsylvania (1974), pp. 7–19.

[15] Rayleigh, J. W. S., Theory of Sound, 2nd ed. 1896, reprinted by Dover, New York, 1945, Sec. 331.

[16] Foch, J. D., and Ford, G. W., "The dispersion of sound in monatomic gases," in Studies in Statistical Mechanics, Vol. V, J. de Boer and G. E. Uhlenbeck, eds., North Holland Publ. Co. (Amsterdam, 1970).

[17] Greenspan, M., "Propagation of Sound in Five Monatomic Gases," J. Acoust. Soc. Am. **28**, 644 (1956); and "Transmission of Sound Waves in Gases at Very Low Pressures," in Physical Acoustics, Vol. IIA, Academic, New York (1965), pp. 1–45.

[18] Ernst, M. H., and Dorfman, J. R., "Nonanalytic dispersion relations in classical fluids," Physica **61**, 157 (1972).

[19] Kennard, E. H., Kinetic Theory of Gases, (McGraw-Hill, New York, 1938), pp. 311–316.

[20] Thomas, L. B., and Golike, R. C., "A Comparative Study of Accommodation Coefficients by the Temperature Jump and Low Pressure Methods and Thermal Conductivities of He, Ne, and CO_2," J. Chem. Phys. **22**, 300 (1954).

[21] Harris, R. E., "On the Determination of Thermal Accommodation Coefficients in the Temperature-Jump Region," J. Chem. Phys. **46**, 3217 (1967).

[22] Shields, F. D., and Faugh, J., "Sound velocity and absorption in low-pressure gases confined to tubes of circular cross section," J. Acoust. Soc. Am. **46**, 158 (1969).

[23] Shields, F. D., "An acoustical method of determining the thermal and momentum accommodation of gases on solids," J. Chem. Phys. **62**, 1248 (1975).

[24] Mehl, J. B., unpublished calculations of effects of surface profile on the thermal boundary layer.

[25] Greenspan, M., unpublished notes on the spherical acoustic resonator.

[26] Morse, P. M., and Ingard, K. U., Theoretical Acoustics, (McGraw-Hill, New York, 1968), Sec. 9.4.

[27] Trusler, J. P. M., unpublished calculations on the acoustic admittance of slits.

[28] Goodwin, A. R. H., Ph.D. Thesis, University of London (1988).

[29] In order to describe materials and experimental procedures adequately, it is occasionally necessary to identify commercial products by manufacturers' name or label. In no instance does such identification imply endorsement by the National Bureau of Standards, nor does it imply that the particular product or equipment is necessarily the best available for the purpose.

[30] Mehl, J. B., "Analysis of resonance standing-wave measurements," J. Acoust. Soc. Am. **64**, 1523 (1978).

[31] Data provided by the manufacturer, Bruel & Kjaer, Copenhagen, Denmark, in the pamphlet "Microphones and Microphone Preamplifiers," (1976).

[32] Cutkosky, R. D., "An automatic resistance thermometer

bridge," IEEE Trans. Instr. and Meas. **IM-29**, 330 (1980); "Grounding techniques in resistance thermometry," IEEE Trans. Instr. and Meas. **IM-30**, 217 (1981).

[33] Riddle, J. L., Furukawa, G. T., and Plumb, H. H., "Platinum Resistance Thermometry," NBS Monograph 126, U.S. Govt. Printing Office, Washington D.C. (1973).

[34] Mehl, J. B., unpublished notes on the effects of non-uniform temperature on the acoustic eigenfrequencies.

[35] Cook, A. H., and Stone, N. W. B., "Precise measurements of the density of mercury at 20 °C I. Absolute displacement method," Phil. Trans. R. Soc. London A **250**, 279 (1957).

[36] Cook, A. H., "Precise measurements of the density of mercury at 20 °C II. Content method," Phil. Trans. R. Soc. London A **254**, 125 (1961).

[37] Guildner, L. A., Stimson, H. F., Edsinger, E. R., and Anderson, R. C. "An accurate mercury manometer for the NBS gas Thermometer," Metrologia **6**, 1 (1970).

[38] Sloggett, G. J., Clothier, W. K., and Ricketts, B. W., "Determination of $2e/h$ and h/e^2 in SI units," Phys. Rev. Lett. **57**, 3237 (1986).

[39] Cook, A. H., "The Expansion of mercury and fused silica between 0 and 300 °C," Brit. J. Appl. Phys. **1**, 285 (1956).

[40] Girard, G. collator "Section: Density," Pure and Appl. Chem., in proof.

[41] Seemann, H. J., and Klein, F. K., "Schallgeschwindigkeit und Kompressibilität von Quecksilber und geschmolzenem Alúminium," Z. Ange. Phys. **19**, 368 (1965).

[42] Hayward, A. T. J., "Precise determination of the isothermal compressibility of mercury at 20 C and 192 bar," J. Phys. **D4**, 951 (1971).

[43] Patterson, J. B., and Prowse, D. B., "Comparative measurements of the density of mercury," Metrologia **21**, 107 (1985).

[44] CSIRO Measurement Report RS 14251, April 9, 1987.

[45] Giacomo, P., "Equation for the determination of the density of moist air (1981)," Metrologia **18**, 33 (1982).

[46] Almer, H. E., Bowman, H. A., Jensen, M. W., Macurdy, L. B., Peiser, H. S., and Wasko, B., "A direct reading two-knife 50-pound balance of high precision suitable for state weights and measures laboratories," J. Res. Natl. Bur. Stand. (U.S.) **68C**, 141 (1964).

[47] ASM Committee on Wrought Stainless Steels, "Wrought stainless steels," in Metals Handbook, Ninth Edition, Vol. 3, American Society for Metals, Metals Park, OH (1980) pp. 34–35.

[48] Prowse, D. B., and Anderson, A. R., "Calibration of a set of masses in terms of one standard mass," Metrologia **10**, 123 (1974).

[49] Davis, R. S., "Note on the choice of a sensitivity weight in precision weighing," J. Res. Natl. Bur. Stand. (U.S.) **92**, 239 (1987).

[50] Kochsiek, M. "Measurement of water adsorption layers on metal surfaces," Metrologia **18**, 156 (1982).

[51] Mehl, J. B., unpublished notes on the elastostatics of thick spherical shells.

[52] Ku, H. H., "Statistical Concepts in Metrology," NBS Spec. Pub. 300, Vol. I, Ku, H. H., editor, pp. 296–20 to 330–54 (1969).

[53] Roark, R. J. Formulas for Stress and Strain, 2nd ed., McGraw-Hill Book Company, Inc., New York, p. 276 (1954).

[54] Ledbetter, H. M., Weston, W. F., and Naimon, E. R., "Low-temperature elastic properties of four austenitic stainless-steels," J. Appl. Phys. **46**, 3855 (1975); see especially note added in proof.

[55] Hayward, A. T. J., "How to measure the isothermal compressibility of liquids accurately" J. Phys. **D4**, 938 (1971).

[56] Lowell, S., and Shields, J. E., Powder Surface Area and Porosity, 2nd ed., Chapman and Hall, New York (1984).

[57] Carslaw, H. S., and Jaeger, J. C., Conduction of Heat in Solids, 2nd ed., University Press, Oxford (1959), see especially equation (8), p. 234.

[58] Ellison, A. H., Klemm, R. D., Schwartz, A. M., Grubb, L. S., and Petrash, D. A., "Contact angles of mercury on various surfaces and the effect of temperature," J. Chem. Eng. Data **12**, 607 (1967).

[59] Holland, P. W., "An analyzer for determining helium-4 in the parts-per-billion range," Bureau of Mines Report of Investigations **8853**, (1984); Seitz, C. A., and Holland, P. W., "An improved analyzer for determining helium-4 in the parts-per-billion range," Bureau of Mines Report of Investigations **9010**, (1986).

[60] Simpson, C. J. S. M., Chandler, T. R. D., and Strawson, A. C., "Vibrational relaxation in CO_2 and CO_2-Ar mixtures studied using a shock tube and laser-Schlieren technique," J. Chem. Phys. **51**, 2214 (1969).

[61] Kneser, H. O., and Roesler, H., "Die Schallabsorption in CO_2-Ar Mischungen," Acustica **9**, 224 (1959).

[62] Wapstra, A. H., and Audi, G., "The 1983 Atomic Mass Evaluation," Nuclear Physics **A432**, 1 (1985).

[63] Nier, A. O., "A Redetermination of the Relative Abundances of the Isotopes of Carbon, Nitrogen, Oxygen, Argon, and Potassium," Phys. Rev. **77**, 789 (1950).

[64] Quinn, T. J., Colclough, A. R., and Chandler, T. R. D., "A new determination of the gas constant by an acoustical method," Phil. Trans. R. Soc. Lond. **A238**, 367 (1976).

[65] Melton, C. E., Massey, W., and Abels, B. N., "The Isotopic Abundance of Neon, Argon, and Krypton," Z. Naturforsh. **26a**, 1241 (1970).

[66] Aziz, R. A., and Slaman, M. J., "The argon and krypton interatomic potential revisited," Molecular Phys. **58**, 679 (1986).

[67] Maitland, G. C., Rigby, R., Smith, E. B., and Wakeham, W. A., Intermolecular Forces: Their Origin and Determination, Clarendon Press, Oxford (1981) pp. 568–572.

[68] Aziz, R. A., McCourt, F. R. W., and Wong, C. K., "A new determination of the ground state interatomic potential for He_2," Molecular Phys., to be published.

[69] Guildner, L. A., and Edsinger, R. E., "Deviation of International Practical Temperatures from Thermodynamic Temperatures in the Temperature Range 273.16 K to 730 K," J. Res. Natl. Bur. Stand. (U.S.) **80A**, 703 (1976).

[70] Bevington, P. R., Data Reduction and Error Analysis for the Physical Sciences, McGraw-Hill Book Co., New York (1969).

[71] Rowlinson, J. S., and Tildesley, D. J., "The determination of the gas constant from the speed of sound," Proc. R. Soc. Lond. **A358**, 281 (1977).

[72] Aziz, R. A., and Chen, H. H., "An accurate intermolecular potential for argon," J. Chem. Phys. **67**, 5719 (1977).

[73] "Round Table Discussion of Statement of Data and Errors," Nuclear Instruments Methods **112**, 391 (1973).

Appendix 1. Resonance Frequencies and Half-Widths for Ar-M near T_t

Data from three separate fillings of the resonator are tabulated. For each filling, the data were taken in order of descending pressure. The data from the first filling were taken March 29–30, 1986; the data from the second filling were taken March 31–April 1, 1986; and, the data from the third filling were taken April 4–5, 1986. Each of the 14 sub-tables are headed by the pressure and the average temperature at which the frequencies are measured. In each sub-table, the frequencies appear in the order in which they were measured.

Mar 29, 1986
p/kPa=504.177
T/K=273.1637

f/Hz	g/Hz
2477.6853	0.2098
4259.8189	0.2785
6012.7468	0.3368
7756.4083	0.3923
9495.9044	0.4757
11233.0132	0.5238
11233.0110	0.5237
9495.9051	0.4757
7756.4092	0.3923
6012.7475	0.3370
4259.8194	0.2782
2477.6853	0.2103

Mar 29, 1986
p/kPa=401.361
T/K=273.1613

f/Hz	g/Hz
2477.2870	0.2338
4259.1434	0.3101
6011.8041	0.3748
7755.2022	0.4345
9494.4431	0.5163
11231.3188	0.5668
11231.3164	0.5674
9494.4431	0.5172
7755.2033	0.4345
6011.8054	0.3751
4259.1466	0.3091
2477.2882	0.2340

Mar 30, 1986
p/kPa=299.937
T/K=273.1595

f/Hz	g/Hz
2476.8988	0.2681
4258.4932	0.3567
6010.8968	0.4309
7754.0431	0.4974
9493.0404	0.5796
11229.6957	0.6392
11229.6960	0.6392
9493.0411	0.5796
7754.0440	0.4974
6010.8979	0.4309
4258.4941	0.3567
2476.8995	0.2681

Mar 30, 1986
p/kPa=199.894
T/K=273.1646

f/Hz	g/Hz
2476.5410	0.3250
4257.9010	0.4338
6010.0790	0.5236
7753.0041	0.6050
9491.7888	0.6958
11228.2544	0.7734
11228.2537	0.7730
9491.7879	0.6966
7753.0042	0.6049
6010.0782	0.5241
4257.9019	0.4341
2476.5411	0.3259

Mar 30, 1986
p/kPa=100.261
T/K=273.1630

f/Hz	g/Hz
2476.0952	0.4583
4257.1896	0.6103
6009.1145	0.7388
7751.7880	0.8577
9490.3337	0.9815
11226.5840	1.1059
11226.5860	1.1062
9490.3381	0.9805
7751.7894	0.8588
6009.1144	0.7381
4257.1906	0.6087
2476.0971	0.4576

Mar 31, 1986
p/kPa=449.295
T/K=273.1642

f/Hz	g/Hz
2477.4801	0.2213
4259.4705	0.2939
6012.2592	0.3560
7755.7852	0.4130
9495.1496	0.4939
11232.1376	0.5437
11232.1351	0.5443
9495.1494	0.4920
7755.7849	0.4128
6012.2581	0.3560
4259.4698	0.2936
2477.4799	0.2217

Mar 31, 1986
p/kPa=350.096
T/K=273.1608

f/Hz	g/Hz
2477.0926	0.2497
4258.8180	0.3303
6011.3492	0.4004
7754.6204	0.4634
9493.7385	0.5428
11230.5055	0.5990
11230.5037	0.6004
9493.7399	0.5427
7754.6220	0.4632
6011.3506	0.4003
4258.8197	0.3310
2477.0943	0.2489

Mar 31, 1986
p/kPa=250.250
T/K=273.1585

f/Hz	g/Hz
2476.7070	0.2919
4258.1715	0.3884
6010.4524	0.4696
7753.4758	0.5425
9492.3570	0.6248
11228.9056	0.6937
11228.9056	0.6956
9492.3579	0.6239
7753.4789	0.5423
6010.4551	0.4699
4258.1743	0.3895
2476.7085	0.2918

Apr 1, 1986
p/kPa=149.792
T/K=273.1650

f/Hz	g/Hz
2476.3359	0.3768
4257.5694	0.5002
6009.6255	0.6043
7752.4332	0.6996
9491.1034	0.7987
11227.4662	0.8948
11227.4656	0.8955
9491.1025	0.7970
7752.4330	0.6994
6009.6259	0.6053
4257.5696	0.4989
2476.3366	0.3764

Apr 1, 1986
p/kPa=50.041
T/K=273.1654

f/Hz	g/Hz
2475.7768	0.6511
4256.7109	0.8687
6008.4901	1.0571
7751.0437	1.2330
9489.4574	1.4198
11225.5861	1.6461
11225.5763	1.6474
9489.4455	1.4162
7751.0412	1.2398
6008.4925	1.0564
4256.7098	0.8664
2475.7762	0.6501

Apr 4, 1986
p/kPa=101.371
T/K=273.1740

f/Hz	g/Hz
2476.1523	0.4570
4257.2843	0.6075
6009.2473	0.7337
7751.9632	0.8543
9490.5428	0.9702
11226.8343	1.1015
11226.8343	1.1015
9490.5459	0.9682
7751.9624	0.8545
6009.2471	0.7345
4257.2830	0.6053
2476.1560	0.4554

Apr 4, 1986
p/kPa=75.154
T/K=273.1615

f/Hz	g/Hz
2475.9438	0.5300
4256.9563	0.7094
6008.8062	0.8554
7751.4103	0.9980
9489.8906	1.1392
11226.0768	1.2998
11226.0768	1.3003
9489.8899	1.1367
7751.4173	0.9980
6008.8090	0.8569
4256.9573	0.7059
2475.9475	0.5265

Apr 5, 1986
p/kPa=50.017
T/K=273.1656

f/Hz	g/Hz
2475.7762	0.6433
4256.7113	0.8696
6008.4930	1.0629
7751.0380	1.2289
9489.4720	1.4234
11225.5943	1.6433
11225.5867	1.6477
9489.4586	1.4182
7751.0401	1.2378
6008.4885	1.0606
4256.7119	0.8662
2475.7788	0.6504

Apr 5, 1986
p/kPa=25.396
T/K=273.1640

f/Hz	g/Hz
2475.4560	0.8932
4256.2613	1.2318
6007.9202	1.5216
7750.3487	1.7909
9488.6706	2.0601
11224.7581	2.5322
11224.7521	2.5631
9488.6751	2.0703
7750.3874	1.8123
6007.9058	1.5123
4256.2608	1.2243
2475.4644	0.9006

Appendix 2. Speed of Sound Squared in Ar-M at T_t

The speed of sound squared in Ar-M at T_t is tabulated as a function of the pressure and the mode used for the measurement. The square of the speed of sound was determined from the frequencies in Appendix 1 and includes corrections for the thermal boundary layer, the elastic response of the shell, the unequal radii of the hemispheres (in the second order of shape perturbation theory), and the difference between the temperature of the measurement and T_t. For the sake of definiteness, the correction for the thermal boundary layer uses the value 1 for the thermal accommodation coefficient.

p/kPa=504.177	
0,2	94883.396
0,3	94883.346
0,4	94883.321
0,5	94833.320
0,6	94883.270

p/kPa=401.361	
0,2	94855.267
0,3	94855.194
0,4	94855.196
0,5	94855.214
0,6	94855.205

p/kPa=299.937	
0,2	94828.439
0,3	94828.454
0,4	94828.471
0,5	94828.487
0,6	94828.516

p/kPa=199.894	
0,2	94803.326
0,3	94803.321
0,4	94803.308
0,5	94803.320
0,6	95803.362

p/kPa=100.261	
0,2	94779.334
0,3	94779.347
0,4	94779.360
0,5	94779.230
0,6	94779.294

p/kPa=449.295	
0,2	94868.238
0,3	94868.142
0,4	94868.116
0,5	94868.163
0,6	94868.147

p/kPa=350.096	
0,2	94841.578
0,3	94841.552
0,4	94841.563
0,5	94841.577
0,6	94841.587

p/kPa=250.250	
0,2	94815.834
0,3	94815.768
0,4	94815.831
0,5	94815.814
0,6	94815.865

p/kPa=149.792	
0,2	94791.066
0,3	94791.065
0,4	94791.076
0,5	94791.088
0,6	94791.125

p/kPa=50.041	
0,2	94767.808
0,3	94767.572
0,4	94767.564
0,5	94767.723
0,6	94767.528

p/kPa=101.371	
0,2	94779.808
0,3	94779.590
0,4	94779.648
0,5	94779.603
0,6	94779.585

p/kPa=75.154	
0,2	94773.462
0,3	94773.355
0,4	94773.430
0,5	94773.390
0,6	94773.397

p/kPa=50.017	
0,2	94767.836
0,3	94767.576
0,4	94767.494
0,5	94767.586
0,6	94767.750

p/kPa=25.396	
0,2	94763.099
0,3	94762.457
0,4	94761.858
0,5	94762.258
0,6	94761.909

Appendix 3. Resonance Frequencies and Half-Widths for Measurement of Speed of Sound Ratios near T_t

The frequencies and half-widths in these tables result from fitting six parameters in eq (4.1) to the measured voltage as a function of frequency. In each table, the frequencies appear in the order in which they were measured. The last two entries for Ar-M on May 14, 1986 were influenced by intermittent arcing in a transducer. These entries were not used in the computation of the speed-of-sound ratios.

Isotopically enriched Ar-40

May 14, 1986 p/kPa=130.565 T/K=273.1910		May 20, 1986 p/kPa=116.567 T/K=273.2014		May 21, 1986 p/kPa=103.570 T/K=273.2124	
f/Hz	g/Hz	f/Hz	g/Hz	f/Hz	g/Hz
2475.9112	0.4009	2475.8900	0.4239	2475.8761	0.4490
4256.8550	0.5322	4256.8292	0.5630	4256.8164	0.5977
6008.6264	0.6482	6008.5974	0.6853	6008.5866	0.7288
7751.1476	0.7481	7751.1160	0.7929	7751.1071	0.8419
9489.5342	0.8410	9489.5017	0.8921	9489.4967	0.9497
9489.5330	0.8414	9489.5032	0.8926	9489.4965	0.9494
7751.1458	0.7481	7751.1171	0.7924	7751.1062	0.8419
6008.6246	0.6483	6008.5990	0.6858	6008.5858	0.7283
4256.8535	0.5320	4256.8304	0.5629	4256.8156	0.5980
2475.9097	0.4011	2475.8917	0.4230	2475.8754	0.4487

Working gas: Ar-M

May 14, 1986 p/kPa=130.564 T/K=273.1883		May 20, 1986 p/kPa=116.838 T/K=273.2074		May 22, 1986 p/kPa=103.468 T/K=273.2158	
f/Hz	g/Hz	f/Hz	g/Hz	f/Hz	g/Hz
2476.3542	0.4011	2476.3759	0.4223	2476.3470	0.4502
4257.6170	0.5327	4257.6638	0.5625	4257.6243	0.5988
6009.7018	0.6481	6009.7753	0.6848	6009.7282	0.7292
7752.5341	0.7480	7752.6350	0.7916	7752.5792	0.8422
9491.2318	0.8420	9491.3607	0.8915	9491.2997	0.9506
9491.2305	0.8419	9491.3612	0.8913	9491.2998	0.9497
7752.5330	0.7486	7752.6347	0.7920	7752.5792	0.8428
6009.7008	0.6480	6009.7750	0.6854	6009.7275	0.7291
4257.6151	0.5321	4257.6641	0.5623	4257.6243	0.5990
2476.3522	0.4009	2476.3751	0.4225	2476.3469	0.4503

Volume 93, Number 2, March–April 1988
Journal of Research of the National Bureau of Standards

A Computer Controlled Data Acquisition System for Combustion Calorimetric Experiments

Volume 93 Number 2 March–April 1988

T. J. Buckley

National Bureau of Standards
Gaithersburg, MD 20899

and

J. M. Rukkers

Department of Informatica
Twente University of Technology
Enschede, The Netherlands

At NBS a data acquisition system for a flow calorimeter which accommodates large samples has been developed. The system is based on an instrument controller, scanners, and voltmeters, all available commercially. Detectors for temperature, gas flow rate, pressure, and gas chemical composition provide data on key operating parameters of the calorimeter. A real-time, multi-tasking, general-purpose, data acquisition program is described. Computer science concepts important to the design of the program are explained. The software is driven by tables of data loaded at the start of the experiment. Thus, program execution is changed by providing different tables of information for the data channels desired, data display, and data storage. Tasks for data acquisition, instrument control, data storage, calculations, data display, and run-time-parameter entry are activated or deactivated during the experiment by the operator. Sample results are presented to illustrate the use of the data acquisition system. The software developed for this system is well suited for the changing experiments commonly encountered in the research laboratory.

Key words: combustion; computer application; data acquisition; flow calorimetry; modular programming; multiprogramming.

Accepted: November 18, 1987

Introduction

As experiments become more sophisticated, the demand on data recording increases. This problem is compounded in the research laboratory where instrument development is occurring. As the instrument evolves, the data recording needs change, which often requires hardware and software changes in a computerized system. The following text describes our approach to minimizing the changes needed to cope with instrument modifications.

The National Bureau of Standards has developed a large sample flow calorimeter for use in studies on municipal solid waste [1,2]. This instrument has been used in heats of combustion studies [3] and in investigations on the fate of chlorine during combustion [4,5]. Details of the design and operation of the multi-kilogram capacity flow calorimeter used in these studies can be found in the publication by Churney and coworkers [6].

Calorimetric experiments have long been recognized as being tedious, time consuming, and suited for automation. Westrum [7] has discussed the benefits of automating calorimeters, described the data acquisition system for his heat capacity calorimeter, and listed other laboratories which have automated their experiments. In certain respects our calorimeter is even more demanding on the need for and requirements of data acquisition. As a result, our flow calorimeter has been automated to assist in monitoring its operation and help improve the integrity of the data.

As in any computer controlled experiment, it is both the hardware and software which make the system work. We have assembled a number of hardware components from commercial vendors resulting in a data acquisition system which has proven to be powerful and adaptable. Since the software is what really gives a computer system its operating character, we have taken an interdisciplinary approach, one joining computer science and physical chemistry, to produce a data acquisition system which is suited to our laboratory needs. Our instrument is a research calorimeter and combustor in which the experiments change regularly as we acquire new detection instruments and new insights into the problems being studied. If we are to progress with the changing detector configurations, a software design is needed which is well structured and easy to modify.

In developing the software we resisted the temptation to design a system which was unique to our calorimeter. Rather, we strived to design a software package which was based on the "generic" character common to experiments in general. Only the unique aspects of our calorimeter were treated in a manner which deviated from the "generic" software philosophy.

One of the authors is a computer scientist while the other is a physical chemist. Since this paper is most likely to be read by physical scientists with limited backgrounds in computer science theory, a portion of the following is a primer on concepts important to structured and concurrent programming related to our program. Other sections discuss calorimetry and combustion concerns, the data acquisition hardware and software, and key features of our data acquisition program.

Flow Calorimetry

The large sample flow calorimeter is unique and has certain data requirements not found in other calorimeters. One feature which is unusual is the sample size which it accommodates. Unlike conventional bomb calorimeters which use sample sizes of one or two grams, our instrument was designed for 2.5 kg samples and has been used with samples weighing up to 5.0 kg. When burned, these samples release on the order of 17 MJ/kg of energy at an average power of up to 35 kW. If the combustion proceeds too quickly, there is not enough heat capacity in the combustor to prevent its temperature from rising to the melting point of stainless steel. As one might guess, this is an undesirable situation. To prevent the possibility of the experiment getting out of control, the combustor is instrumented with an array of thermocouples used to monitor its temperature profile.

The size of the sample is the primary reason for using the flow calorimeter design instead of the conventional bomb design, because of the safety problems associated with a large constant volume system. Unlike the bomb calorimeter, where there is no mass flow between the combustion zone and the surrounding environment, the flow calorimeter requires a substantial volume of gases to enter and leave the combustor. The use of the flow combustion technique for burning the sample necessitated the use of certain detectors (to measure gas flow rate, pressure, and composition) not found on a bomb calorimeter.

Corrections to the observed temperature rise in a bomb calorimeter are about 2% for heat exchange with the surroundings and a total of 0.1% for the difference between experimental and standard states, ignition, and acid formation. The combined corrections amount to about a 2.1% change in the enthalpy of combustion computed from the observed temperature rise alone.

In flow calorimetry, oxygen or air enriched with oxygen enters the combustor and the product gas leaves with varying amounts of oxygen, carbon dioxide, water, and a small amount of carbon monoxide. Thus, the composition and flow rate of the gas must be monitored in real-time during the burn. Corrections to the observed temperature rise are about 4% for heat exchange with the surroundings. Tens of thousands of liters of gas flow through the calorimeter. As a result, corrections due to carbon monoxide formation, water evaporation, and gas heating can be as high as 1.5%. The combined corrections amount to about a 5.5% change in the enthalpy of combustion obtained from the temperature rise of the calorimeter fluid [6].

Combustion Combustion experiments, as distinct from flow calorimetric experiments, place a further burden on the data acquisition system. In combustion experiments, the important questions involve quantitative accounting for the major components and the production of trace amounts of unburned hydrocarbons, chlorinated organic compounds, carbon monoxide, and other species. Some of the species, such as chlorinated organic compounds, are in such small amounts that they must be trapped so a detectable amount accumulates. Other species, such as sulfur dioxide, are produced in large enough quantities allowing them to be observed using real-time standard spectroscopic

techniques. The nature of the experiments and the calorimeter/combustor requires many channels of data to be recorded for extended periods of time.

Experiment Sequence

The calorimeter/combustor can be operated in two different modes: either as a combustion calorimeter or just as a combustor. When operated as a calorimeter, the temperature of the calorimeter water is most important. The compositions, temperatures, and flow rates of the inlet and outlet gases are of secondary importance. When used as a combustor, the primary parameters are the secondary ones for the calorimeter plus the combustor temperatures.

Table 1 lists the sequence of events during the two modes of operation. After assembly, the calorimeter is allowed to attain equilibrium heat exchange with its surroundings during the initial temperature drift period. The combustion zone is then purged of air with the oxidizing gas. The sample is ignited, followed by the burn, then the combustion zone is purged of product gases. The final drift period, instrument calibration, and disassembly complete the experiment. The sequence of events are similar for combustion experiments differing by the absence of drift periods before and after the burn and the final purge. Due to the size of the calorimeter, the time needed to reach a final steady state heat exchange with the surroundings is on the order of 2 hours. As a result, a combustion experiment requires less than half the time as a calorimetric experiment. The similarities between the two modes of operation compelled to us to develop generic software.

Table 1. Comparison of the sequence of events for calorimetry and combustion experiments

Event	Calorimetry	Combustion
1) Assemble	X	X
2) Temperature drift	X	
3) Purge	X	X
4) Ignite	X	X
5) Burn	X	X
6) Purge	X	
7) Temperature drift	X	
8) Calibrate instruments	X	X
9) Dissassemble	X	X

Experimental Apparatus

Calorimeter Configuration

The large sample flow calorimeter is diagrammed in figure 1. There are three main parts to the calorimeter: the gas inlet system, the combustor and calorimeter, and the product gas analyzer system. These sections are interfaced to a data acquisition system which records and displays the incoming data in real-time.

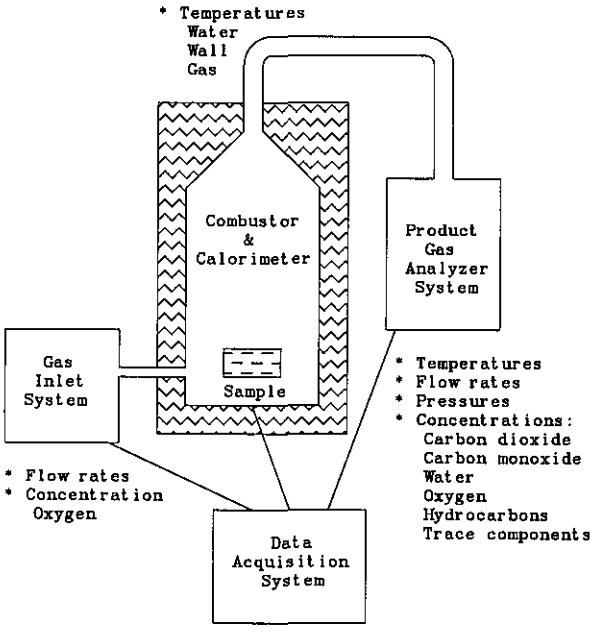

Figure 1. Block diagram of the large sample flow calorimeter and its data system. The parameters recorded from each section are indicated by a star (*). Unstarred items are specific data taken under the parameter listed above them.

The volume and composition of the gas entering the combustor is controlled by the gas inlet system. The valving in the manifold allows one to control the oxygen content of the oxidizing gas, monitor its flow rate, and intercompare the flow meters.

The calorimeter and combustor section is made up of a stainless steel combustion chamber with gas preheaters and six tiers of inlet nozzles that direct the oxidant gas at and around the sample. The surrounding calorimeter contains a metric ton of water which absorbs most of the heat of combustion. This section of the instrument is equipped only with temperature sensors.

The product gas analyzer has two sections. One is a gas trap for collecting chlorinated organics used during the fate of chlorine experiments. The other, used in every experiment, is composed of a group of instruments which measure the exhaust gas characteristics. They consist of infrared detec-

tors, pressure meters, temperature transducers, and a dew point meter to mention a few of the instruments involved.

Detectors and Sensors

Table 2 lists the various sensor types used to monitor the operation of the calorimeter. There are four classes of detectors and sensors used in our experiments: temperature, gas flow rate, pressure, and gas composition. The gas inlet system uses differential mass flowmeters [8] and a rotameter [9] to monitor the air and oxygen flow rates into the combustor[1]. These meters generate analog voltages with full scale readings corresponding to flow rates of 15 to 500 liters per minute depending on the meter. A ZrO_2 EMF cell [10] monitors the inlet oxygen content.

Table 2. Sensors and detectors on the calorimeter/combustor used to measure various physical parameters. The detector types are followed by their corresponding outputs

Sensor or detector	Output
Temperature:	
Thermocouples: Type T and Type K	microvolts
Quartz crystal thermometers [11]	frequency
Gas flow rate:	
Rotameters [9],[13]	volts
Differential temperature mass flow meters [8]	volts
Pressure:	
Absolute manometer [17]	volts
Differential manometers [18]	volts
Gas composition:	
Cooled-mirror humidity analyzer [14]	volts
Fixed wavelength infrared spectrometers [16]	*millivolts*
Scanning infrared spectrometer [15]	characters
Flame ionization detector hydrocarbon analyzer [12]	millivolts
Zirconium dioxide EMF cell oxygen analyzers [10],[19]	volts

The calorimeter/combustor assembly is equipped with temperature sensors of Type T and Type K thermocouples. The Type T couples are used to monitor temperatures near room temperature such as the gases entering and leaving the calorimeter while the Type K couples are used to measure high temperatures such as those of the combustor walls. Two quartz crystal thermometers [11] are used to measure the temperature of the calorimeter and surrounding jacket water.

[1] Company products are identified to adequately specify the apparatus. In no case does such identification imply recommendation or endorsement by the National Bureau of Standards, nor does it imply that the products are necessarily the best available for the purpose.

The product gas analyzer system involves several detector types. The temperature of the gas at various points is measured by Type T thermocouples. The concentration of hydrocarbons on the ppm level is monitored by a hydrocarbon analyzer [12] whose flow rate is measured by a rotameter [13]. Water vapor is measured by a cooled-mirror humidity analyzer [14] while the CO_2 and CO concentrations are determined by dedicated infrared detectors [15]. Minor constituents, such as HCl and SO_2, are monitored by a scanning infrared detector [16]. The gas pressure in the analyzer system is measured at three points by using an absolute manometer [17] and two differential manometers [18]. A ZrO_2 EMF cell [19] measures the product gas oxygen content. The chlorinated organic trap is instrumented with Type T thermocouples for temperature monitoring.

These detectors have a variety of different outputs from microvolt level signal from the thermocouples, to five volt signals from the flowmeters, to frequencies from the quartz crystal thermometers, to serial data (ASCII characters) from the scanning infrared spectrometer. In order to accommodate this wide range of voltages and data types, a versatile data acquisition system is needed.

Data Acquisition System

Until the purchase of our current instrument control system, we used a microcomputer and a minicomputer to record data from our experiments. The limited memory sizes (64KB, kilobytes, of RAM) and processing capabilities of these machines quickly became obstacles in our effort to expand the productivity of the data acquisition system. The problems were further complicated by the great differences between the operating systems, programming languages, and utilities of the two computers. These limitations have been remedied by our current system which replaces the two computers previously used.

A block diagram of the data acquisition system is shown in figure 2. The system can be divided into two parts: the acquisition instruments (top and left) and the computer system (lower right corner). The choice of the acquisition instruments allows for flexibility in the handling of the various detectors and sensors. Signals from most detectors arrive as analog voltages at two scanners [20] which provide, at present, a total of 80 channels of input. Of the 80 pairs of switches making up the two scanners, 20 have less than one microvolt thermal offset while 50 are rated at less than two microvolts.

These switches are used for measuring single thermocouple voltages to obtain a temperature resolution of a tenth of a degree. The remaining 10 pairs of switches are rated at 30 microvolts and are used only for high level signals. These switches allow us to handle a wide dynamic range in analog signal input.

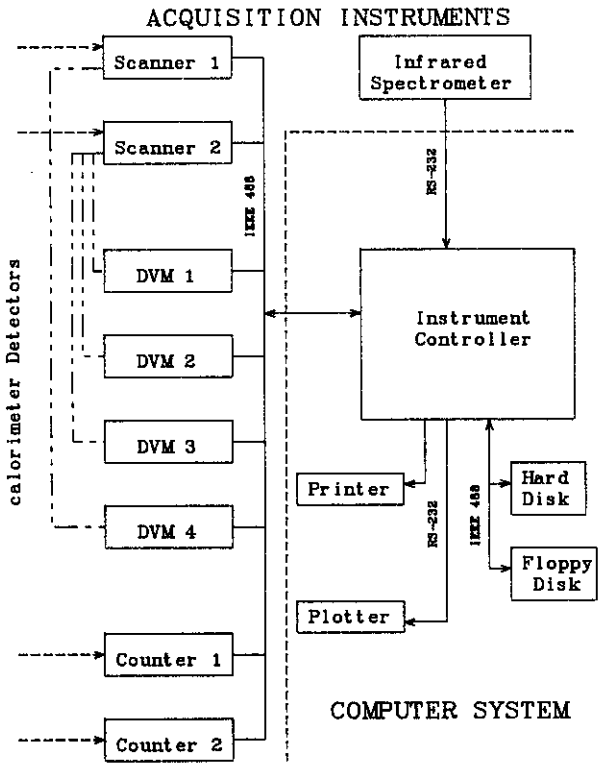

Figure 2. Diagram of the calorimeter/combustor data acquisition instruments and instrument control system.

The signals from the scanners are sent to one of four high precision digital voltmeters (DVMs) [21] to be digitized. The auto ranging feature of the DVMs allow the recording of signals ranging from a microvolt to a thousand volts. Two counters [22] are used to measure the frequency of the quartz crystal thermometers. The voltmeters, counters, and scanners used are well suited for the research laboratory by allowing one to measure ac/dc volts, resistance, or frequency with wide dynamic range and high precision.

The scanners and voltmeters are interfaced to the computer system through an IEEE-488 communications bus. The scanning infrared spectrometer sends data to the computer system through an RS-232 serial communications port.

The data acquisition system is controlled by an instrument controller [23], a unit which has also been used by Gallagher [24] in a system to acquire data from calorimeters. This computer is designed to service communication buses and ports in applications where the data acquisition instruments generate interrupts. The computer has 136KB of RAM of which 64KB is available for the operating system and user software. A high resolution monochrome graphic display with a touch sensitive overlay provides a convenient user interface. Mass storage is provided by two 400KB floppy disk drives, a 10MB (megabytes) hard disk drive, and 512KB of RAM used as a disk. Hard copy of text and graphics is provided by a dot-matrix printer and a multi-pen color plotter. An IEEE-488 and four serial communications ports allow the computer to access the instruments.

Software Tools

The Fluke instrument control system is furnished with several software tools and language features. Fluke's own disk operating system (FDOS) provides basic control of the hardware. A self test is performed upon power up while a diagnostics package aids in hardware trouble shooting. An editor, file manager, and other utility programs are provided for system maintenance.

The computer can be programmed in any of four languages: FORTRAN, Interpretive BASIC, Compiled BASIC, and assembly language. A linker allows limited combinations of the four languages, such as subroutines written in FORTRAN can be executed by a program written in Compiled BASIC.

While Interpretive BASIC is useful for testing new hardware devices and program segments, Compiled BASIC is used for execution of our calorimeter program due to its faster execution speed. Other features, such as the use of true subroutines and flow control statements, help in software development. Fluke's Compiled BASIC has program flow control statements (EXTENDED IF, WHILE, REPEAT, LOOP, LEAVE, and SELECT-CASE) found in Pascal, a language designed to teach programming as a systematic discipline. Virtual arrays, arrays used as if in main memory but reside on disk, greatly expand Fluke BASIC's ability to handle large data sets. The program also can be made much larger by making sections of the code into overlays which are stored on disk and only loaded when needed. The instrument control character of the computer is evident in the

high level language structures provided for servicing interrupts. Interrupts can be called by a serial port, an IEEE-488 port, time of day and interval clocks, an error, or a touch sensitive screen. These and other features make the system very useful in a real-time interrupt-driven environment.

Data Acquisition Software

Structured Programming

The demands of large sample flow calorimetry, the idiosyncrasies of the hardware used, and the flexibility needed in a research laboratory environment dictate a software package which is not trivial. When developing complex software it is very important to use a structured approach to programming. This is especially true when working with languages such as BASIC which have arbitrary transfer of control statements (i.e., the GOTO statement).

An unstructured approach may seem expedient, since there will finally be a program that "gets the job done," but in the long run this approach is uneconomical due to the time spent in later modifications of the software. Unstructured programs very often turn out to be "logical spaghetti" which are not easy to modify or debug. Computer scientists such as Dijkstra [25] have discussed in detail structured programming and its relationship to effective and reliable programs. Based on the advice of the experts, we proceed with the structured approach to programming.

Computer Science Concepts and Definitions

When developing a program, a design methodology is needed. A very good and widely understood method is the top-down approach. This means that one first comes up with a general description of the overall program structure, and then starts refining the various parts until the actual program is generated. Starting with a mixture of natural language type descriptors and formal control functions (WHILE, REPEAT, etc.) refinements are made until the detailed program statements are produced.

For the interested reader, more details concerning these topics can be found elsewhere. The following lists some excellent papers dealing with topics of interest: structured programming and correctness, hierarchical program structures, structuring of data (which has a significant impact on the program) [26], top-down programming [27], managing of program development [28], and concurrent programming [29].

The introduction of the concept of modular program code is very important when structuring a program. Program modules introduce a separation of concerns: different processes reside in different modules. This concept can be applied at many levels of abstraction [26,28]. Modular programming is a great thinking and development aid and promotes the design of a well structured system.

Processes

A sequential program specifies sequential execution of a list of statements; its execution is called a process. A concurrent program specifies two of more sequential programs that may be executed concurrently as virtual parallel processes.

A concurrent program can be executed by allowing processes to alternately share one processor. This approach is referred to as multiprogramming and is supported by an environment that multiplexes the processes on the processor [30]. The program operates as if each process is executed on its own virtual variable-speed processor.

In order for processes to cooperate, concurrently executing processes must communicate and synchronize with each other. Communication allows execution of one process to influence the execution of another. Interprocess communication is based on the use of shared variables (data that can be referenced by more than one process).

Synchronization is often necessary. Since processes are executed with unpredictable speeds, one process may have to wait for certain actions to be performed by another process before continuing its execution. For example, imagine a process that is acquiring data from an external source. Another process, that performs an operation such as a calculation using the data from the former process, will have to wait for this process to make the data available before it can do its computation.

Processes can be divided into two categories: foreground and background. Background processes are either active or passive (dormant). When a process is activated, it is inserted into the background and executes until it becomes passivated. More than one background process can be competing for the computer's resources at a given time. Foreground processes are essential interrupt-driven operations. They have priority over the background processes, whose execution is preempted to make processor time available for the foreground process. Foreground processes cannot preempt one another.

In order to multiplex the various processes on one processor, the following scheduling mecha-

nisms are provided. The foreground solution is straight forward; the occurrence of an interrupt is the scheduling entity and since only one interrupt can be active at a given time, no other mechanism has to be provided.

The background processes are scheduled by using the following continuous loop solution.

```
REPEAT
  IF active(p1) THEN p1(interface list)
  IF active(p2) THEN p2(interface list)
  .
  .
  IF active(pn) THEN pn(interface list)
UNTIL False
```

The boolean variables used in the loop, active(pn), are guards signalling the state of a process, pn, being either active or passive. When a process is activated, the subroutine for the process, pn(interface list), is called. Thus, the processor time is divided over the active processes. If there are no processes active, then the computer waits in the loop until an interrupt occurs at which time one of the processes may be activated.

A scheduling mechanism should be fair to be adequate, e.g., no process should be delayed forever. The continuous loop described is bounded fair. That is, a process waiting to get access to the processor is delayed for at most the execution times of the other active processes. Of course, the continuous loop scheduling mechanism is fair only when none of the other processes is executing indefinitely. To insure this is so, it is desirable that the execution time of a process at each call is "short." The continuous loop scheduling mechanism will then establish a good sharing of the processor time. For a more complete discussion of fairness see the article by Lehman [31].

When dealing with concurrent processes, it is necessary to insure that no unwanted influence will take place between two processes. There will be some critical sections of code that have to be protected. This is partly provided by the BASIC language used since it executes statements on one line in an atomic matter; interrupts can only be serviced before or after the statement is executed and never during. The language also provides ENABLE and DISABLE interrupt statements that can be used to protect critical program segments from unintentional changes. These entities give sufficient possibilities for solving the unwanted influence problems we faced.

The possibility of introducing a deadlock situation has to be considered. Deadlock is a state of affairs in which two or more processes are waiting for events which will never occur. More explicitly, a processes will continue testing a certain variable for change but will not see it (this is sometimes called "spinning"), because the process that is supposed to set this variable is blocked on a variable that has to be set by the first process. This situation has to be prevented from occurring by carefully using the continuous loop scheduling mechanism.

The continuous loop scheduling mechanism prohibits very long iterations or recursions in a process using the WHILE or REPEAT Compiled BASIC language commands. In order to iterate, the process must save its variables upon completion of any iteration step and continue on the next opportunity through the scheduling loop. The mechanism used for saving the state conditions and for holding the shared variables used for synchronization is called the interface list. It consists of variables that are exchanged between the process and the main program and used for the previously mentioned purposes. The interface list is explored in more depth in the following section.

Program Environment A process needs an environment in which it can be executed. This environment consists of two parts: 1) a dynamic environment formed by the behavior of the active processes, 2) a static environment consisting of the data structures that are used to enable the process to be aware of the dynamic or changing environment.

The static environment can be viewed as a window to the state of the system at a particular moment. This window is provided by the parameter lists of the processes. By examining the variables of the parameter lists, the program determines what the appropriate actions are under the given conditions. Thus, this list is essentially an interface list that couples the necessary global data to the processes.

Using the static environment, it is possible to synchronize the various processes by letting the interface lists overlap, thus providing variables common to the interrelated processes. It should be stated that, while this solution to the synchronization problem is sufficient, it is not the best way to solve the problem. It would be convenient to use some more sophisticated primitives for scheduling and synchronizing to give one more flexibility and a better program structure. The P&V concept, the cobegin [30], and the fork and join [32] are worth mentioning in this context. The overlapping interface list solution is considered the best possible, given the limitations of Compiled BASIC, and provides a good and conceptually clean program structure.

Modules As previously stated, a modular approach is desired to control the complexity of the system. It also provides a separation of concerns by localizing entities to the processes where they are used. Essentially, a module consists of what we call a process and the local routines that support the execution of that process. Since there are also the global routines that make up the environment of a process, the overall architecture can be pictured as in figure 3. The main program, which manages the scheduling of the processes, is coupled through interface lists to the modules, which contain the computer commands for the tasks discussed next.

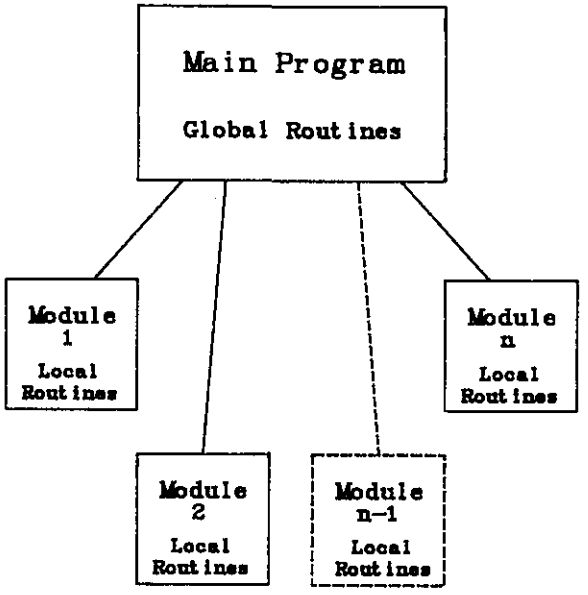

Figure 3. Diagram of the calorimeter program architecture showing the creation of modules as subsections of the main program.

Experiment Tasks The structure of our data acquisition software is developed from the combustion and calorimetric experiment task list. The tasks identified as characteristic of a general purpose combustion experiment are given in table 3. In order to implement the program design, the interrupt-driven tasks are identified as the foreground processes. They involve the data collection, the data channel selection, and error handling. The rest of the tasks are implemented in the background processes using the continuous loop scheduling mechanism previously described. The processes to be performed can easily be written in the form of modules to complete the program structure.

Table 3. Tasks performed by our combustion calorimetry data acquisition system and their execution modes

Task	Foreground	Background
Instrument control		
Initialize devices	X	X
Select data input channels	X	
Trigger digitizers	X	
Data collection		
Voltage input	X	
Frequency input	X	
Serial input	X	
Data recording		
Store data on mass storage device	X	
Print data on hard copy device		X
Data calculations		
Convert data to physical quantities		X
Derive quantities from the data		X
Video display		
Show raw data voltage readings		X
Show calculated quantities		X
Plot data as a function of time		X
Show experiment control menus		X
Parameter input		
Reference temperature		X
Burn starting time		X
Scale values for plot routine		X
Software initialization		X
Error handling	X	

Program Configuration

An important feature to support the flexibility of our program is the program database. Since the data acquisition sequence may be changed very often, the program has the opportunity to be tailored to the required data channel selection scheme. The data acquisition sequence is handled by a timetable database which can be easily changed or generated. Therefore, a change in the acquisition sequence does not involve recoding but uses the features of a database generator to create the desired data structure. Also, the displays are of a general character, driven by a display database structure that also can be easily changed. Our program for data acquisition is divided into three parts: the program statements, database, and database manipulator.

Figure 4 shows the overall architecture of the cooperating processes which make up the data acquisition program. Shown are not only the real processes as they were derived from the initial task recognition and analysis, but also how processes are synchronized (indicated by the dashed lines) relative to one another. As an example, the process

displaying the results computed from the synchronous data has to first wait for the data to be acquired and computations completed. The interface list driven processes are called from the continuous loop of the main program while the interrupt driven processes are executed when an interrupt occurs.

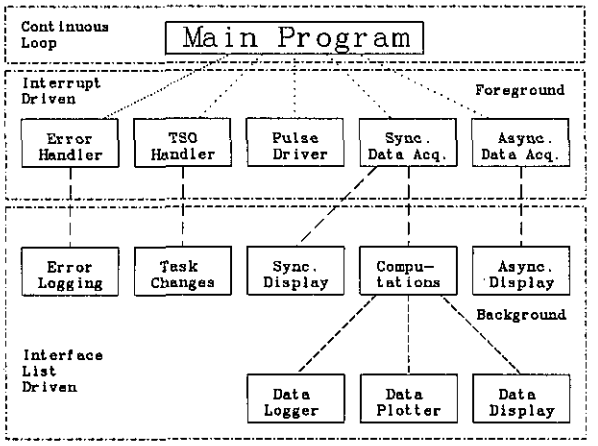

Figure 4. Total architecture of the calorimeter program. The main program operates in a continuous loop. Interrupts force various processes to be performed, then pass on parameters in an interface list to enable execution of other processes.

Data Acquisition

The data acquired can be separated into two different types: synchronous and asynchronous data. The acquisition of synchronous data is controlled by the clock and composes the majority of the data recorded during our experiments. The asynchronous data arrives at the computer at a pace which is not dependent on operation of our data acquisition program but only upon the instrument transmitting the data.

Synchronous Data Acquisition The scheme we use for the acquisition of synchronous data can be viewed as an active foreground process. This process is constantly executing a data logging loop in which channels are selected for digitizing at a specific moment. The timing of the data acquisition scheme is interrupt driven, so that processor time not used when the acquisition process is idle can be used by active processes in the background.

Our data logging loop is established by a one second interrupt interval timer we call the experiment "pulse." Each second, the timer generates an interrupt which causes program statements in the pulse driver process to be executed. The pulse driver uses the timetable database (described later) to determine which channels should be selected by a scanner during a particular second and triggers the data acquisition devices attached to the channels. When the devices have their data available, they generate a service request flag and the background processes are temporarily stopped to allow the synchronous data acquisition process in the foreground to be executed.

Asynchronous Data Acquisition The acquisition of asynchronous data is a foreground process in which our program does not initiate the data coming in but only records it. This mode of operation is characteristic of data from our scanning infrared detector, which sends data as it becomes available down a serial interface line to the data instrument controller. Datum from the serial port generates an interrupt which is then read and stored on disk by the asynchronous data acquisition process if it is activated, otherwise the data is lost.

Timetable Database The foundation of our data acquisition program is formed by the timetable database. The information stored in this database is used for determining the behavior of the program. The timetable gives the program the channel numbers to be selected at a specific time and the device from which to read the data.

The structure of the timetable, shown in figure 5, is closely related to the experiment. A minute is divided into 60 seconds, each in which data collection can take place. The timetable is a two-dimensional array 60 rows long by four columns wide. Each row corresponds to a second of each minute in which any combination of four DVMs can be given a channel to digitize. When a non-negative entry occurs in the timetable, it indicates that channel is to be selected by the scanner and the appropriate device to be triggered. Eventually, the data acquisition device responds by sending a service request flag to the computer, followed by the execution of the synchronous data acquisition process which reads and stores the datum on disk.

The introduction of this timetable concept provides a powerful and flexible tool for tailoring the program to the needs of a specific experiment, a general need characteristic of a research laboratory. It is not necessary to change the program code in order to change the behavior of the program, the only thing to be done is to generate a timetable which resembles the structure of the experiment to be performed.

Digitizer

Second	DVM 1	DVM 2	DVM 3	DVM 4
1	39	27		
2	38	25		
3	37	24	C	C
4	36	−1	h	h
5	35	0	a	a
6	34	−1	n	n
7	33	5	n	n
8	32	−1	e	e
⋮	⋮	⋮	l	l
			s	s
			40	60
			to	to
			49	69
56	34	−1		
57	33	14		
58	32	−1		
59	31	6		
60	30	13		

Figure 5. Two-dimensional timetable used to sequence the data acquisition channel selection. Each row corresponds to a second in a minute and each column corresponds to one of four DVMs. The non-negative numeric entries are scanner channels to be digitized while the minus ones are when no data are recorded.

Data Storage Structures Storage of the acquired data is provided by the implementation of an abstract data structure, consisting of several virtual arrays linked together and the subroutines GET and STORE we developed. This approach enhances the language features that were available in Compiled BASIC by allowing for a single data storage array that is much larger than is normally permitted. Since the programmer only has to use the STORE and GET subroutines to save and retrieve data from storage, there is no problem of finding the data's location in the linked virtual arrays.

Synchronous Data Storage The data manipulated by the program is divided into two groups: the raw data coming from the data acquisition instruments and the calculated data derived from the raw data. Raw data are saved on a hard disk, thus providing a non-volatile storage medium. This protects the data already recorded from being lost in case the computer system goes down. The calculated data are stored on an electronic disk to provide fast access to the derived quantities.

The synchronous data are stored in the equivalent of a two dimensional array of the form shown in figure 6a. This array has the structure of the timetable. Each row of the data array corresponds to a minute during the experiment. Row 1 corresponds to the first minute while the total number of minutes allowed is dictated by the amount of virtual array space allocated and the number of channels recorded. Column 0 of the array contains the real-time in minutes at which the minute started while the remainder of the columns record the voltages.

a) Data File

Minute	Column 0	1 ·····		n−1	n
1	660	.12		9.8	.044
2	661	.05		9.5	.050
3	662	−.01		9.2	.057
4	663	−.03		8.9	.063
5	664	.11		8.6	.069
⋮					
	Time	Voltage		Voltage	Voltage
m−3					
m−2					
m−1					
m					

b) Map File

Channel Number

0	1	2	3	4 ·····	79	80	81
1	−1	5	2	−1		13	60	−1

Data File Column

Figure 6. Diagrams of data file (a) and map file (b) used to store synchronous data from the channels selected in the timetable. Each row in the data file corresponds to a minute when data are recorded. *Column 0 entries are the minutes in real-time when* the data were recorded. The rest of the columns contain voltage measurements corresponding to one of the scanner channels recorded during the experiment. The map file entries are column numbers of the data file used to store each of the scanner channel numbers. A −1 indicates that the scanner channel was not recorded.

Due to the data structure, only one value can be stored for a specific channel for a given minute. When multiple readings are taken from a single channel, either the last voltage read or the average of the set of readings is stored.

Usually, only a subset of the available channels are recorded during a specific experiment. In order to optimize storage use, a variable mapping of the channels to the array columns is provided by using a map file illustrated in figure 6b. This one dimension array is 82 (0 to 81) units long. Each entry corresponds to a physical channel number; the first 80 are for the scanner channels and the last two are for the frequency counters. When a channel is to be recorded during an experiment, it is assigned a column number in the map file. If a channel is not to be used, it is assigned a -1. Note that the channels do not have to be assigned sequentially since the GET and STORE subroutines use the map file for determining data placement.

This technique has a distinct advantage of efficient utilization of storage space. One can trade off the maximum recording time for the number of channels recorded. For every 64KB of storage used (up to 256KB can be assigned to an array) two channels can be recorded for 45 hours while all 80 channels can be saved for 1.7 hours.

Asynchronous Data Storage Storage of the asynchronous data is provided in a fashion similar to the synchronous data. Since there are no channels and minutes, the dimensions of the data storage array is of a fixed length and width. The asynchronous data in our experiment comes from the scanning infrared detector and have a known order. The absorbance of the sample at several wavelengths is monitored, transmitted as serial datum to the computer, and printed in order. Each row of the data storage array is designed to be wide enough to save each set of absorbance readings plus one more column for the minute during which transmission of each data set started. An end of record (the characters carriage return and line feed), which separates the data sets, provides a signal to indicate when the row count of the data storage array should be incremented and the time information recorded.

Interactive Program Control

Since our program is actually made up of several processes that can be either active or dormant, a tool has to be provided to manipulate the state of these processes. Therefore, we developed operator interface software which exploits the features offered by a video screen with a touch sensitive overlay (TSO). Pushing a touch sensitive pad on the screen initiates the foreground process, TSO handler, which activates or passivates a process. The TSO is also used to update various on-line parameters, such as references temperatures and plotting parameters, entered by the operator.

Miscellaneous Features

A good deal of the processes are mutually exclusive, that is they do not execute concurrently, so they can be exchanged in and out of memory while occupying the same region of memory. This is possible by using the overlay feature provided by the computer's operating system. The main program, global routines, and the processes that are frequently executing concurrently always remain in memory. The rest of the processes are mutually exclusive (such as the displays) and reside in overlays and may only be present in memory when the process is executing.

A crucial feature of our program worth mentioning is its ability to recover from errors that may occur. Even when the computer system totally goes down, no data which has already been recorded is lost as long as the computer's real-time clock is not corrupted. This ability to recover is due to our storing the data on the hard disk immediately after reading them from the data acquisition instruments. When the computer is restarted, our program just continues the data acquisition where it would have been if the data recording had not been terminated. The resulting data set will have a blank spot in it, however, all of the data will be properly timed relative to the first part.

The ability of our program to recover from errors and continue collecting data is made possible by deriving the data acquisition timing from a real-time clock. The instrument controller's clock is read at the beginning of each system pulse. Subtracting the starting time, which was stored on the hard disk, from the pulse time gives the experiment time. This is converted into minutes and seconds. The minute is used to point to the proper synchronous data storage row, while the second tells which entry in the timetable should be used for channel selection.

Sample Results

No description of an instrument system would be complete without the displaying of sample results.

The initial record of an experiment is the raw data file stored on the hard disk. While the calculated data provide a more meaningful picture of what went on during a burn, they can be regenerated from the raw voltages recorded. Another valuable record is the list of printed data values logged during the burn. This record allows one to readily look up values for various times of the experiment and provides an added level of backup in case the disk files are lost.

The left half of one page from an experiment is shown in figure 7. The overall form of the page is similar to the channel selection pattern used. One page is produced for each minute of an experiment. The time of day and the experiment time, in minutes, are printed at the top of each page. The first column contains the second in which the data was recorded, while the next three columns contain a label, raw voltage, and calculated value for data from DVM1. This pattern is repeated for the next three columns for DVM2 and in two more sets of columns for DVM3 and DVM4 (not shown).

The columns for DVM1 show a regular pattern of nine channels digitized three times per minute.

```
Current time: 11:21:23
Current minute:  55

  1                                                Shi Top      0.000001   22.000
  2                                                Oxy In       0.215740   21.574
  3                                                Oxy Out     -1.266290  -12.663
  4
  5
  6
  7                                                Out Gas      0.006151  156.311
  8
  9                                                Samp Gas     0.008641  234.413
 10
 11      Var Fl        0.017175     0.017         Ox Bot       0.019475  493.257
 12      Xh2o          0.545390     0.930         Ox #1        0.020065  507.103
 13      CO(IR)        0.074799     0.038         Ox #3        0.014808  383.173
 14      CO2(IR)       0.222540    17.384
 15      CO Tc        -0.159420   -51.000         Low Top      0.012748  334.074
 16      CO2 Tc        0.000289    29.098         Up Con       0.010186  272.302
 17      Entry Tc      0.000612    36.909         Ox Top       0.005134  146.889
 18      N2 Flow      -0.008854    -0.009
 19      Miran Tc      0.000390    31.554         Up Mid       0.009933  266.139
 20                                               Mid Fla      0.008630  234.141
 21                                               Up Top       0.009534  256.387
 22                                               Exh Gas      0.014004  364.056
 23                                               Ar Gas       0.005407  153.670
 24                                               Bot Fla      0.013833  359.983
 25                                               Low Mid      0.023283  582.592
 25                                               Up Bot       0.009894  265.187
 27
 28                                               Low Bot      0.012844  336.371
 29                                               Samp Gas     0.008671  235.154
 30                                               Oxy Out     -1.267500  -12.675
 31      Var Fl        0.017175     0.017         Shi Top      0.000002   22.000
 32      Xh2o          0.543780     0.929         Oxy In       0.215130   21.513
 33      CO(IR)        0.079258     0.041         Out Gas      0.006191  157.082
 34      CO2(IR)       0.256730    20.665
 35      CO Tc        -0.120635   -51.000
 36      CO2 Tc        0.000288    29.074
 37      Entry Tc      0.000614    36.957
 38      N2 Flow      -0.008823    -0.009
 39      Miran Tc      0.000392    31.603
 40
 41                                               Ox Bot       0.019547  494.924
 42                                               Ox #1        0.020113  508.205
 43                                               Ox #3        0.014836  383.814
 44
 45                                               Low Top      0.012786  334.960
 46                                               Up Con       0.010227  273.276
 47                                               Ox Top       0.005175  147.882
 48                                               Mid Fla      0.008719  236.316
 49                                               Samp Gas     0.008698  235.797
 50                                               Up Mid       0.009998  267.699
 51      Var Fl        0.017200     0.017         Up Top       0.009583  257.562
 52      Xh2o          0.543660     0.929         Exh Gas      0.014026  364.556
 53      CO(IR)        0.088448     0.047         Ar Gas       0.005427  154.143
 54      CO2(IR)       0.257730    20.763         Bot Fla      0.013992  363.747
 55      CO Tc        -0.117322   -51.000         Low Mid      0.023290  582.733
 56      CO2 Tc        0.000289    29.098         Up Bot       0.009956  266.675
 57      Entry Tc      0.000611    36.885
 58      N2 Flow      -0.008899    -0.009         Low Bot      0.012959  339.098
 59      Miran Tc      0.000391    31.579
 60

Slot # :  54
          Reference   0.0026
                      0.0407
          Ethane      0.0135
          HCl        -0.0001
          CO          0.2357
          Water       0.9918
          SO2         0.0120
```

Figure 7. Sample print out from a typical experiment. Data from two DVMs are shown, while the data from the other two have been deleted for simplicity. Each numbered row corresponds to one second during a minute of synchronous data recording. The last eight rows show the asynchronous data storage row (Slot #) and the absorbance measurements from our scanning infrared detector.

The values for temperatures are individual measurements while the flow rates are averaged ones. The columns of data for DVM2 show a repeat of some data but not with the regularity of DVM1. Blank entries in the columns correspond to seconds when data was not recorded.

The bottom of the page has a set of data received from the scanning infrared detector. The data set number (Slot #) is followed by the absorbance readings at seven selected wavelengths. This set of numbers is printed at the next available opportunity after all seven readings are recorded. The timing is usually such that the numbers printed were recorded during the previous minute.

The video display contains the information shown in the printed output but organized in logical groupings of channels. Besides the label for a particular channel, the raw voltage or computed value is displayed along with the change since the last minute. Graphs of a selected channel as a function of time can also be plotted on the screen to see long term trends in the data. The video display also provides menus for the TSO which allow the operator to activate and deactivate various processes.

The use of the data to obtain calorimetric information has been discussed in detail [3] and will not be presented here. However, the use of the data for combustion experiments has not been presented previously and is given in the following discussion.

Figures 8 to 10 show graphs of three channels of data from a typical experiment where a sample of municipal solid waste with 5% added lime was burned. From these data we derive other physical quantities. The CO_2 (fig. 8) and CO (fig. 9) data are combined with flow rate data to give molar flow rates. The CO_2 molar flow rate curve is integrated to give the total amount of carbon in the original sample or used as is to indicate the rate of combustion. The CO molar flow rate curve gives a measure of the completeness of the combustion reaction.

The effects of changing parameters such as the gas flow rates or its oxygen content can be observed as changes in the slopes of these curves. The sample was ignited at minute 61 which is marked by a steep rise in the CO_2 concentration. At minute 71 the oxygen concentration was reduced to slow the burn down, but this was followed by an unacceptably high concentration of CO at minute 82. While watching the computer readouts, the oxygen concentration and gas flow rates were adjusted to lower the CO to an acceptable level of 0.1 mol%. The large CO peak at minute 156 is a characteristic peak that usually occurs when the sample combustion nears completion. The ability to see the data in real time allows us to control the combustor to study the effects of different operating conditions.

Two other peaks can be seen at minutes 262 and 273 minutes into the experiment. These correspond to calibration data for the CO and CO_2 detectors, respectively.

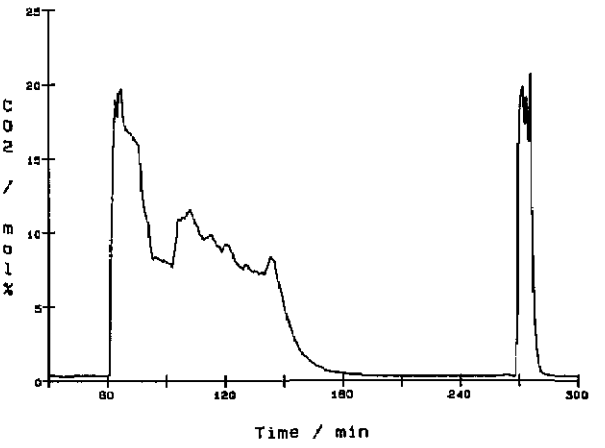

Figure 8. Plot of mole percent CO_2 data as a function of experiment time. The sample burned during the combustion experiment was municipal solid waste with 5% added lime. The sample was ignited at minute 61 and burned until minute 190. The peak at minute 275 was caused by a 20 mol% carbon dioxide reference gas used to calibrate the detector.

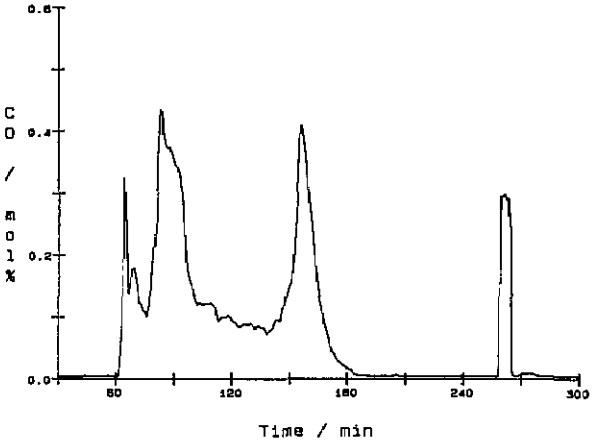

Figure 9. Plot of mole percent CO data as a function of experiment time. The sample burned during the combustion experiment was municipal solid waste with 5% added lime. The peak at minute 260 was caused by a 0.3 mol% carbon monoxide reference gas used to calibrate the detector.

Figure 10 shows the combustor wall temperature at a point near the burning sample. The wall reached nearly 500 °C for a good part of the burn. This is not quite the 600 °C we desire during a combustion experiment but well below the 900 °C critical temperature where the combustor can be damaged. The break in the curve at 202 minutes is due to the cooling gas circulated around the combustor after the burn. The temperature drops slowly to a level where the combustor can be disassembled.

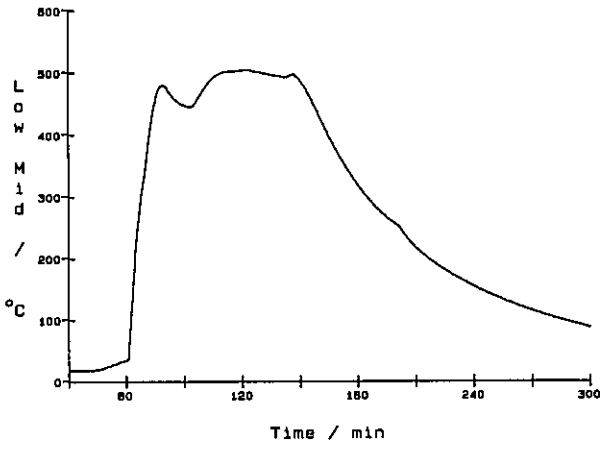

Figure 10. Plot of the combustor wall temperature, approximately 40 cm away from the sample, as a function of experiment time. The sample burned during the combustion experiment was municipal solid waste with 5% added lime.

Summary and Conclusions

Our data acquisition system has proven itself through real experiments to live up to its design. The hardware provides a versatile foundation for data acquisition. The autoranging capabilities of the DVM's compensate for differences in signal level while the scanners provide plenty of room for expansion. The modular form of the data acquisition software has enabled us to modify the program with a minimum amount of trouble and debugging. The data tables are easy to modify and let us change the recording and displaying of data to suit the needs of our experiments. The tabular form of the recorded data makes it easy to manipulate and export to other computers for further analysis.

Acknowledgments

We thank the U.S. Department of Energy's Biofuels and Municipal Waste Technology Division and the NBS Chemical Thermodynamics Division for the financial resources that made this project possible. We also thank our coworkers for their invaluable assistance: E. S. Domalski supervised the project, K. C. Churney defined the calculations and critical experiment parameters, A. E. Ledford, Jr. constructed the calorimeter/combustor, M. L. Reilly developed the multichannel data recording technique, S. S. Bruce assisted in the execution of experiments, and R. Metz, S. S. Sung, and R. Lamdan aided in various aspects of software development and data reduction.

Glossary

ASCII: Derived from the American Standard Code for Information Interchange. A seven- or eight-bit code used to represent alphanumeric characters.

BASIC: Derived from Beginners All-purpose Symbolic Instruction Code. A high-level programming language with a small repertoire of commands and a simple syntax. Fluke BASIC has an expanded instruction set for instrument control and other enhanced features.

Driver: a small program that controls external devices or interrupts.

Flag: any of various types of indications used for identification that signifies the occurrence of some condition.

Foreground: a program or process of high priority that utilizes machine facilities as needed with less critical, background, work performed in the otherwise unused time.

FORTRAN: Derived from formula translator. A high-level language used mostly for scientific or algebraic applications.

Interrupt: to stop a running program in such a way that it can be resumed at a later time, and in the meanwhile permit some other action to be performed.

Modular programming: the construction of a computer program from a collection of modules, each of workable size, whose interactions are rigidly restricted.

Module: a distinct and identifiable unit of a computer program dedicated to a particular process.

Multiprogramming: the interleaved execution of two or more programs by a computer, in which the central processing unit executes a few instructions from each program in succession.

Overlay: a technique for bringing routines into high-speed storage from some other means of storage during processing, so that several routines will occupy the same storage location at different times; an overlay is used when the total storage requirements for instructions exceed the available main storage.

Pascal: a high-level language which emphasizes structured programming.

Process: a set of instructions, data, and control information capable of being executed by the central processing unit of a computer in order to accomplish some purpose; in a multiprogramming environment, processes compete with one another for control of the central processing unit.

RAM: random-access memory.

Scheduling mechanism: a systematic method of determining the order in which processes will be performed by a computer system.

Structured programming: the use of program design and documentation techniques that impose a uniform structure on all computer programs. In another sense, it is an approach to programming in which only three constructs are employed for governing flow of control through the program. These three constructs allow for sequential, conditional, and iterative control flow.

True subroutine: a section of computer software which may be developed separately from the calling program, have parameters exchanged between it and the calling routine, and have local variables not accessible from the other program segments.

Virtual memory: a combination of primary and mass storage memories that can be treated as a single memory by programmers because the computer itself translates a program or virtual address to the actual hardware address.

About the authors: Tom Buckley is a research chemist working with the Large-Sample Combustion Calorimetry Group in the Chemical Thermodynamics Division at the National Bureau of Standards. Hans Rukkers is now a research computer scientist working with the Expert Systems Research Group at the Dutch Center for Mathematics and Computer Science, The Netherlands.

References

[1] Ledford, A. E., Ryan, R. V., Reilly, M. L., Domalski, E. S., and Churney, K. L., Resources and Conservation **8**, 159 (1982).
[2] Churney, K. L., Domalski, E. S., Ledford, A. E., Jr., Colbert, J. C., Bruce, S. S., Paule, R. C., and Reilly, M. L., Proc. of Twelfth Biennial Conf. on Waste Processing, Denver, CO, June 1–4, 449 (1986).
[3] Domalski, E. S., Churney, K. L., Ledford, A. E., Jr., Colbert, J. C., Bruce, S. S., Buckley, T. J., Paule, R. C., and Reilly, M. L., Energy from Municipal Waste Research, Workshop Proceedings, Kissemmee, FL, Feb. 22–24, 29 (1984).
[4] Domalski, E. S., Churney, K. L., Ledford, A. E., Jr., Bruce, S. S., Buckley, T. J., Parris, R. M., and Chesler, S. N., Proceedings of the EPRI seminar on MSW as a Utility Fuel, Madison, WI, Nov. 20 (1985).
[5] Domalski, E. S., Churney, K. L., Ledford, A. E., Jr., Bruce, S. S., Buckley, T. J., Parris, R. M., Chesler, S. N., Chemosphere **15**, 1355 (1986).
[6] Churney, K. L., Ledford, A. E., Jr., Reilly, M. L., and Domalski, E. S., J. Res. Natl. Bur. Stand. **91**, 277 (1986).
[7] Westrum, E. F., Jr., NATO ASI Ser., Ser. C, **119**, 745 (1984).
[8] Flowmeter, Tylan model FC-262 mass flow controller.
[9] Flowmeter, Wallace and Tiernan Varea-meter electronic transmitter.
[10] Oxygen analyzer, Datatest model 303.
[11] Thermometer, Hewlett Packard quartz crystal thermometer model HP18112A with an external oscillator model HP18107A.
[12[Hydrocarbon analyzer, Beckman model 402.
[13] Flowmeter, Ramapo model Mark X.
[14] Humidity analyzer, EG&G model 911.
[15] CO detector, Foxborro Miran II process infrared analyzer; Lira model 300 infrared gas analyzer. CO_2 detector, Foxborro Miran IA infrared analyzer; Lira model 300 infrared gas analyzer.
[16] Infrared spectrometer, Foxborro Miran 80.
[17] Pressure, Sentra model 304B absolute manometer.
[18] Pressure, Sentra model 304B differential manometer.
[19] Oxygen analyzer, Ametek Thermox model WDG III.

[20] Hewlett Packard Scanner model HP3495A, with options 001, 002, and 004. Wavetek model 601 Signal Switching System with model 615 relay cards.
[21] Voltmeter, Hewlett Packard model HP3455A; Fluke model 8840A.
[22] Counter, Hewlett Packard model HP5328A universal counter.
[23] Fluke model 1722A instrument controller.
[24] Gallagher, P. K., Thermochem. Acta **90**, 115 (1985).
[25] Dijkstra, E. W., Commun. ACM15 **10**, 859 (1972).
[26] Dahl, O. J., Dijkstra, E. W., and Hoare, C. A. R., Structured Programming, Academic Press, London (1972).
[27] McGowan, K., and Kelly, J. R., Top-down Structured Programming Techniques, Petrocelli/Charter, New York (1975).
[28] Muxworthy, D. T., ed., Programming for Software Sharing, D. Reidel Publishing Company, Hingham (1983).
[29] Andrews, G. R., and Schneider, F. B., Concepts and Notations for Concurrent Programming, ACM Computing Surveys **15** (1983).
[30] Dijkstra, E. W., Cooperating Sequential Processes, in Programming Languages, F. Genuys, ed., Academic Press, New York, 264 (1968).
[31] Lehmann, D., Pnueli, A., and Stavi, J., Impartiality Justice and Fairness: The Ethics of Concurrent Termination, Automata, Languages and Programming, Lecture Notes in Computer Science **115**, Springer-Verlag, New York, 264-277 (1981).
[32] Dennis, J. B., and Van Horn, E. C., Commun. ACM **9**, 143 (1966).

Volume 93, Number 2, March–April 1988
Journal of Research of the National Bureau of Standards

Partitioning of Alkylbenzenes and Aliphatic Alcohols between Hexadecane and Methanol-Water Mixtures

Volume 93 Number 2 March–April 1988

Michele (Miller) Schantz

National Bureau of Standards
Gaithersburg, MD 20899, and
Georgetown University
Washington, DC 20057

B. N. Barman

Georgetown University
Washington, DC 20057, and
University of Utah
Salt Lake City, UT 84112

and

Daniel E. Martire

Georgetown University
Washington, DC 20057

Partition coefficients between *n*-hexadecane and methanol-water mixtures are reported and analyzed for a series of alkylbenzenes and aliphatic alcohols. A custom-designed flask which has a side arm attached near the bottom was used for the measurements. The hexadecane layer was sampled from the top of the flask, and the aqueous layer was sampled through the side arm of the flask. Both phases were analyzed by an appropriate analytical technique, either gas or liquid chromatography, to determine concentrations. A lattice-model theory suggests a correlation between the hexadecane/methanol-water partition coefficients and the solute molar volume for each solute group type and between the hexadecane/methanol-water partition coefficients and the volume fraction of water in the aqueous phase. The mole-fraction-based activity coefficients calculated from the partition coefficients compare favorably to those determined by a headspace gas chromatographic method. Finally, based upon the data contained herein, the retention mechanism in reversed phase liquid chromatography appears to involve the stationary phase as more than just a passive receptor.

Key words: activity coefficients; alcohols; alkylbenzenes; hexadecane; methanol-water mixtures; partition coefficients; reversed phase liquid chromatography.

Accepted: November 25, 1987

1. Introduction

Partition coefficients have been measured or estimated for a large number of solutes in an octanol/water system [1]. Recently, the partition coefficients between *n*-hexadecane and water were reported for a series of *n*-alkylbenzenes, *n*-alkanes, *n*-1-alkenes, *n*-1-bromoalkanes, and *n*-1-alcohols [2]. For this paper, the partitioning of *n*-alkylbenzenes and 1-alcohols between hexadecane and methanol-water mixtures was studied in an effort to relate this partitioning to retention in reversed phase liquid chromatography (RPLC).

RPLC involves the distribution of a nonpolar or moderately polar solute between a polar mobile phase (the eluent) and a relatively nonpolar stationary phase [3]. The stationary phase is made up of silica gel particles to which *n*-alkyl chains (often, *n*-octadecyl) have been bound. The most common eluents are generally not pure solvents, but rather mixtures of an organic solvent (often, methanol or acetonitrile) and water. When methanol and water are mixed, the solvent properties change [4]. For example, with an increasing percent of methanol in water, the viscosity first increases and then decreases, reaching a maximum at approximately

35% (v/v) methanol in water. The dielectric constant decreases in an almost linear fashion, and the surface tension decreases more rapidly between 0 and 20% (v/v) methanol in water than between 20 and 100% methanol in water.

It has been argued that mobile phase interactions are of principal importance in the control of solute retention, with the nonpolar stationary phase acting mainly as a passive solute acceptor [5]. Many workers in the field (e.g., [6]–[8]) have measured RPLC capacity factors (k') as a function of the volume fraction of organic solvent in water. The capacity factor (k') is given by

$$k' = (t_r - t_0)/t_0, \tag{1}$$

where t_r is the retention time of the solute of interest and t_0 is the retention time of an "unretained solute." The net retention volume, V_n, also has been correlated with the volume fraction of water in the mobile phase [9]. Most of these studies attribute the changes in retention with a change in volume fraction solely to mobile-phase effects.

In the present study, solute partition coefficients have been determined between *n*-hexadecane and methanol-water mixtures for a series of alkylbenzenes and 1-alcohols. In addition, the mutual solubility between hexadecane and methanol has been investigated at 25 °C. Previous partition coefficient measurements done in this laboratory have utilized a generator column attached to an extractor column, a short column packed with C18 material [2]. Since the methanol contained in the aqueous phase would strip the solute from an extractor column, a sit-flask technique similar to that reported by Polak and Lu [10] was used for the present study. The flask had a side arm attached near the bottom which permitted sampling of the aqueous phase without contaminating the syringe with the hexadecane phase. The flask sat undisturbed for 7 days at room temperature, 23 °C. Both phases were analyzed by an appropriate analytical technique, either gas or liquid chromatography. The partition coefficient is the ratio of the concentration in the hexadecane phase to that in the aqueous phase.

As for the hexadecane/water partition coefficient [2], a lattice-model theory suggests a correlation between the hexadecane/methanol-water partition coefficients and the solute molar volume for each solute group type. Using this lattice-model theory, an expression is obtained that relates the hexadecane/methanol-water partition coefficients to the volume fraction of water in the aqueous phase. Finally, the partition coefficients are used in conjunction with chromatographic data to examine the retention mechanism in RPLC.

2. Background Thermodynamics

In this treatment, the solute is designated as component a, water as component b, methanol as component b′, and hexadecane as component h. Hence, the partition coefficient of a solute between hexadecane and methanol-water mixtures is denoted by $K_{h/\%w}$ or $K_{a(h/b'+b)}$. In addition, the volume fraction of water in the methanol-water mixtures is denoted by θ_b, and that of methanol by $\theta_{b'}$. The partition coefficient between hexadecane and methanol-water mixtures is then defined by

$$\ln K_{h/\%w} = \ln K_{a(h/b'+b)} = \ln \gamma_{a(b'+b)} - \ln \gamma_{a(h)}, \tag{2}$$

where γ_a is the volume-fraction-based infinite-dilution solute activity coefficient, with the convention that $\gamma_a \to 1$ as $\theta_a \to 1$, where θ_a is the volume fraction of the solute. Note that eq (2) is analogous to equations for the octanol/water and hexadecane/water partition coefficients [11].

From the Flory-Huggins theory, which is based on a random-mixing (Bragg-Williams) approximation, the solute activity coefficients in water, methanol, and hexadecane are given by [12]

$$\ln \gamma_{a(b)} = [1 - (r_a/r_b)] + r_a X_{ab} \tag{3}$$

$$\ln \gamma_{a(b')} = [1 - (r_a/r_{b'})] + r_a X_{ab'} \tag{4}$$

$$\ln \gamma_{a(h)} = [1 - (r_a/r_h)] + r_a X_{ah} \tag{5}$$

In these equations, r_i is the total number of segments in a molecule of component i which is proportional to V_i^*, the molar volume of component i. Furthermore, X_{ij} is the segmental interaction parameter. In the mixed solvent (b+b′), the solute activity coefficient is given by [3]

$$\ln \gamma_{a(b+b')} = \theta_b \ln \gamma_{a(b)} + \theta_{b'} \ln \gamma_{a(b')} - r_a \theta_b \theta_{b'} X_{bb'} \tag{6}$$

Substituting eqs (3) and (4) into eq (6) and coupling that result with a substitution of eq (5) into eq (2), one obtains

$$\ln K_{a(h/b+b')} = r_a(1/r_h - 1/r_{b'})\theta_{b'} + r_a(1/r_h - 1/r_b)\theta_b + r_a(X_{ab'} - X_{ah})\theta_{b'} + r_a(X_{ab} - X_{ah})\theta_b - r_a X_{b'b} \theta_{b'} \theta_b. \tag{7}$$

By definition, the solute, component a, is composed of group type 1, the methyl and methylene groups and group type 2, the substituent group. Water, component b, is composed of group type 3, and methanol, component b′, is composed of group type 3′. Hexadecane, component h, is composed of group type 1, the methyl and methylene groups. Expanding eqs (3), (4), and (5) to include the group types and substituting the results into eq (7), the hexadecane/methanol-water partition coefficient is now given by

$$\begin{aligned}\ln K_{a(h/b'+b)} &= r_{1a}[X_{13'}+1/r_h-1/r_{b'}]\theta_{b'}\\ &+r_{2a}[X_{23'}-X_{12}+1/r_h-1/r_{b'}]\theta_{b'}\\ &+r_{1a}[X_{13}+1/r_h-1/r_b]\theta_b\\ &+r_{2a}[X_{23}-X_{12}+1/r_h-1/r_b]\theta_b\\ &-r_{1a}X_{33'}\theta_{b'}\theta_b-r_{2a}X_{33'}\theta_{b'}\theta_b \qquad (8)\end{aligned}$$

where r_{ia} is the number of segments of group type i in the solute molecule ($r_a=r_{1a}+r_{2a}$) and where X_{ij} is now a group interaction parameter per unit segment.

Knowing the hexadecane/methanol-water partition coefficient at a limited number of volume fractions of water in methanol, θ_b, it is convenient to be able to predict the partition coefficients at other values of θ_b. Neglecting terms involving the product $\theta_b\theta_{b'}$ ($X_{33'}\approx 0$) and noting that $\theta_b+\theta_{b'}=1$, eq (8) becomes

$$\begin{aligned}\ln K_{a(h/b+b')} &\approx r_{1a}[X_{13'}+1/r_h-1/r_{b'}]\\ &+r_{2a}[X_{23'}-X_{12}+1/r_h-1/r_{b'}]\\ &+r_{1a}[X_{13}-X_{13'}+1/r_{b'}-1/r_b]\theta_b\\ &+r_{2a}[X_{23}-X_{23'}+1/r_{b'}-1/r_b]\theta_b \qquad (9)\end{aligned}$$

Therefore, a plot of $\ln K_{a(h/b+b')}$ versus θ_b would yield a straight line with a slope of $r_{1a}[X_{13}-X_{13'}+1/r_{b'}-1/r_b]+r_{2a}[X_{23}-X_{23'}+1/r_{b'}-1/r_b]$ and an intercept of $r_{1a}[X_{13'}+1/r_h-1/r_{b'}]+r_{2a}[X_{23'}-X_{12}+1/r_h-1/r_{b'}]$.

It is also convenient to correlate the $K_{a(h/b+b')}$ at a particular θ_b with the molar volume of the solute V_a^*. In other words, if one knows the $K_{a(h/b+b')}$ for several members of a solute series at a particular θ_b, one may wish to predict that partition coefficient for another member of that series, knowing its molar volume. Using eq (9) with $r_{1a}=r_a-r_{2a}$, one finds that

$$\begin{aligned}\ln K_{a(h/b+b')} &\approx r_a[X_{13'}+1/r_h-1/r_{b'}]\\ &+r_{2a}[X_{23'}-X_{12}-X_{13'}]\\ &+r_a[X_{13}-X_{13'}+1/r_{b'}-1/r_b]\theta_b\\ &+r_{2a}[X_{23}-X_{23'}-X_{13}+X_{13'}]\theta_b. \qquad (10)\end{aligned}$$

However, r_a is proportional to V_a^*, the molar volume of the solute and r_{2a} is proportional to V_{2a}^*, the molar volume of the solute functional group. The partition coefficient can now be rewritten as

$$\begin{aligned}\ln K_{a(h/b+b')} &= CV_a^*[X_{13'}+1/r_h-1/r_{b'}]\\ &+CV_a^*[X_{13}-X_{13'}+1/r_{b'}-1/r_b]\theta_b\\ &+CV_{2a}^*[X_{23'}-X_{12}-X_{13'}]\\ &+CV_{2a}^*[X_{23}-X_{23'}-X_{13}+X_{13'}]\theta_b, \qquad (11)\end{aligned}$$

where C is a constant. This equation predicts a linear relationship between $\ln K_{a(h/b+b')}$ and V_a^*, where the slope is $C[X_{13'}+1/r_h-1/r_b]+C[X_{13}-X_{13'}+1/r_{b'}-1/r_b]\theta_b$ and the intercept is $CV_{2a}^*[X_{23'}-X_{12}-X_{13'}]+CV_{2a}^*[X_{23}-X_{23'}-X_{13}+X_{13'}]\theta_b$. Therefore, according to eq (11), at a given θ_b the slope should be independent of the solute functional group, whereas, the intercept should reflect the size and interactions of the functional group. Similar linear relationships between the octanol/water partition coefficient, $K_{o/w}$, and V_a^*, as well as the hexadecane/water partition coefficient, $K_{h/w}$, and V_a^*, were discussed in a previous paper [2].

3. Experimental

A sit flask was used for the partition coefficient measurements. The solute was quantitatively added to the hexadecane phase. The aqueous layer was placed at the bottom of a flask containing a side arm. The hexadecane-solute mixture was also added to the flask. This flask was then allowed to sit in a room kept at 23 °C without stirring for at least 7 days [10]. The propylbenzene in hexadecane/100% methanol partition coefficient ($K_{h/0\%w}$) was used as the test system. Samples of both layers were removed and analyzed after 3, 5, 7, 9, and 11 days of sitting. The $K_{h/0\%w}$ value was constant within experimental error from day 7 to day 11.

Both phases were analyzed by an appropriate analytical method, either gas or liquid chromatography. The hexadecane layer was sampled through the top of the sit flask while the aqueous layer was sampled through the side arm.

4. Results and Discussion

The mole fraction of methanol in *n*-hexadecane at 25 °C is 3×10^{-3} mole hexadecane per total number of moles in the methanol phase, and the mole fraction of *n*-hexadecane in methanol at 25 °C is 4.25×10^{-2} mole methanol per total number of moles in the hexadecane phase. The results for the partition coefficients between hexadecane and methanol-water mixtures are given in tables 1, 2, and 3 for the alcohols, benzene, and alkylbenzenes, respectively. The data revealed some dependence of the partition coefficient between hexadecane and methanol-water mixtures on concentration of the alcohol in the hexadecane phase for the alcohols studied. Riebesehl and Tomlinson [13] noted that, although alcohols tend to self-associate in nonaqueous solution, association below 10^{-2} mol/L is extremely small. Backlund et al. [14] measured the partition coefficients of alcohols between octane and alcohol-water mixtures. They noted a concentration dependence of the partition coefficient indicating self-association of the alcohols in the octane phase. In the case of the alkylbenzenes, a clear dependence on concentration was found for the partition coefficients, especially between hexadecane and 100% methanol ($K_{h/0\%w}$), suggesting aggregation effects. As Karickhoff and Brown [15] suggested, the monomer partition coefficient is determined by reducing the solute concentration below the aggregation threshold concentration, experimentally determined by consecutive dilutions. Association generally tends to raise the partition coefficient, and dissociation tends to lower the partition coefficient [16]. In the case of benzene and the alkylbenzenes, with increasing aromatic concentration in the hexadecane phase, the hexadecane/methanol partition coefficient first increases. For the alkylbenzenes, the $K_{h/0\%w}$ levels off at this point. For benzene, however, $K_{h/0\%w}$ next reaches a minimum and then increases again. In all cases (alcohols, benzene, and alkylbenzenes), the lowest value of $K_{h/0\%w}$ determined was taken as the "true" value.

There are only three sets of literature values of any similarity to those reported here, two of which are those of Krustulovic et al. [17] and Lochmuller and Wilder [18] who determined the liquid-liquid extraction between *n*-hexadecane and a 90% acetonitrile in water mixture for hexane and octane or a 50% methanol in water mixture for benzene and toluene, respectively. They determined the relative partition coefficients in the hexadecane layer, log α, however. The other set are preliminary data of Hussam and Carr [19] who determined the infinite dilution activity coefficients of benzene, toluene, ethylbenzene, *n*-propylbenzene, and *n*-butylbenzene in methanol-water mixtures at 30 °C by a headspace gas chromatographic method. They studied solutes at concentrations as low as 10^{-6}

Table 1. Dependence of the hexadecane/methanol-water partition coefficient on concentration in hexadecane and percent methanol in the aqueous phase for the alcohols

Compound	100% H_2O		80% H_2O		50% H_2O		20% H_2O		0% H_2O	
	[in C_{16}](M)	ln $K_{h/100\%w}$[a]	[in C_{16}](M)	ln $K_{h/80\%w}$[a]	[in C_{16}](M)	ln $K_{h/50\%w}$[a]	[in C_{16}](M)	ln $K_{h/20\%w}$[a]	[in C_{16}](M)	ln $K_{h/0\%w}$[a]
1-Butanol	1.04×10^{-1}	−2.22±0.09	1.29×10^{-1}	−2.56±0.01	0.69×10^{-1}	−2.95±0.06	0.69×10^{-1}	−4.05±0.10	1.19×10^{-1}	−4.51±0.01
	0.16×10^{-1}	−2.21±0.06	0.16×10^{-1}	−2.55±0.02	0.16×10^{-1}	−3.18±0.08	0.16×10^{-1}	−4.04±0.05	0.16×10^{-1}	−4.52±0.04
1-Pentanol	1.20×10^{-1}	−0.07±0.01	1.13×10^{-1}	−1.16±0.02	0.59×10^{-1}	−2.17±0.02	0.59×10^{-1}	−3.32±0.06	0.59×10^{-1}	−4.19±0.02
	0.12×10^{-1}	−0.71±0.03	0.12×10^{-1}	−1.16±0.03	0.12×10^{-1}	−2.19±0.05	0.12×10^{-1}	−3.32±0.04	0.12×10^{-1}	−4.18±0.06
1-Hexanol	0.67×10^{-1}	1.23±0.01	1.11×10^{-1}	−0.77±0.01	0.87×10^{-1}	−1.20±0.04	0.87×10^{-1}	−2.23±0.07	0.87×10^{-1}	−3.38±0.07
	0.40×10^{-1}	1.23±0.03	0.40×10^{-1}	−0.08±0.01	0.40×10^{-1}	−1.21±0.03	0.40×10^{-1}	−2.62±0.05	0.40×10^{-1}	−3.88±0.02
			0.15×10^{-1}	−0.07±0.01			0.15×10^{-1}	−2.64±0.03	0.15×10^{-1}	−3.85±0.05
1-Heptanol	0.46×10^{-1}	2.53±0.08	1.27×10^{-1}	1.97±0.09	1.17×10^{-1}	−0.75±0.01	1.17×10^{-1}	−2.62±0.08	1.17×10^{-1}	−3.34±0.01
	0.16×10^{-1}	2.51±0.03	0.16×10^{-1}	1.46±0.02	0.16×10^{-1}	−0.24±0.01	0.16×10^{-1}	−2.23±0.04	0.16×10^{-1}	−3.34±0.05
			0.06×10^{-1}	1.45±0.05	0.06×10^{-1}	−0.21±0.02	0.06×10^{-1}	−2.24±0.02		
1-Octanol	0.90×10^{-1}	4.42±0.01	1.03×10^{-1}	2.17±0.02	0.91×10^{-1}	1.02±0.02	0.91×10^{-1}	−2.07±0.01	1.03×10^{-1}	−2.58±0.05
	0.16×10^{-1}	4.40±0.04	0.16×10^{-1}	2.67±0.03	0.16×10^{-1}	0.62±0.01	0.16×10^{-1}	−1.40±0.02	0.16×10^{-1}	−2.95±0.04
			0.05×10^{-1}	2.69±0.03	0.05×10^{-1}	0.63±0.02	0.05×10^{-1}	−1.39±0.04	0.05×10^{-1}	−2.91±0.05
1-Nonanol	0.57×10^{-1}	6.29±0.01	0.96×10^{-1}	3.59±0.09	1.22×10^{-1}	1.98±0.02	1.22×10^{-1}	−1.46±0.03	0.96×10^{-1}	−2.58±0.09
	0.09×10^{-1}	6.28±0.02	0.09×10^{-1}	4.29±0.05	0.09×10^{-1}	1.57±0.01	0.09×10^{-1}	−1.04±0.02	0.09×10^{-1}	−2.59±0.05
			0.06×10^{-1}	4.31±0.04	0.06×10^{-1}	1.56±0.02	0.06×10^{-1}	−1.04±0.03		

[a] The uncertainty is the standard deviation of the mean for three replicate measurements.

Table 2. Dependence of the hexadecane/methanol-water partition coefficient ($K_{h/\%w}$) on concentration in hexadecane and percent methanol in the aqueous phase for benzene

% H_2O	[Benzene in C_{16}](M)	ln $K_{h/\%w}$[a]
100	9.90×10^{-2}	4.77±0.01
80	9.29×10^{-2}	4.21±0.01
	0.02×10^{-2}	3.99±0.05
50	9.29×10^{-2}	2.72±0.01
	1.35×10^{-2}	3.10±0.04
	1.14×10^{-2}	2.65±0.03
	0.99×10^{-2}	2.34±0.02
	0.02×10^{-2}	2.37±0.05
40	0.99×10^{-2}	1.84±0.02
30	0.99×10^{-2}	1.46±0.02
20	9.29×10^{-2}	1.10±0.02
	0.99×10^{-2}	0.99±0.02
	0.02×10^{-2}	0.82±0.01
10	0.99×10^{-2}	0.41±0.01
0	9.29×10^{-2}	−0.41±0.01
	6.88×10^{-2}	−0.78±0.01
	2.36×10^{-2}	−1.05±0.02
	0.97×10^{-2}	−0.42±0.01
	0.64×10^{-2}	−0.27±0.02
	0.24×10^{-2}	−0.08±0.01
	0.23×10^{-2}	−0.09±0.01
	0.21×10^{-2}	−0.10±0.02
	0.13×10^{-2}	−0.11±0.01
	0.11×10^{-2}	−0.07±0.01
	0.10×10^{-2}	−0.07±0.01
	0.03×10^{-2}	−0.13±0.01
	0.01×10^{-2}	−0.16±0.01

[a] The uncertainty is the standard deviation of the mean for three replicate measurements.

mole fraction up to 10^{-3} mole fraction to insure that solute self-association was negligible. The polynomial equations obtained from their data relating the mole-fraction-based activity coefficients to the mole fraction of water in methanol are given in table 4.

Table 4. Coefficients determined from regression analysis of the data of Hussam and Carr [19], according to the form[a], ln $\gamma_{a,x}=A+Bx_b+Cx_b^2+Dx_b^3$

Solute	A	B	C	D
Benzene	1.9767	2.9411	1.3497	1.4030
Toluene	2.2962	3.0698	2.9367	3.7922×10^{-3}
Ethylbenzene	2.5489	3.7923	1.8357	1.7573
n-Propylbenzene	2.8088	4.2765	2.4203	1.2938
n-Butylbenzene	3.0462	5.0907	1.7578	2.3608

[a] ln $\gamma_{a,x}$ is the mole-fraction-based activity coefficient of the solute a, and x_b is the mole fraction of water in the water-methanol mixture.

In a previous publication [2], the volume-fraction-based activity coefficients in hexadecane as determined from a gas-liquid chromatographic experiment are reported. Using the relationships for activity (a) of a solute, one can relate the activity coefficient on a volume-fraction basis ($\gamma_{a,\theta}$) to that on a mole-fraction basis ($\gamma_{a,x}$), i.e.

$$a=\gamma_{a,\theta}\theta_a=\gamma_{a,x}x_a, \tag{12}$$

Table 3. Dependence of the hexadecane/methanol-water partition coefficients on concentration in hexadecane and percent methanol in the aqueous phase for biphenyl and the alkylbenzenes

Compound	100% H_2O		80% H_2O		50% H_2O		20% H_2O		0% H_2O	
	[in C_{16}](M)	ln $K_{h/100\%w}$[a]	[in C_{16}](M)	ln $K_{h/80\%w}$[a]	[in C_{16}](M)	ln $K_{h/50\%w}$[a]	[in C_{16}](M)	ln $K_{h/20\%w}$[a]	[in C_{16}](M)	ln $K_{h/0\%w}$[a]
Biphenyl	3.91×10^{-2}	9.65±0.02	3.91×10^{-2}	8.43±0.07	3.91×10^{-2}	5.57±0.04	3.91×10^{-2}	3.06±0.01	3.91×10^{-2}	0.53±0.01
Toluene	11.1×10^{-2}	6.24±0.01	9.61×10^{-2}	4.67±0.09	9.61×10^{-2}	3.66±0.02	9.61×10^{-2}	1.85±0.01	9.61×10^{-2}	0.29±0.01
			0.02×10^{-2}	5.01±0.10	0.02×10^{-2}	3.29±0.08	0.02×10^{-2}	1.49±0.03	0.67×10^{-2}	0.31±0.01
									0.50×10^{-2}	0.30±0.01
									0.33×10^{-2}	0.29±0.01
Ethylbenzene	14.2×10^{-2}	7.41±0.01	12.8×10^{-2}	6.19±0.04	12.8×10^{-2}	4.35±0.01	12.8×10^{-2}	2.42±0.05	12.8×10^{-2}	0.48±0.01
			0.02×10^{-2}	5.98±0.07	0.02×10^{-2}	4.01±0.07	0.02×10^{-2}	1.93±0.03	0.87×10^{-2}	0.45±0.01
									0.72×10^{-2}	0.40±0.01
									0.46×10^{-2}	0.39±0.01
n-Propylbenzene	11.2×10^{-2}	8.82±0.01	2.08×10^{-2}	6.68±0.04	6.71×10^{-2}	4.97±0.08	6.71×10^{-2}	2.90±0.04	6.71×10^{-2}	1.07±0.02
			0.01×10^{-2}	7.15±0.06	0.01×10^{-2}	4.86±0.06	0.01×10^{-2}	2.58±0.02	0.87×10^{-2}	0.93±0.01
									0.60×10^{-2}	0.81±0.02
									0.46×10^{-2}	0.80±0.01
n-Butylbenzene	7.55×10^{-2}	10.50±0.03	9.57×10^{-2}	8.04±0.02	9.57×10^{-2}	5.62±0.03	9.57×10^{-2}	3.52±0.05	9.57×10^{-2}	1.50±0.03
			0.01×10^{-2}	8.54±0.09	0.01×10^{-2}	5.78±0.06	0.01×10^{-2}	3.21±0.06	0.81×10^{-2}	1.47±0.03
									0.47×10^{-2}	1.20±0.02
									0.28×10^{-2}	1.14±0.04
n-Pentylbenzene	7.18×10^{-2}	11.61±0.20			7.18×10^{-2}	6.26±0.02			7.18×10^{-2}	1.86±0.08
n-Hexylbenzene	8.67×10^{-2}	12.94±0.41			8.67×10^{-2}	6.98±0.03			8.67×10^{-2}	2.35±0.03

[a] The uncertainty is the standard deviation of the mean for three replicate measurements.

where θ_a and x_a are, respectively, the volume fraction and mole fraction of the solute in solution. From eq (12), it follows that

$$\gamma_{a(h),x} \approx \gamma_{a(h),\theta} (V_a^*/V_h^*) \quad (13)$$

where V_a^* and V_h^* are the molar volumes of the solute and hexadecane, respectively. Using the $\gamma_{a(h),\theta}$ reported previously [2] and eq (13), the $\gamma_{a(h),x}$ are calculated for the alkylbenzene series, benzene through butylbenzene as reported in table 5. From

Table 5. Comparison of activity coefficients determined from partition coefficients (25 °C) and from headspace analysis (30 °C)[a]

0% Water; $x_b=0$

Compound	$\ln K_{h/0\%w}$	$\ln V_{0\%w}/V_h$[b]	$\ln\gamma_{a(h),x}$	$\ln\gamma_{a(0\%w),x}$ Partition	Headspace[a]
Benzene	−0.07	−1.98	0.095	2.07	1.97
Toluene	0.29	−1.98	0.028	2.29	2.29
Ethylbenzene	0.39	−1.98	0.141	2.51	2.55
n-Propylbenzene	0.80	−1.98	0.130	2.91	2.80
n-Butylbenzene	1.14	−1.98	0.132	3.25	3.05

20% Water; $x_b=0.3604$

Compound	$\ln K_{h/20\%w}$	$\ln V_{20\%w}/V_h$[b]	$\ln\gamma_{a(h),x}$	$\ln\gamma_{a(20\%w),x}$ Partition	Headspace[a]
Benzene	0.82	−2.20	0.095	3.12	3.28
Toluene	1.49	−2.20	0.028	3.72	3.78
Ethylbenzene	1.93	−2.20	0.141	4.27	4.24
n-Propylbenzene	2.58	−2.20	0.130	4.91	4.73
n-Butylbenzene	3.21	−2.20	0.132	5.54	5.22

50% Water; $x_b=0.6927$

Compound	$\ln K_{h/50\%w}$	$\ln V_{50\%w}/V_h$[b]	$\ln\gamma_{a(h),x}$	$\ln\gamma_{a(50\%w),x}$ Partition	Headspace[a]
Benzene	2.37	−2.46	0.095	4.93	5.13
Toluene	3.29	−2.46	0.028	5.78	5.83
Ethylbenzene	4.01	−2.46	0.141	6.62	6.64
n-Propylbenzene	4.86	−2.46	0.130	7.45	7.36
n-Butylbenzene	5.78	−2.46	0.132	8.38	8.20

80% Water; $x_b=0.9002$

Compound	$\ln K_{h/80\%w}$	$\ln V_{80\%w}/V_h$[b]	$\ln\gamma_{a(h),x}$	$\ln\gamma_{a(80\%w),x}$ Partition	Headspace[a]
Benzene	3.99	−2.67	0.095	6.76	6.74
Toluene	5.01	−2.67	0.028	7.71	7.44
Ethylbenzene	5.98	−2.67	0.141	8.79	8.73
n-Propylbenzene	7.15	−2.67	0.130	9.95	9.56
n-Butylbenzene	8.54	−2.67	0.132	11.34	10.78

100% Water; $x_b=1.0000$

Compound	$\ln K_{h/100\%w}$	$\ln V_{100\%w}/V_h$[b]	$\ln\gamma_{a(h),x}$	$\ln\gamma_{a(100\%w),x}$ Partition	Solub[c]	Headspace[a]
Benzene	4.77	−2.79	0.095	7.66	7.56	7.67
Toluene	6.24	−2.79	0.028	9.06	9.08	8.31
Ethylbenzene	7.41	−2.79	0.141	10.34	10.37	9.93
n-Propylbenzene	8.82	−2.79	0.130	11.74	11.77	10.80
n-Butylbenzene	10.50	−2.79	0.132	13.42	13.19	12.26

[a] Hussam and Carr [19].
[b] Ratio of molar volumes.
[c] Determined from aqueous solubility [2].

ln $K_{h/\%w}$ and $\gamma_{a(h),x}$, the mole-fraction-based activity coefficients at the corresponding mole fraction of water in methanol are calculated using eq (2) (table 5). Using the equations obtained by fitting Hussam and Carr's data (table 4), the infinite dilution mole-fraction-based activity coefficients were determined at the same mole fractions of water in methanol as in the partitioning experiments. The data are presented in table 5. Note that the agreement between the activity coefficients determined at infinite dilution and from partition coefficients is fairly good. At 100% water, the activity coefficients determined from aqueous solubilities are also given. There is a relatively good agreement among all three activity coefficients for benzene. For *n*-butylbenzene, an extrapolation of Hussam and Carr's data [19] from $x_b=0.53$ to $x_b=1.00$, where x_b denotes the mole fraction of water in the water-methanol mixture, is required to obtain a value at 100% water.

The hexadecane/methanol-water partition coefficient, similar to the hexadecane/water and octanol/water partition coefficients [2], is linearly related to the solute molar volume by eq (11). As can be seen in figures 1 and 2 for the alkylbenzenes and alcohols, respectively, there is a linear relationship between ln $K_{h/\%w}$ and solute molar volume at a particular volume percent for the solutes studied. The volume percents of water in methanol used are 0%, 20%, 50%, 80%, and 100% water in methanol.

In figure 1, equations for each percent of water in methanol are:

$$\ln K_{h/100\%w}=0.0831(\pm0.0018)V_a^*-2.67(\pm0.05),$$

$$r^2=0.999(\pm0.019)$$

$$\ln K_{h/80\%w}=0.0676(\pm0.0009)V_a^*-2.17(\pm0.03),$$

$$r^2=0.995(\pm0.015)$$

$$\ln K_{h/50\%w}=0.0467(\pm0.0011)V_a^*-1.71(\pm0.05),$$

$$r^2=0.996(\pm0.021)$$

$$\ln K_{h/20\%w}=0.0353(\pm0.0009)V_a^*-2.33(\pm0.06),$$

$$r^2=0.997(\pm0.022)$$

$$\ln K_{h/0\%w}=0.0241(\pm0.0008)V_a^*-2.39(\pm0.08),$$

$$r^2=0.956(\pm0.019)$$

Deleting *n*-pentylbenzene and *n*-hexylbenzene,

$$\ln K_{h/0\%w}=0.0716(\pm0.0010)V_a^*-1.66(\pm0.05),$$

$$r^2=0.978(\pm0.021).$$

The values in the parentheses indicate the standard deviation of the slope, intercept, and overall fit, respectively, for each equation.

In figure 2, equations for each percent of water in methanol are:

$$\ln K_{h/100\%w}=0.103(\pm0.004)V_a^*-11.74(\pm0.09),$$

$$r^2=0.998(\pm0.015)$$

$$\ln K_{h/80\%w}=0.082(\pm0.003)V_a^*-10.17(\pm0.10),$$

$$r^2=0.997(\pm0.018)$$

$$\ln K_{h/50\%w}=0.057(\pm0.006)V_a^*-8.40(\pm0.10),$$

$$r^2=0.999(\pm0.017)$$

$$\ln K_{h/20\%w}=0.037(\pm0.004)V_a^*-7.35(\pm0.09),$$

$$r^2=0.991(\pm0.020)$$

$$\ln K_{h/0\%w}=0.024(\pm0.003)V_a^*-6.79(\pm0.08),$$

$$r^2=0.993(\pm0.019).$$

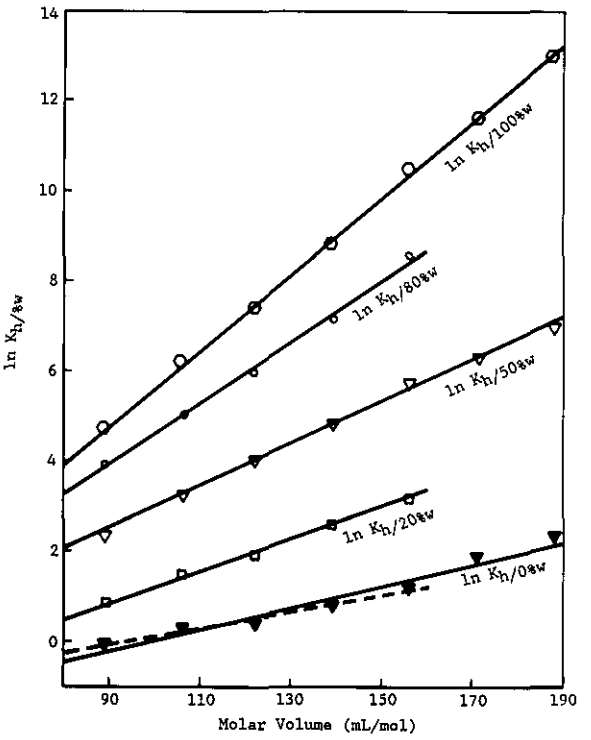

Figure 1. ln $K_{h/\%w}$ versus molar volume for the alkylbenzenes.

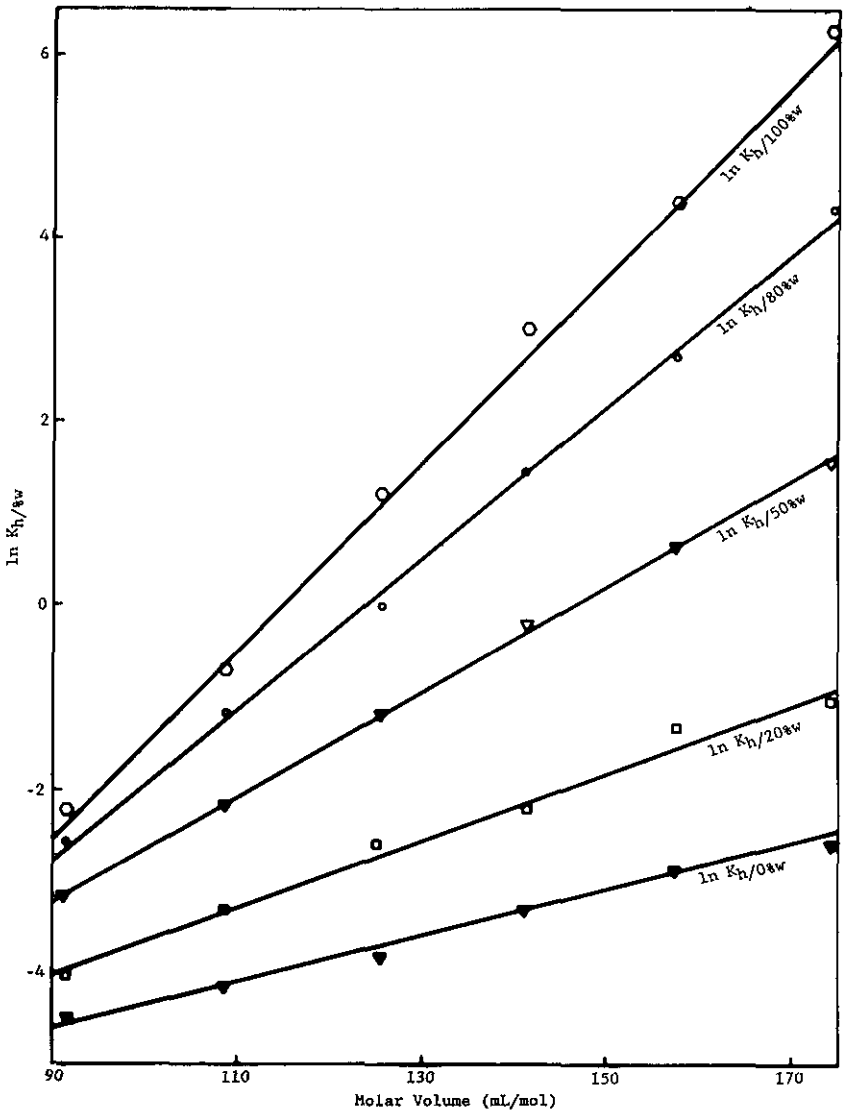

Figure 2. ln $K_{h/\%w}$ versus molar volume for the alcohols.

The worst correlation coefficient is for the alkylbenzene partition coefficients in 100% methanol, where as seen in tables 2 and 3, there is considerable dependence of these values on the concentration of alkylbenzenes in the hexadecane phase, making it difficult to determine the "true" infinite-dilution partition coefficient.

One notes in eq (11) that both the slope and intercept of plots of ln $K_{h/\%w}$ versus V_a* depend on the volume fraction of water in methanol, θ_b. As can be seen in figures 1 and 2, as θ_b increases the slopes increases for a given homologous series. Also, the slopes are approximately the same at a given θ_b for the alkylbenzene and alcohol series. However, the intercepts are highly negative for the alcohols, becoming more so with increasing θ_b, while they are much less negative and essentially independent of θ_b for the alkylbenzenes.

To interpret these trends, let us first examine the dependence of the partition coefficients on θ_b, shown in figures 3 and 4 for the alkylbenzenes and alcohols, respectively.

In figure 3, equations of the lines are:

Benzene $\ln K_{h/\%w} = 4.94(\pm 0.06)\theta_b - 0.09(\pm 0.01)$,

$r^2 = 0.998(\pm 0.021)$

Toluene $\ln K_{h/\%w} = 5.93(\pm 0.08)\theta_b + 0.30(\pm 0.01)$,

$r^2 = 0.999(\pm 0.016)$

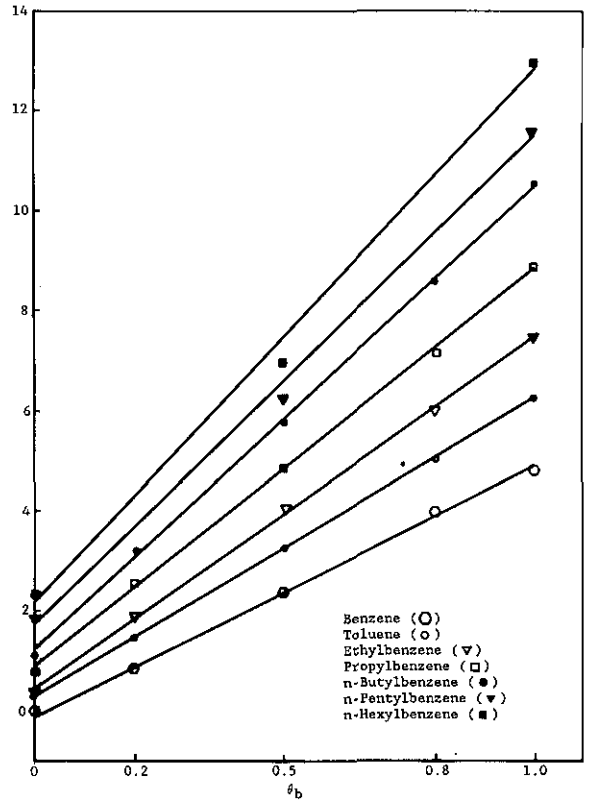

Figure 3. ln $K_{h/\%w}$ versus volume fraction of water in methanol for the alkylbenzenes.

Ethylbenzene $\ln K_{h/\%w}=6.95(\pm0.09)\theta_b$

$+0.47(\pm0.01)$, $r^2=0.999(\pm0.019)$

Propylbenzene $\ln K_{h/\%w}=7.91(\pm0.06)\theta_b$

$+0.89(\pm0.01)$, $r^2=0.999(\pm0.019)$

n-Butylbenzene $\ln K_{h/\%w}=9.23(\pm0.08)\theta_b$

$+1.22(\pm0.02)$, $r^2=0.999(\pm0.021)$

n-Pentylbenzene $\ln K_{h/\%w}=9.75(\pm0.09)\theta_b$

$+1.70(\pm0.02)$, $r^2=0.997(\pm0.024)$

n-Hexylbenzene $\ln K_{h/\%w}=10.59(\pm0.11)\theta_b$

$+2.13(\pm0.03)$, $r^2=0.995(\pm0.022)$.

In figure 4, equations of the lines are:

n-Butanol $\ln K_{h/\%w}=2.36(\pm0.04)\theta_b$

$-4.48(\pm0.06)$, $r^2=0.993(\pm0.021)$

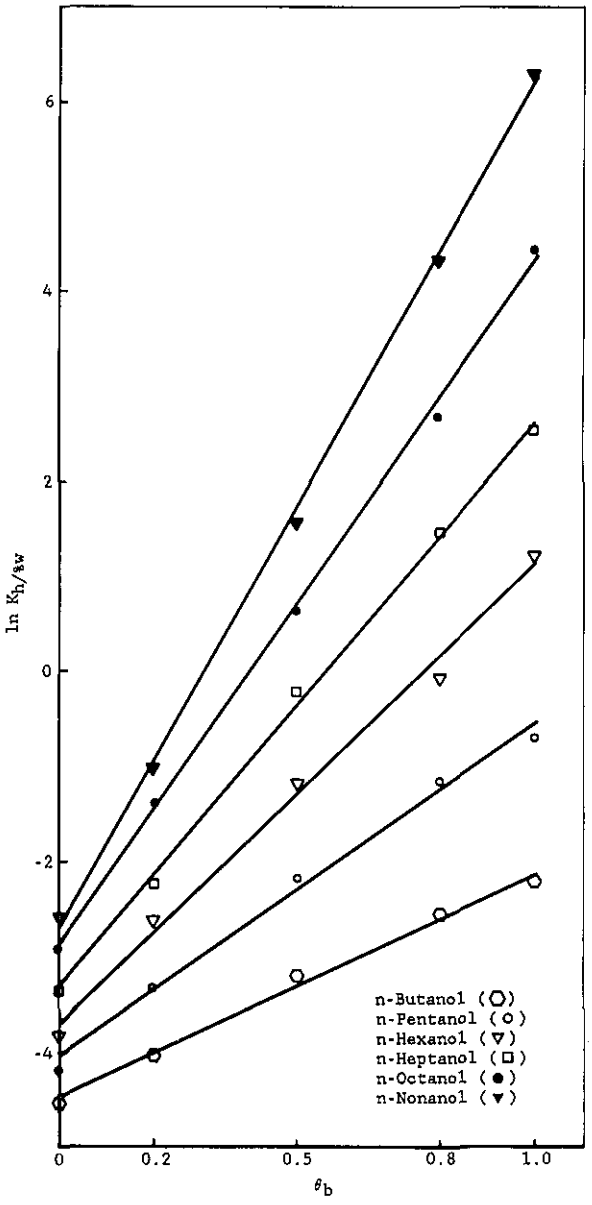

Figure 4. ln $K_{h/\%w}$ versus volume fraction of water in methanol for the alcohols.

n-Pentanol $\ln K_{h/\%w}=3.50(\pm0.05)\theta_b$

$-4.06(\pm0.06)$, $r^2=0.993(\pm0.019)$

n-Hexanol $\ln K_{h/\%w}=4.87(\pm0.07)\theta_b$

$-3.74(\pm0.08)$, $r^2=0.994(\pm0.018)$

n-Heptanol $\ln K_{h/\%w}=5.93(\pm0.06)\theta_b$

$-3.33(\pm0.07)$, $r^2=0.998(\pm0.016)$

n-Octanol $\ln K_{h/\%w}=7.18(\pm0.09)\theta_b9$

$-2.90(\pm 0.08)$, $r^2=0.999(\pm 0.019)$

n-Nonanol $\ln K_{h/\%w}=8.88(\pm 0.08)\theta_b$

$-2.73(\pm 0.06)$, $r^2=0.999(\pm 0.017)$.

Workers [6,8] have studied the dependence of the RPLC capacity factor (k') on the volume fraction of water in methanol. Hennion et al. [6] found a linear relation between $\ln k'$ and θ_b, while other workers [8] contend that these plots are linear for only part of the aqueous volume fraction range. Theoretical justification for a linear relationship between $\ln K_{h/\%w}$ and θ_b is given by eq (9), which reveals that both the intercept and slope depend on r_{1a}, the number of alkyl segments in the solute molecule.

To analyze figures 3 and 4 in terms of eq (9), let us first assign one segment to each methylene group. Accordingly, from relative van der Waals volumes [20], a methyl group would correspond to 1.33 segments, a bound hydrogen atom to approximately 0.33 segments, and a phenyl group to 4.48 segments. Thus, $r_b=1.00$ (water), $r_{b'}=2.00$ (methanol), $r_h=16.67$ (hexadecane), and, for the solutes,

$$\text{alkylbenzenes:}\quad r_a=4.48+(n_a+0.33) \tag{14}$$

$$\text{alcohols:}\quad r_a=0.67+(n_a+0.33), \tag{15}$$

where n_a is the number of carbon atoms in the solute *n*-alkyl chain, $r_{1a}=n_a+0.33$, and r_{2a} is 4.48 and 0.67 for the phenyl and hydroxyl groups, respectively.

Using these assigned volumes and eq (9) a linear least-squares analysis of the coefficients of the θ_b term for alkylbenzenes (fig. 3) as a function of r_{1a} gives $X_{23}-X_{23'}=1.56$ and $X_{13}-X_{13'}=1.45$, with a correlation coefficient of 0.997. These results indicate that, in terms of interaction energetics, both the phenyl group and alkyl groups prefer to dissolve in methanol rather than water. Similarly, analysis of the intercepts of the plots (fig. 3) as a linear function of r_{1a} yields $X_{23'}-X_{12}=0.38$ and $X_{13'}=0.80$ (whence, $X_{13}=2.25$), with a correlation coefficient of 0.994. The former result indicates that, energetically, phenyl groups prefer alkyl groups over water, while the latter result indicates that methanol (and especially water) are not hospitable solvents for alkyl groups. A linear least-squares analysis of the coefficients of the θ_b term for the alcohols (fig. 4) as a function of r_{1a} gives $X_{23}-X_{23'}=-4.41$ and $X_{13}-X_{13'}=1.78$, with a correlation coefficient of 0.998. The former result clearly indicates that, as expected, hydroxyl groups energetically prefer solution in water over solution in methanol. The latter result (already discussed) is somewhat higher than that obtained from analysis of the alkylbenzene plots (1.45); however, in view of the approximate nature of the model and the uncertainty in the experimental data, the agreement is reasonable. Similarly, analysis of the intercepts of the plots (fig. 4) as a linear function of r_{1a} yields $X_{23'}-X_{12}=-8.57$ and $X_{13'}=0.80$ (in full agreement with the alkylbenzene result), with a correlation coefficient of 0.995. The former value reflects the very strong energetic preference of hydroxyl groups for dissolving in methanol, relative to solution in an alkyl-group environment.

Returning to the interpretation of figures 1 and 2, note that all of the molecular parameters in eq (11) have now been assigned (r values) or determined (X values). Inserting these values into eq (11), one obtains for the alkylbenzenes and alcohols, respectively:

$$\ln K_{a(h/b+b')}=V_a^*C[0.36+0.95\theta_b] + V_{2a}^*C[-0.42+0.11\theta_b] \tag{16}$$

$$\ln K_{a(h/b+b')}=V_a^*C[0.36+1.28\theta_b] + V_{2a}^*C[-9.37-6.19\theta_b]. \tag{17}$$

As discussed earlier and as can be seen by comparing eqs (16) and (17), the coefficients of the V_a^* term are approximately the same for the alkylbenzene and alcohol series, and they increase with increasing θ_b, primarily reflecting the unfavorable mixing of alkyl groups with water, relative to their mixing with methanol ($X_{13}-X_{13'}$).

For the alkylbenzenes, the intercepts in figure 1 are negative and are virtually independent of θ_b. This can be understood by examining the V_{2a}^* term in eq (16) in the light of eq (11). The lack of a discernible dependence of these intercepts on θ_b reflects the near cancellation of four X terms in eq (11), i.e., $X_{23}-X_{23'}-X_{13}+X_{13'}\approx 0$. The negative intercepts stem primarily from the relative preference of methanol for phenyl groups over alkyl groups, i.e., $X_{23'}-X_{13}<0$. For the alcohols [eq (17)], the intercepts in figure 2 are highly negative and become even more negative with increasing θ_b. When $\theta_b=0$ (pure methanol), the intercept is proportional to $X_{23'}-X_{12}-X_{13'}$ ($=-9.37$). Clearly, the very negative $X_{23'}-X_{12}$, reflecting the solution preference of hydroxyl groups for methanol rather

than alkyl groups, governs here. With increasing θ_b, both the preference of hydroxyl groups for water over methanol ($X_{23}-X_{23'}=-4.41$) and of alkyl groups for methanol over water ($X_{13'}-X_{13}=-1.78$) lead to more negative intercepts. Note that even though V_{2a}* for the hydroxyl group is smaller than that of the phenyl group by a factor of about 6.7 (from the ratio of r_{2a} values), the coefficient of the V_{2a}* term in eq (17) is more negative by a factor of 22 ($\theta_b=0$) to 50 ($\theta_b=1$) than the corresponding coefficient in eq (16).

Finally, we address the important question as to whether the entire dependence of solute retention on mobile-phase composition can be attributed solely to the mobile phase or whether the stationary-phase contribution varies with mobile-phase composition also. Assuming that in RPLC systems the solute partitions between two "bulk" phases, the net retention volume is given by

$$V_n=K_{a(s/b+b')}C_s, \tag{18}$$

where $K_{a(s/b+b')}$ is the partition coefficient of the solute between the mobile phase and stationary phase and C_s is the capacity of the stationary phase, given here by V_s, the volume. The partition coefficient is the ratio of the volume-fraction-based activity coefficients such that

$$K_{a(s/b+b')}=\gamma_{a(b+b')}/\gamma_{a(s)}, \tag{19}$$

where $\gamma_{a(s)}$ is the apparent activity coefficient of the solute in the stationary phase. Therefore, substituting eq (19) into eq (18) and using eq (2), the hexadecane/methanol-water partition coefficient ($K_{a(h/b+b')}=K_{h/\%w}$) divided by V_n is given by

$$\ln [K_{a(h/b+b')}/V_n]=\ln [\gamma_{a(s)}/\gamma_{a(h)}]-\ln C_s. \tag{20}$$

Using V_n determined on a Zorbax ODS column at 25 °C [9], the plots of ln $[K_{h/\%w}/V_n]$ versus θ_b, the volume fraction of water in methanol, are shown in figures 5 and 6 for the alkylbenzenes and alcohols, respectively. It is observed that ln $[K_{h/\%w}/V_n]$ decreases with increasing θ_b for the solutes studied.

Again we are assuming that the RPLC retention is governed by a single mechanism involving solute partitioning between the mobile phase and the stationary phase consisting of the bonded C18 chains and any solvent (methanol and/or water) which is absorbed by the chains. Examining eq (20), one expects that C_s should decrease with increasing θ_b since any solvent uptake decreases with increasing θ_b. This, however, leads to an increase in ln $[K_{h/\%w}/V_n]$. Therefore, $\gamma_{a(s)}$ must decrease dramatically with increasing θ_b. The solute may be experiencing a mixed C18+methanol environment with pure methanol ($\theta_b=0$). Presumably, the methanol is gradually expelled from the stationary phase with increasing θ_b, leading to a more favorable environment thus the decrease in $\gamma_{a(s)}$. In any event, the stationary phase contribution to V_n is not independent of θ_b.

Another possible interpretation is that RPLC retention is governed by some multiple mechanism where the relative contributions vary with θ_b. Considering a dual mechanism (s and t),

$$V_n=K_{a(s/b+b')}C_s+K_{a(t/b+b')}C_t \tag{21}$$

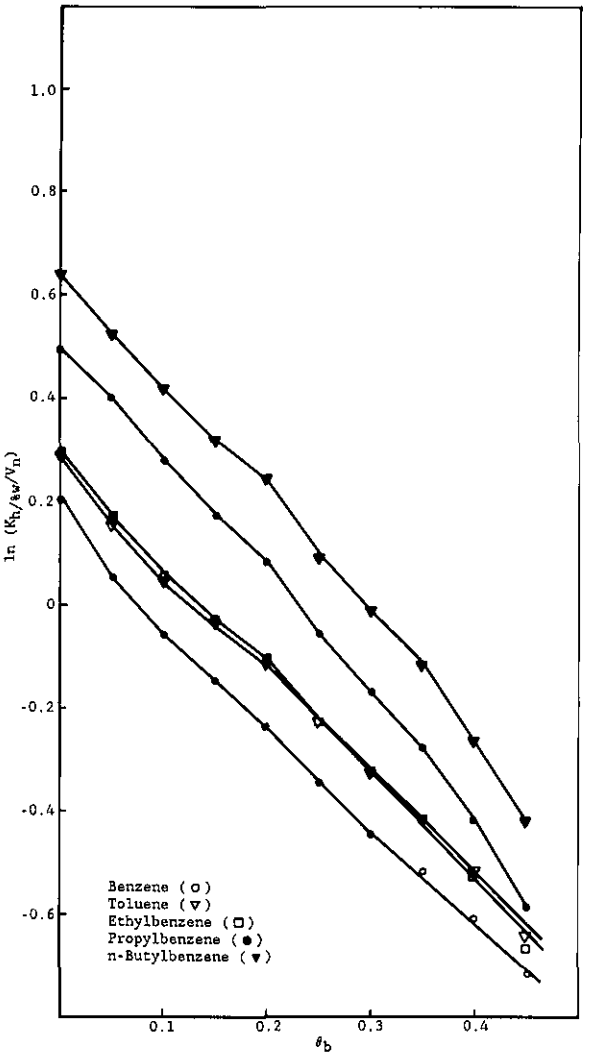

Figure 5. Relationship between ln ($K_{h/\%w}/V_n$) and θ_b for the alkylbenzenes.

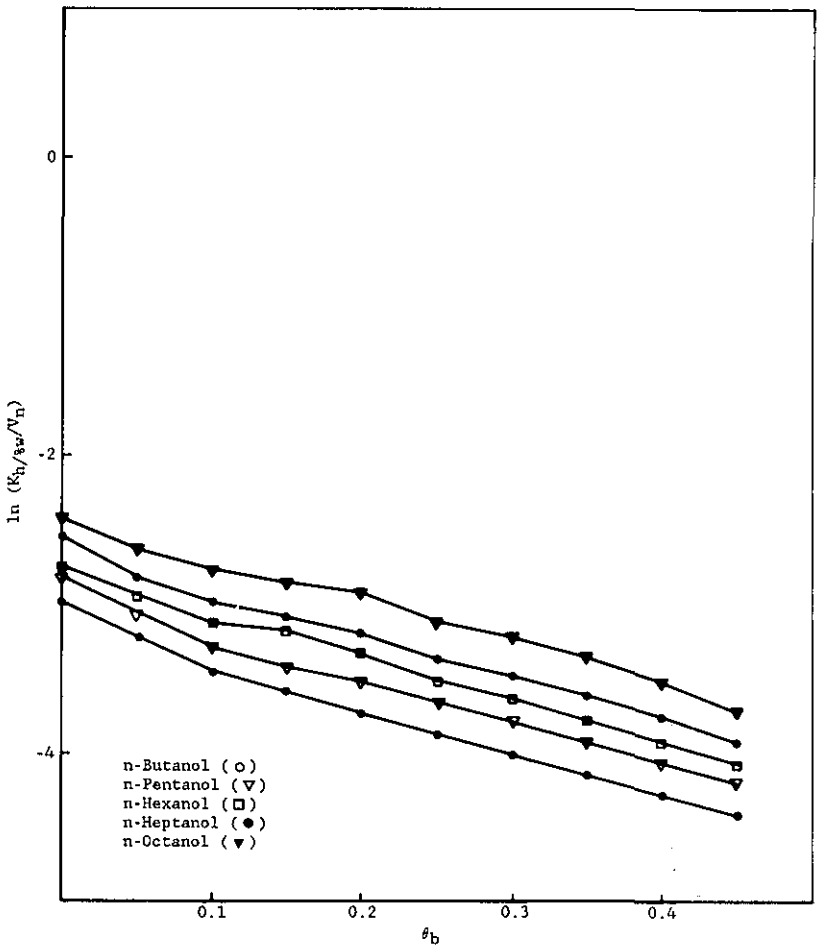

Figure 6. Relationship between ln ($K_{h/\%w}/V_n$) and θ_b for the alcohols.

Here, s might refer to contributions from solute absorption (solvation) by the C18 chains plus a limited amount of incorporated methanol, and t might refer to the contribution from solute adsorption/displacement at the mobile phase-bonded phase interface. At the interface, the composition of the relevant interfacial layer would vary with θ_b and is richer in methanol than the mobile phase. C_s is then the volume of the bonded phase with any solvent uptake included, and C_t is the volume of the interfacial layer which may vary with varying θ_b. Therefore, the partition coefficients are given by

$$K_{a(s/b+b')} = \gamma_{a(b+b')}/\gamma_s \tag{22}$$

$$K_{a(t/b+b')} = \gamma_{a(b+b')}/\gamma_t, \tag{23}$$

where $\gamma_{a(s)}$ and $\gamma_{a(t)}$ are the apparent solute activity coefficients in the stationary phase for retention modes s and t, respectively. Now the hexadecane/methanol-water partition coefficient divided by the net retention volume is given by

$$\ln [K_{a(h/b+b')}/V_n] = -\ln [C_s\gamma_{a(h)}/\gamma_{a(s)}] - \ln [1+(\gamma_{a(s)}C_t/\gamma_{a(t)}C_s)]. \tag{24}$$

Looking at eq (24), one could argue that $C_s/\gamma_{a(s)}$ should remain fairly constant as θ_b increases since there should be little uptake of solvent within the C18 chains. Therefore, the observed decrease in ln $[K_{h/\%w}/V_n]$ with increasing θ_b would then be due to an increase in $(\gamma_{a(s)}C_t)/(\gamma_{a(t)}C_s)$ suggesting that $\gamma_{a(t)}/C_t$, primarily $\gamma_{a(t)}$, must decrease with increasing γ_b. Possibly, as θ_b increases, the interface becomes less rich in methanol so the solute can more readily displace the adsorbed solvent, thus lowering $\gamma_{a(t)}$.

From these observations, it is clear that regardless of the retention mechanism, single or multiple, the stationary phase is not a "passive receptor." It

appears to become progressively more hospitable to the solute with increasing θ_b.

5. Acknowledgments

The work done at Georgetown University is based upon research supported by the National Science Foundation under Grant CHE-8305045. We are also grateful to P. W. Carr and A. Hussam for helpful discussions and for access to unpublished data.

About the authors: Michele Schantz is a chemist with the Organic Analytical Research Division of NBS, B. N. Barman is presently in the Chemistry Department at the University of Utah, and Daniel E. Martire is a professor of chemistry at Georgetown University.

References

[1] Hansch, C., and Leo, A., Substituent Constants for Correlation Analysis in Chemistry and Biology, John Wiley & Sons, New York, (1979).
[2] Schantz, M. M., and Martire, D. E., Determination of Hydrocarbon-Water Partition Coefficients from Chromatographic Data and Based on Solution Thermodynamics and Theory, J. Chromatogr. **391**, 35 (1987).
[3] Martire, D. E., and Boehm, R. E., Unified Theory of Retention and Selectivity in Liquid Chromatography. 2. Reversed Phase Liquid Chromatography with Chemically Bonded Phases, J. Phys. Chem. **87**, 1045 (1983).
[4] Horvath, C., and Melander, W., Liquid Chromatography with Hydrocarbonaceous Bonded Phases; Theory and Practice of Reversed Phase Chromatography, J. Chromatogr. Sci. **115**, 393 (1977).
[5] Jandera, P., Reversed Phase Liquid Chromatography of Homologous Series: A General Method for Prediction of Retention, J. Chromatogr. **314**, 13 (1984).
[6] Hennion, M. C., Picard, C., and Caude, M., Influence of the Number and Length of Alkyl Chains on the Chromatographic Properties of Hydrocarbonaceous Bonded Phases, J. Chromatogr. **166**, 21 (1978).
[7] Bruggeman, W. A., van der Stien, J., and Hutzinger, O., Reversed Phase Thin-Layer Chromatography of Polynuclear Aromatic Hydrocarbons and Chlorinated Biphenyls: Relationship with Hydrophobicity as Measured by Aqueous Solubility and Octanol-Water Partition Coefficient, J. Chromatogr. **238**, 335 (1982).
[8] Grünbauer, H. J. M., and Tomlinson, E., Application of Local-Composition Theory to Reversed-Phase Liquid Chromatography, J. Chromatogr. **268**, 277 (1983).
[9] Barman, B. N., Doctoral Dissertation, Georgetown University, Washington, DC (1985).
[10] Polak, J., and Lu, B. C.-Y., Mutual Solubilities of Hydrocarbons and Water at 0 and 25 °C, Can. J. Chem. **51**, 4018 (1973).
[11] Tewari, Y. B., Miller, M. M., and Wasik, S. P., Calculation of Aqueous Solubility of Organic Compounds, J. Res. Natl. Bur. Stand. (U.S.) **87**, 155 (1982).
[12] Acree, W. E., Jr., Thermodynamic Properties of Nonelectrolyte Solutions, Academic Press, New York (1984).
[13] Riebesehl, W., and Tomlinson, E., Enthalpies of Solute Transfer between Alkanes and Water Determined Directly by Flow Microcalorimetry, J. Phys. Chem. **88**, 4770 (1984).
[14] Backlund, S., Hoiland, H., and Vikholm, I., Water-Alcohol Interactions in the Two Phase System Water-Alcohol-Alkane, J. Soln. Chem. **13**, 749 (1984).
[15] Karickhoff, S. W., and Brown, D. S., Determination of Octanol/Water Distribution Coefficients, Water Solubilities, and Sediment/Water Partition Coefficients for Hydrophobic Organic Pollutants, EPA Report #EPA-600/4-79-032, U.S. Environmental Protection Agency, Athens, GA (1979).
[16] Smith, H. W., The Nature of Secondary Valence Part II. Partition Coefficients, J. Phys. Chem. **25**, 204 (1921).
[17] Krstulovic, A. M., Colin, H., Tchapla, A., and Guiochon, G., Effects of the Bonded Alkyl Chain Length on Methylene Selectivity in Reversed-Phase Liquid Chromatography, Chromatographia **17**, 228 (1983).
[18] Lochmuller, C. H., and Wilder, D. R., The Sorption Behavior of Alkyl Bonded Phases in Reverse-Phase, High Performance Liquid Chromatography, J. Chromatogr. Sci. **17**, 574 (1979).
[19] Hussam, A., and Carr, P. W., University of Minnesota, Minneapolis, MN, private communication.
[20] Bondi, A., Vander Waals Volumes and Radii, J. Phys. Chem. **68**, 441 (1964).